Dynamics of resonant x-ray and Auger scattering

Faris Gel'mukhanov

Department of Theoretical Chemistry and Biology, KTH Royal Institute of Technology, 10691 Stockholm, Sweden,
Institute for Methods and Instrumentation in Synchrotron Radiation Research, Helmholtz-Zentrum Berlin für Materialien und Energie, Albert-Einstein-Strasse 15, 12489 Berlin, Germany,
International Research Center of Spectroscopy and Quantum Chemistry—IRC SQC, Siberian Federal University, 660041 Krasnoyarsk, Russia,
and Kirensky Institute of Physics, Federal Research Center KSC SB RAS, 660036 Krasnoyarsk, Russia

Michael Odelius

Department of Physics, AlbaNova University Center, Stockholm University, SE-106 91 Stockholm, Sweden

Sergey P. Polyutov

International Research Center of Spectroscopy and Quantum Chemistry—IRC SQC, Siberian Federal University, 660041 Krasnoyarsk, Russia
and Kirensky Institute of Physics, Federal Research Center KSC SB RAS, 660036 Krasnoyarsk, Russia

Alexander Föhlisch

Institute for Methods and Instrumentation in Synchrotron Radiation Research, Helmholtz-Zentrum Berlin für Materialien und Energie, Albert-Einstein-Strasse 15, 12489 Berlin, Germany
and Institute of Physics and Astronomy, University of Potsdam, Karl-Liebknecht-Strasse 24-25, 14476 Potsdam, Germany

Victor Kimberg

Department of Theoretical Chemistry and Biology, KTH Royal Institute of Technology, 10691 Stockholm, Sweden
and International Research Center of Spectroscopy and Quantum Chemistry—IRC SQC, Siberian Federal University, 660041 Krasnoyarsk, Russia

(published 8 July 2021)

An overview of both experimental and theoretical results in the field of resonant scattering of tunable soft and hard x-ray radiation is presented, with a main focus on the closely related processes of resonant inelastic x-ray scattering (RIXS) and resonant Auger scattering (RAS). The review starts with an overview of fundamental dynamical aspects of RIXS illustrated for different systems. A detailed analysis of case studies with increasing complexity, considering both gas-phase and condensed matter (liquids and solids) applications, is given. In the review, the most important achievements in investigations of coupled electron-nuclear dynamics and structural aspects in studies of liquids and solids over the last two decades are outlined. To give a perspective on the insights from RIXS and RAS, the x-ray results are discussed against the background of complementary experimental techniques like vibrational infrared absorption and Raman spectroscopy, as well as small-angle x-ray and neutron scattering. Finally, recent achievements in time-resolved studies based on x-ray free-electron lasers are described.

DOI: 10.1103/RevModPhys.93.035001

CONTENTS

I. INTRODUCTION

Scattering of photons, electrons, and neutrons is utilized in many experimental probes for investigation of the structure of matter and of dynamical processes (Sivia, 2011). The interaction with photons has the undeniable advantage of the simplicity of the matrix element of interaction with atoms and molecules. The absorption of x rays by matter involves the interaction of photons with electrons in atomic levels, the energies of which are specific for each element. This makes x-ray spectroscopy a unique, element-specific probe (Svanberg, 2001). Elemental selectivity, greatly simplifying the spectrum (compared to optical and ultraviolet spectroscopy), gives detailed information about the local electronic structure in complex systems since, conceptually, an atom projected contribution to the electronic states can be determined. X-ray spectroscopy includes x-ray absorption spectroscopy (XAS), x-ray photoelectron spectroscopy (XPS), nonresonant x-ray emission spectroscopy (XES), time-of-flight mass spectroscopy, coincidence spectroscopy, Auger spectroscopy, Compton spectroscopy (Kane, 1992; Hämäläinen and Manninen, 2001), etc. Since the creation of x-ray free-electron lasers (XFELs) (Pellegrini, Marinelli, and Reiche, 2016) and high-harmonic generation (HHG) light sources, research has begun in the field of nonlinear spectroscopy and pump-probe field spectroscopy. In this review, we focus on two spectroscopic techniques, initially enabled by the appearance of x-ray synchrotron radiation light sources. We refer to resonant inelastic x-ray scattering (RIXS) and resonant Auger scattering (RAS), known also as resonant x-ray Raman scattering and resonant photoemission, respectively. Apart from the reviews by Nordgren and Rubensson (2013), Simon and Schmitt (2013), Schmitt, de Groot, and Rubensson (2014), van Veenendaal (2015), and van den Brink (2016) and the more recent review of RIXS in the hard x-ray region (Piancastelli *et al.*, 2020), the preceding monograph (Schülke, 2007) and reviews (Gel'mukhanov and Ågren, 1999; Kotani and Shin, 2001; de Groot, 2001; Brühwiler, Karis, and Mårtensson, 2002; Glatzel and Bergmann, 2005; Ament *et al.*, 2011), which to some extent cover these areas of

research, were published about a decade ago. RIXS investigations of electronic structure and excitations in liquids and solids under high pressure were summarized in the review by Rueff and Shukla (2010) and in the recent article by Rossi *et al.* (2019b). There are also recent reviews devoted to theoretical aspects of x-ray spectroscopy (van Veenendaal, 2015; van den Brink, 2016; Norman and Dreuw, 2018; Bokarev and Kühn, 2020), to RIXS of transition-metal complexes (Lundberg and Wernet, 2019), and to XFEL-based time-resolved RIXS studies (Wernet, 2019). We also mention linear-response time-dependent density-functional theory of RIXS of complex systems (Vaz da Cruz, Eckert, and Föhlisch, 2021).

The main emphasis in our review is on processes that are most pronounced in molecules and solids. Nevertheless, we also give an overview of investigations of liquids, for which significant progress has recently been observed. We also discuss the most important results obtained using XFELs.

II. SOURCES OF X-RAY RADIATION AND SPECTRAL INSTRUMENTATION

A detailed overview of experimental methods is beyond the scope of our review. For this, we recommend the extensive analyses of RIXS instrumentation given by Ament *et al.* (2011), Ismail, Simon, and Penent (2020), Jaeschke *et al.* (2020), Piancastelli *et al.* (2020), and Wollenweber *et al.* (2021) and the RAS measurements given by Lindblad *et al.* (2013) and Liu, Nicolas, and Miron (2013). Analyses of experimental techniques used in time-resolved XFEL-based RIXS were given by Lundberg and Wernet (2019), Wernet (2019), and Jaeschke *et al.* (2020).

Presently two contemporary sources of polarized intense x-ray radiation are in use (Ishikawa, 2019). The first category is third-generation synchrotron radiation sources with the storage rings optimized for the use of undulator radiation, while the second category is XFELs. XFELs are in turn subdivided into XFELs based on self-amplified spontaneous emission (SASE) (Ishikawa, 2019; Rossbach, Schneider, and Wurth, 2019), seeded-XFELs in which an external laser is used to initiate the emission process (Amann *et al.*, 2012; Petrillo *et al.*, 2020) and self-seeded XFELs (Kumar *et al.*, 2020).

Notice that there are two types of x-ray spectrometers used in polarization-resolved RIXS, namely, with (Lindle *et al.*, 1991; Southworth, 1994; Ishii *et al.*, 2013; Gao *et al.*, 2016; Brookes *et al.*, 2018; Kim *et al.*, 2018; Sala *et al.*, 2018) and without (Schmitt *et al.*, 2013; Brookes *et al.*, 2018) polarization resolution for the scattered photon; see Sec. IV. The spectral resolution is different in soft and hard x-ray regions. The spectral resolution is usually about 5–10 meV (discussed later) for a hard x-ray wavelength that matches the distance between successive lattice planes (Ament *et al.*, 2011). Ultrahigh resolution (0.1 meV) was obtained in a hard x-ray spectrometer with multicrystal multireflection optics as the dispersing element (Shvyd'ko *et al.*, 2013; Chubar *et al.*, 2016). This scheme does not work for soft x rays, where long wavelengths prohibit the use of crystal optics. Instead artificial periodic structures, diffraction gratings, are used. In the soft x-ray region the best resolution is about 30–100 meV [or even better (Jarrige *et al.*, 2018)], and it depends on the spectrometer design and the quality of the grating (Schmitt, de Groot, and Rubensson, 2014; Chaix *et al.*, 2017; Couto *et al.*, 2017; Brookes *et al.*, 2018).

III. FINGERPRINTS OF RIXS AND RAS

Resonant x-ray scattering occurs when the incoming x-ray photon γ triggers a resonant electronic transition in a target A (atoms, molecules, liquids, and solids). The excited state decays via emission of a photon γ' with the frequency ω' or an Auger electron e^- with the kinetic energy E (see Fig. 1), giving rise to the radiative (RIXS) and resonant Auger (RAS) scattering channels, respectively,

$$\gamma + A \to A_i \to A_f + \begin{cases} \gamma' \\ e^- \end{cases}. \tag{1}$$

RIXS cross section.—The Kramers-Heisenberg (KH) equation

$$\begin{aligned} \sigma(\omega',\omega) &= r_\circ^2 \sum_f |F_f|^2 \Delta(\omega' + \omega_{f0} - \omega, \Gamma_f), \\ F_f &= F_f^T + \sum_i \frac{\omega\omega'}{\omega - \omega_{i0} + i\Gamma} \\ &\quad \times \langle f| \sum (\mathbf{e}' \cdot \mathbf{d}) e^{\imath(\mathbf{k}'\cdot\mathbf{r})} |i\rangle\langle i| \sum (\mathbf{e} \cdot \mathbf{d}) e^{-\imath(\mathbf{k}\cdot\mathbf{r})} |0\rangle, \\ F_f^T &= (\mathbf{e}\cdot\mathbf{e}')\langle f|\rho_{\mathbf{q}}|0\rangle, \qquad \rho_{\mathbf{q}} = \sum e^{\imath\mathbf{q}\cdot\mathbf{r}}, \end{aligned} \tag{2}$$

for the photon scattering cross section was obtained in 1925 before the discovery of quantum mechanics (Kramers and Heisenberg, 1925). Two years later, Dirac (1927) provided a quantum derivation of this formula. Here the first term F_f^T in the scattering amplitude F_f describes the Thomson scattering, for which the contribution to the cross section is determined by the dynamic structural factor $S(\mathbf{q}, \omega - \omega') = |\langle f|\rho_{\mathbf{q}}|0\rangle|^2 \Delta(\omega' + \omega_{f0} - \omega, \Gamma_f)$, $r_\circ = \alpha^2 \approx 2.83 \times 10^{-13}$ cm (the classic electron radius), $\mathbf{q} = \mathbf{k}' - \mathbf{k}$ (the momentum transfer), $\alpha = 1/137$ (the fine-structure constant), $\omega_{ij} = E_i - E_j$ (the spacing between the levels of the quantum system), $\mathbf{k}$, $\mathbf{e}$, $\mathbf{k}'$, $\mathbf{e}'$ denote momentum and polarization

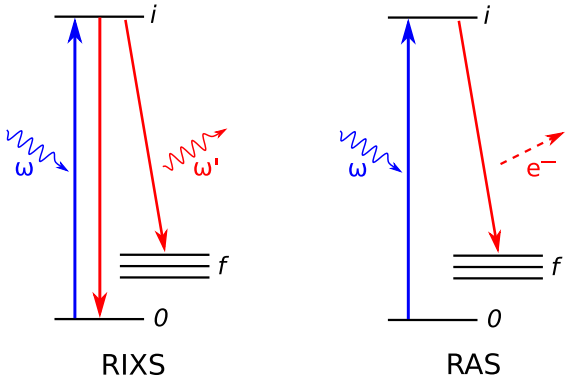

FIG. 1. Illustration of resonant elastic and inelastic x-ray scattering (photon in and photon out) and resonant Auger (photon-in and electron-out) scattering; 0, i, and f refer to the ground, intermediate core-excited, and final electronic states, respectively.

vectors of the initial and scattered photons; $\sum$ denotes a sum over the electrons and $\mathbf{r}$ is the radius vector of an electron $\Delta(\Omega,\Gamma)=\Gamma/\pi(\Omega^2+\Gamma^2)$. Throughout the review, we adhere to the atomic system of units.

In RIXS studies of magnetic materials spin-flip scattering channels are important (Das *et al.*, 2018; Elnaggar *et al.*, 2019; Nag *et al.*, 2020). To describe this process one must add the small relativistic correction to the Thomson term (Blume, 1985)

$$\rho_{\mathbf{q}} \to \rho_{\mathbf{q}} - \imath\omega\alpha^2 \sum e^{\imath\mathbf{q}\cdot\mathbf{r}}\left(\imath\frac{\mathbf{p}\times\mathbf{q}}{k^2}\cdot\mathbf{A}+\mathbf{s}\cdot\mathbf{B}\right), \tag{3}$$

where $\mathbf{A}=\mathbf{e}'\times\mathbf{e}$, $\mathbf{B}=\mathbf{e}'\times\mathbf{e}+(\hat{\mathbf{k}}'\times\mathbf{e}')(\hat{\mathbf{k}}'\cdot\mathbf{e})-(\hat{\mathbf{k}}\times\mathbf{e})(\hat{\mathbf{k}}\cdot\mathbf{e}')-(\hat{\mathbf{k}}'\times\mathbf{e}')(\hat{\mathbf{k}}\times\mathbf{e})$, $\hat{\mathbf{k}}=\mathbf{k}/k$, $\mathbf{p}=-\imath\partial/\partial\mathbf{r}$ is the momentum of electron, and $\mathbf{s}=\sigma/2$ is the spin operator comprising Pauli matrices σ. At the same time, magnetic terms can be neglected in the resonant scattering channel where the dipole approximation [Eq. (2)] is good enough to describe the spin-flip transitions (Såthe *et al.*, 2006; Ament *et al.*, 2011). This is because magnetic scattering is usually studied for RIXS channels with nonzero orbital momentum of the core hole. In this case the magnetic spin-flip transitions occur because of the spin-orbital (SO) mixing of spin and orbital momentum in the core-excited state (de Groot, Kuiper, and Sawatzky, 1998; Såthe *et al.*, 2006). However, modern RIXS with superhigh resolution resolves low-energy ($\lesssim$100 meV) spin-flip peaks caused by SO interaction in the valence shell (Das *et al.*, 2018; Elnaggar *et al.*, 2019; Nag *et al.*, 2020); see Sec. XIII.D.

RAS cross section.—The structure of the RAS amplitude and cross section is similar to the KH equation (2)

$$F_f=(\mathbf{e}\cdot\mathbf{d}_{\mathbf{p}0})+\sum_i\frac{Q_{fi}(\mathbf{e}\cdot\mathbf{d}_{i0})}{\omega-\omega_{i0}+\imath\Gamma},$$
$$\sigma(E,\omega)=\sum_f|F_f|^2\Delta(E+\omega_{f0}-\omega,\Gamma_f), \tag{4}$$

where the first nonresonant term in the scattering amplitude describes the direct photoionization of an electron with kinetic energy $E=p^2/2$, while the second term gives the amplitude of resonant Auger scattering through the intermediate state $|i\rangle$ of a target. The only difference in the second term between RIXS and RAS is that the dipole operator in RIXS is replaced by the interelectronic Coulomb interaction Q, which describes the Auger decay in RAS. This makes the scattering anisotropy of RAS and RIXS significantly different.

Usually, spectral broadening Γ_f of the final valence-excited state is much smaller than the natural width Γ of the x-ray excited state

$$\Gamma_f \ll \Gamma. \tag{5}$$

For this reason, RIXS and RAS spectroscopy can be measured with superhigh resolution, which is limited only by the degree of monochromatization of the initial x-ray beam and the spectral resolution of the instrument. A distinguishing feature of RIXS and RAS is the Raman dispersion law

$$\omega'=\omega-\omega_{f0}, \qquad E=\omega-\omega_{f0}, \tag{6}$$

which is described by Lorentzian $\Delta(\Omega,\Gamma)$ in Eqs. (2) and (4) and which is simply the energy conservation law of the scattering process. Since the fraction of fluorescence yield is of the order of 10^{-4} for the first row molecules, the intensity of the Auger signal is higher, resulting in much better statistics in RAS measurements and, as a result, in a better spectral resolution of RAS than of RIXS. In the soft x-ray range, unlike the hard x-ray range, the Auger contribution to the width Γ exceeds that of the radiative transitions. It was found recently that Γ can be controlled in an x-ray cavity that modifies the spontaneous emission rate (Huang *et al.*, 2021).

Owing to a lack of selection rules for the Q operator, the RAS spectral profile usually contains many overlapping lines, which makes its interpretation more difficult compared to the RIXS spectra. Notice that the nuclear dynamics in the intermediate state strongly violates the Raman dispersion [Eq. (6)] (Gel'mukhanov and Ågren, 1996a; Hikosaka *et al.*, 2008; Velkov *et al.*, 2009; Liu *et al.*, 2011a; Weinhardt *et al.*, 2011).

Special attention is paid in the review to $\exp[\imath(\mathbf{q}\cdot\mathbf{R})]$, which is responsible for the recoil effect, namely, the momentum exchange between photons, electrons, and nuclei with nuclear coordinate $\mathbf{R}$. For example, in the soft x-ray region $qR\ll 1$ and Thomson scattering, described by the first term in Eq. (2) $F_f^T\propto\delta_{f,0}$, is an elastic process. Increase of the x-ray photon energy ($qR\gtrsim 1$) opens an inelastic Compton scattering channel (Kane, 1992; Spielberger *et al.*, 1995; Hämäläinen and Manninen, 2001). A similar factor in the RAS $\exp[\imath(\mathbf{p}\cdot\mathbf{R})]$, which describes the Doppler and recoil effects, already leads to a number of phenomena in the soft x-ray range due to the large magnitude of the Auger electron momentum $\mathbf{p}$; see Sec. V.

IV. POLARIZATION-RESOLVED RIXS

The polarization anisotropy of RIXS from disordered systems and crystals (Braicovich *et al.*, 2014; Brookes *et al.*, 2018) (Sec. XII) allows one to gain information on the symmetry of the excitations, and therefore on their nature. The polarization filters overlapping energy states of different symmetry (Braicovich *et al.*, 2014) and allows one to reduce the nonresonant contributions. In studies of magnetic circular dichroism (MCD) we need circular polarized light (Sec. XII). The first impression is that the scattering by randomly oriented molecules in a gas or liquid must be isotropic. However, this is not the case (Gel'mukhanov and Mazalov, 1977; Gel'mukhanov and Ågren, 1994).

A. Scattering anisotropy by randomly oriented molecules

Anisotropy of RIXS from randomly oriented samples was already confirmed in the first measurements on polarization dependence (Lindle *et al.*, 1991). Moreover, the scattering anisotropy is different for different molecular orbitals involved in the RIXS (Gel'mukhanov and Mazalov, 1977; Gel'mukhanov and Ågren, 1994). The physical reason for the scattering anisotropy is that RIXS is a two-step process. At the absorption stage $\propto(\mathbf{e}\cdot\mathbf{d}_{i0})^2$, mainly molecules with a dipole transition moment $\mathbf{d}_{i0}$ predominantly aligned along $\mathbf{e}$ are excited. Thus, even in an isotropic ensemble the excited

molecules are not randomly oriented. Taking into account that the emission of the final photon comes from an ensemble of partially aligned molecules, it is possible to see that the scattering will be anisotropic with the scattering anisotropy R_{fi}, depending on the relative orientation of the dipole moments of the emission and absorption of $(\mathbf{d}_{fi}\cdot\mathbf{d}_{i0})$ (Gel'mukhanov and Mazalov, 1977; Gel'mukhanov and Ågren, 1994):

$$\sigma_{fi}(\omega',\omega,\theta)=\sigma_{fi}[1+R_{fi}(3\cos^2\theta-1)],$$
$$R_{fi}=\tfrac{1}{5}[3(\hat{\mathbf{d}}_{fi}\cdot\hat{\mathbf{d}}_{i0})^2-1]. \quad (7)$$

Equation (7) is obtained by averaging over molecular orientations of the resonance contribution to the cross section [Eq. (2)] with one intermediate state i. Here $\sigma_{fi}\equiv\sigma_{fi}(\omega',\omega)$ is the isotropic part of the cross section and $\theta=\angle(\mathbf{e}',\mathbf{e})$. The anisotropy parameter in the experiment is defined as $R_{fi}=[\sigma_{fi}(0)-\sigma_{fi}(90°)]/[\sigma_{fi}(0)+2\sigma_{fi}(90°)]$. The RIXS anisotropy of Eq. (7) can be measured using instruments with polarization resolution for the scattered photons.

In experiments without polarization resolution for the scattered photons, the spectrometer "sums" all final polarizations (Gel'mukhanov and Ågren, 1994; Gunnelin *et al.*, 1998; Vaz da Cruz *et al.*, 2019b). Therefore, the RIXS cross section [Eq. (7)] should be averaged over the orientations $\mathbf{e}'$ around the direction of departure $\mathbf{k}'$ of the scattered photon using

$$e'_ie'_j\to\tfrac{1}{2}(\delta_{ij}-\hat{\mathbf{k}}'_i\hat{\mathbf{k}}'_j). \quad (8)$$

Here and to follow, a hat denotes the unit vector ($\hat{\mathbf{k}}=\mathbf{k}/k$). After the averaging the cross section depends on the angle $\chi=\angle(\mathbf{k}',\mathbf{e})$ between the polarization vector of the initial and the direction of the scattered photons

$$\sigma_{fi}(\omega',\omega,\chi)=\sigma_{fi}[1+\mathcal{R}_{fi}(3\cos^2\chi-1)]. \quad (9)$$

Since we kept the same structure of Eq. (9) as in Eq. (7), the expression for the scattering anisotropy changed: $\mathcal{R}_{fi}=-R_{fi}/2$. The anisotropy parameter decreased by a factor of 2 due to additional averaging over the orientations of $\mathbf{e}'$. We illustrate the large magnitude of the RIXS anisotropy effect using the case of $1s\to\sigma^*$ absorption transition in a diatomic molecule with subsequent emission transitions from occupied σ and π molecular orbitals: $R_{\sigma\sigma^*}=2/5$, $R_{\pi\sigma^*}=-1/5$. This example shows that polarization measurements can extract information about the spatial orientation of molecular orbitals, which has been repeatedly confirmed in experiments. The scattering anisotropy in RIXS has been studied for many systems: CH_3Cl (Lindle *et al.*, 1988, 1991), CF_3Cl (Lindle *et al.*, 1991; Southworth *et al.*, 1991), H_2S (Mayer *et al.*, 1991), CF_2Cl_2, $CFCl_2$ (Lindle *et al.*, 1991), SF_6 (Ekholm *et al.*, 2020), C_{60} (Luo *et al.*, 1995), C_{70} (Guo *et al.*, 1995), CO_2 (Gunnelin *et al.*, 1998), liquid water (Forsberg *et al.*, 2009; Odelius, 2009a), etc. A spherical tensor technique for the RIXS cross section allows one to study general properties of the scattering anisotropy beyond the dipole approximation (Juhin, Brouder, and de Groot, 2014).

B. Scattering anisotropy due to molecular field splitting of the core shell

The molecular field can break the spherical symmetry of the core shells (Svensson *et al.*, 1994; Gel'mukhanov, Ågren, Svensson *et al.*, 1996; Ertan *et al.*, 2020), thereby slightly (~100 meV) splitting the spin-orbit sublevels of deep core electrons. This occurs in the $L_{II,III}$ shell of the sulfur atom of the H_2S molecule or chlorine atom in the HCl and CF_3Cl molecules. The spin-orbit components split by the molecular field acquire a certain spatial orientation (Svensson *et al.*, 1994; Gel'mukhanov, Ågren, Svensson *et al.*, 1996), thereby making the intensity distribution dependent on the relative orientation of the core and valence molecular orbitals (Svensson *et al.*, 1994; Gel'mukhanov, Ågren, Svensson *et al.*, 1996). This introduces a specific scattering anisotropy to RIXS (Guillemin *et al.*, 2008; Carniato *et al.*, 2009; Puglisi *et al.*, 2020).

V. INTERFERENCE OF SCATTERING CHANNELS

Often there are several intermediate core-excited states that are closely spaced in energy. Channel interference should be expected for RIXS through these states.

A. Young's double-slit experiment (YDSE) interference of scattering channels in symmetric molecules and selection rules

One of the most striking manifestations of interference in RIXS is the interference of resonant scattering channels through intermediate states with core holes localized at different atoms. It can manifest in symmetrical molecules, such as N_2, O_2, and Cl_2 (Gel'mukhanov, Mazalov, and Shklyaeva, 1975; Gel'mukhanov and Ågren, 1994, 1999), or in the crystals (Gel'mukhanov, Mazalov, and Shklyaeva, 1976). This effect is in close analogy with wave scattering by two slits (YDSE) (Gel'mukhanov, Privalov, and Ågren, 1998b; Gel'mukhanov and Ågren, 1999; Liu *et al.*, 2015). YDSE interference in symmetrical molecules has been repeatedly studied in XPS (Liu *et al.*, 2006; Ueda *et al.*, 2006, 2009; Gel'mukhanov *et al.*, 2007; Canton *et al.*, 2011; Argenti *et al.*, 2012), where it is named the Cohen-Fano effect after the seminal article by Cohen and Fano (1966). YDSE interference in RAS of molecular oxygen gives a unique realization of the Einstein-Bohr recoiling double-slit gedanken experiment at the molecular level (Liu *et al.*, 2015); see Sec. VII.B.

To clarify the physical picture of the phenomenon, we consider RIXS by a homonuclear diatomic molecule in the gerade (g) ground state. The initial photon (ω, $\mathbf{e}$, $\mathbf{k}$, etc.) excites the $1s$ electron of one of the atoms to the unoccupied σ molecular orbital (MO) ψ_ν. Then the electron from the occupied σ MO ψ_j fills the vacancy at the $1s$ level and a scattered photon is emitted (ω', $\mathbf{e}'$, $\mathbf{k}'$, etc.). For definiteness, we assume that both molecular orbitals have σ symmetry. Both scattering channels must be taken into account:

$$\omega+A_2\to\left\{\begin{matrix}A^*A\\AA^*\end{matrix}\right\}\to[A_2]_f+\omega'. \quad (10)$$

An asterisk marks an atom with a $1s$ hole. Having placed the origin at the center of symmetry and neglecting an

insignificant constant prefactor, we write the total scattering amplitude as the sum of the amplitudes of both channels

$$F_f = (\mathbf{e}\cdot\mathbf{n})(\mathbf{e}'\cdot\mathbf{n})(e^{\imath(\mathbf{q}\cdot\mathbf{R})/2} + \mathcal{P}_f e^{-\imath(\mathbf{q}\cdot\mathbf{R})/2}), \qquad (11)$$

where $\mathbf{n} = \mathbf{R}/R$, with $\mathbf{R}$ the interatomic radius vector, and $\mathcal{P}_f = 1$ or -1 when $f = g$ or u, respectively. The parity $\mathcal{P}_f$ of the final state $|f\rangle = |\psi_j^{-1}\psi_\nu^1\rangle$ is defined by the parity of the product $\psi_j\psi_\nu$. First, we write the expression for the scattering cross section of a molecule oriented in space

$$\sigma_f = |F_f|^2 = 2a^2[1 + \mathcal{P}_f\cos(\mathbf{q}\cdot\mathbf{R})] \times \frac{\Delta(\omega' - \omega + \omega_{f0}, \Gamma_f)}{(\omega - \omega_{i0})^2 + \Gamma^2},$$
$$a = (\mathbf{e}\cdot\mathbf{n})^2(\mathbf{e}'\cdot\mathbf{n})^2, \qquad q \approx 2k\sin\frac{\Theta}{2}. \qquad (12)$$

Here $\Theta = \angle(\mathbf{k}', \mathbf{k})$ is the scattering angle. In obtaining the expression for q, we have used the fact that the energy of the valence electron is small relative to the photon energy ω. As expected, the selection rules for the scattering cross section $\sigma_u = 0$ are satisfied in the region of soft x-ray radiation or small-angle scattering $qR \ll 1$. However, the selection rules are violated when moving into the hard x-ray regime $qR > 1$, where the scattering channel to the ungerade final state opens ($\sigma_u \neq 0$).

In a real experimental situation, the molecules are randomly oriented and the scattering cross section must be averaged over all orientations, following the theoretical work (Gel'mukhanov, Mazalov, and Shklyaeva, 1975; Gel'mukhanov and Ågren, 1994; Gel'mukhanov, Privalov, and Ågren, 1998b). Because of our interest in selection rules, we write the ratio of the peak intensities of the forbidden and allowed scattering channels as (Fig. 2)

$$\frac{\sigma_u(\omega', \omega)}{\sigma_g(\omega', \omega)} = \frac{1 - \varrho}{1 + \varrho} = \begin{cases} 0, & qR \ll 1, \\ 1, & qR \gg 1, \end{cases} \qquad (13)$$

where the interference factor $\varrho = \overline{a\cos(\mathbf{q}\cdot\mathbf{R})}/\bar{a}$ (Gel'mukhanov, Mazalov, and Shklyaeva, 1975; Gel'mukhanov and Ågren, 1994; Gel'mukhanov, Privalov, and Ågren, 1998b),

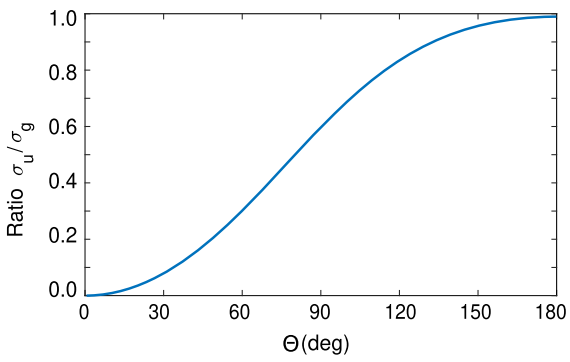

FIG. 2. Ratio $\sigma_u/\sigma_g = 15j_2(qR)/(qR)^2$ [Eq. (13)] for the Cl $1s$ RIXS of the Cl_2 molecule vs the scattering angle Θ. $\mathbf{e}'\|\mathbf{e}$.

$$\varrho = 15\left[\frac{j_2(qR)}{(qR)^2} - \frac{j_3(qR)}{4qR\sin^2(\Theta/2)}\frac{(\mathbf{e}'\cdot\hat{\mathbf{k}})^2}{1 + 2(\mathbf{e}'\cdot\mathbf{e})^2}\right], \qquad (14)$$

tends to unity for soft x-ray radiation or small-angle scattering ($qR \ll 1$). In the opposite limit of the hard x-ray regime ($qR \gg 1$), the interference factor tends to zero [$\varrho \sim 1/(qR)^2$]. Here $j_\ell(x)$ is the Bessel spherical function and the overline refers to averaging over the molecular orientations. To avoid cumbersome expressions, Eq. (14) is written for the typical geometry of the experiment, where $\mathbf{k}'\perp\mathbf{e}$ (Lindle *et al.*, 1991).

Equation (13) shows that the selection rules are fulfilled only for soft x-ray radiation or small-angle scattering ($\varrho \approx 1$), which was confirmed in experiments with the N_2 (Glans, Skytt *et al.*, 1996a) (see Fig. 3) and O_2 (Glans, Gunnelin *et al.*, 1996) molecules. The same selection rules hold under core excitation above core-ionization threshold in the region of shape resonances (Gel'mukhanov and Ågren, 1996; Glans, Skytt *et al.*, 1996b).

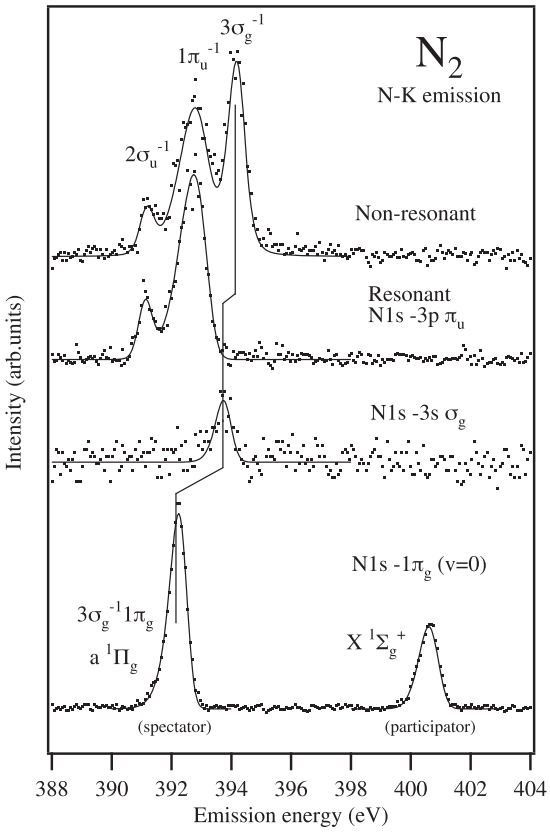

FIG. 3. Soft x-ray RIXS spectra of the N_2 ($1\sigma_g^2, 1\sigma_u^2, 2\sigma_g^2, 2\sigma_u^2, 1\pi_u^4, 3\sigma_g^2$) molecule shows that the scatterings to ungerade final states $3\sigma_g^{-1}3p\pi_u^1$, ($1\pi_u^{-1}3s\sigma_g^1$, $2\sigma_u^{-1}3s\sigma_g^1$), and ($1\pi_u^{-1}1\pi_g^1$, $2\sigma_u^{-1}1\pi_g^1$) are forbidden under core excitation to ungerade core-excited states $1\sigma_g^{-1}3p\pi_u^1$, $1\sigma_u^{-1}3s\sigma_g^1$, and $1\sigma_u^{-1}1\pi_g^1$, respectively. These selection rules are absent for nonresonant x-ray emission due to degeneracy of the final continuum states with opposite parities (Gel'mukhanov and Ågren, 1994). Circles and solid lines show experimental and theoretical spectra, respectively. From Glans, Skytt *et al.*, 1996a.

The interference of scattering channels in the hard x-ray range ($\varrho < 1$) violates the parity ban and opens the scattering channel from a gerade initial to an ungerade final state. This effect, previously predicted by Gel'mukhanov, Mazalov, and Shklyaeva (1975), Gel'mukhanov and Ågren (1994), and Gel'mukhanov, Privalov, and Ågren (1998b), was experimentally confirmed in a study (Mills *et al.*, 1997) of the Cl_2 molecule; see Fig. 4.

The interference structure [Eq. (12)] for oriented diatomic molecules is reduced in the gas phase (Fig. 2) due to orientational disorder [Eq. (14)]. In the $Ba_3CeIr_2O_9$ crystal, which contains quasimolecular orbitals localized on ordered dimers, a distinct interference structure [Eq. (12)] was observed (Revelli *et al.*, 2019).

The selection rules in RIXS deserve a special comment; see also Sec. VIII. The dipole selection rules can be violated in the hard x-ray region. For example, the importance of quadrupole transitions was demonstrated in $1s2p$ RIXS of titanium oxide ($\omega \approx 4970$ eV) (Bagger *et al.*, 2017). The role of higher multipoles in RIXS was analyzed by Ament *et al.* (2011), Juhin, Brouder, and de Groot (2014), and van Veenendaal (2015). The violation of selection rules due to YDSE interference [Eq. (12)] is defined by the molecular size R instead of the much smaller size of the localized core hole a_{1s}. This fact is related to the size of the delocalized core hole $1\sigma_{g,u} = (1s_1 \pm 1s_2)/\sqrt{2}$, which is equal to R (Gel'mukhanov and Ågren, 1994, 1998a, 1999; Mills *et al.*, 1997; Gel'mukhanov, Privalov, and Ågren, 1998a). Thus, the YDSE breakdown of selection rules gives raise to a strong nondipolar effect defined by parameter qR instead of qa_{1s}. The selection rules can also be broken due to vibronic coupling (VC) or electron-phonon interaction (Skytt *et al.*, 1996; Köuppel, Domcke, and Cederbaum, 2007; Miedema *et al.*, 2014) (Sec. VIII). The internal spin symmetry of molecular oxygen leads to new selectional rules in RIXS (Sun, Pietzsch *et al.*, 2011). The selection rules can also be broken because the core electron and excited electron can swap parity in RIXS (Sun, Pietzsch *et al.*, 2011; Sun *et al.*, 2013). There are also special selection rules for Franck-Condon (FC) amplitudes (Couto *et al.*, 2017; Vaz da Cruz *et al.*, 2018).

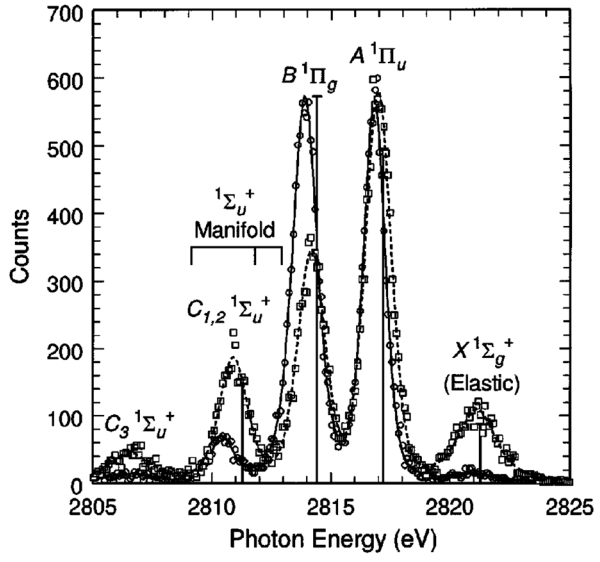

FIG. 4. RIXS in the hard x-ray region of the Cl_2 molecule shows the symmetry-forbidden resonances $C_{1,2}{}^1\Sigma_u^+$ and $A^1\Pi_u$ [$\varrho < 1$; see Eq. (13)]. The experiment was performed for $\angle(\mathbf{k}', \mathbf{k}) = 90°$ and two orientations of polarizations of initial and scattered photons $\angle(\mathbf{e}', \mathbf{e}) = 90°$ (squares) and 0° (circles). From Mills *et al.*, 1997.

B. Interference of scattering channels in crystals: Conservation of momentum

The previously considered interference should also occur in crystals with a periodic arrangement of identical atoms. The initial photon in the crystal excites a $1s_n$ electron localized on the nth atom to the conduction band ($1s_n \to \psi_{c\mathbf{p}}$). Then the valence electron fills the vacancy in the $1s_n$ level ($\psi_{v\mathbf{p}'} \to 1s_n$) and photon ω' is emitted. In the RIXS amplitude, we must sum over all intermediate core-hole states, as in the previously considered case of a diatomic molecule,

$$F \propto \sum_n \frac{\langle 1s_n|D'e^{-\imath\mathbf{k}'\cdot\mathbf{r}}|\psi_{v\mathbf{p}'}\rangle\langle\psi_{c\mathbf{p}}|De^{\imath\mathbf{k}\cdot\mathbf{r}}|1s_n\rangle}{\omega - \omega_{c\mathbf{p}} + \imath\Gamma}. \quad (15)$$

The resonant energy of photoabsorption is approximately equal to the difference between the energies of the electron in the conduction band and on the $1s$ level ($\omega_{c\mathbf{p}} \approx \epsilon_{c\mathbf{p}} - \epsilon_{1s}$). Using Bloch's theorem, $\psi_{\mathbf{p}} = e^{\imath\mathbf{p}\cdot\mathbf{r}}u(\mathbf{r})$, where $u(\mathbf{r}) = u(\mathbf{r} + \mathbf{R}_n)$ is a periodic function, the dipole approximation for the atomic matrix transition element, and

$$\sum_n e^{\imath(\mathbf{p}'-\mathbf{p}-\mathbf{q})\cdot\mathbf{R}_n} \propto \sum_{\mathbf{G}} \delta(\mathbf{p}' - \mathbf{p} - \mathbf{q} - \mathbf{G}), \quad (16)$$

we obtain (Gel'mukhanov, Mazalov, and Shklyaeva, 1976; Gel'mukhanov and Ågren, 1998b; Gel'mukhanov, Privalov, and Ågren, 2000)

$$\sigma(\omega', \omega) \propto \sum_{\mathbf{G}} \int d\mathbf{p}|D'_{v\mathbf{p}'}D_{i\mathbf{p}}|^2 \times \Delta(\omega - \omega_{v\mathbf{p}}, \Gamma)\Delta(\omega' - \omega - \omega_{c\mathbf{p},v\mathbf{p}'}, \Gamma_f), \quad \mathbf{p}' = \mathbf{p} + \mathbf{q} + \mathbf{G}, \quad (17)$$

where $\mathbf{G}$ is the reciprocal lattice vector ($\omega_{c\mathbf{p},v\mathbf{p}'} \approx \epsilon_{c\mathbf{p}} - \epsilon_{v\mathbf{p}'}$) and $D_{c\mathbf{p}'}$ and $D'_{v\mathbf{p}'}$ are matrix elements of x-ray transitions to the conduction band (CB) and from the valence band (VB), respectively. In the soft x-ray range, the photon momentum transferred to the electrons is small ($q \ll G$). Since the momenta of the valence electron and the conduction electron approximately coincide,

$$\mathbf{p}' \approx \mathbf{p}, \quad (18)$$

the scattering process is vertical. The spectral features of RIXS are determined by the interband density of states $\rho(\omega', \omega)$ (Gel'mukhanov, Mazalov, and Shklyaeva, 1976; Gel'mukhanov, Privalov, and Ågren, 2000)

$$\rho(\omega',\omega)=\sum_{v<F,c>F}\int d\mathbf{p}\delta(\omega-\omega_{c\mathbf{p}})\delta(\omega'-\omega_{v\mathbf{p}}), \quad (19)$$

where the summation is carried out over the zones above and below the Fermi level (F). The interband density of states is related to the formation of the RIXS spectrum of periodic structures. The frequency of the initial photon determines the crystal momentum $\mathbf{p}$ ($\omega_{c\mathbf{p}}=\omega$), and hence the resonant frequency of emission transition $\omega'=\omega_{v\mathbf{p}}$; see Fig. 5(a).

The variation of ω changes the resonance value of the momentum $\mathbf{p}$ and the position of the emission peak $\omega'=\omega_{v\mathbf{p}}$ changes accordingly; see Fig. 5(a). This explains the evolution of the RIXS spectrum when ω changes (Carlisle *et al.*, 1995, 1999; Shirley, 2000) and allows one to solve the inverse problem of reconstruction of the band structure from experimental RIXS spectra (Lüning *et al.*, 1997; Kanász-Nagy *et al.*, 2016).

The RIXS process ceases to be vertical (Gel'mukhanov, Mazalov, and Shklyaeva, 1976; Gel'mukhanov, Privalov, and Ågren, 2000; Ament *et al.*, 2011) in the hard x-ray region ($q\gtrsim G$) due to the transfer of large momentum from the photons to the electrons. In this case, one should use the strict law of momentum conservation (17) instead of Eq. (18). The $\mathbf{q}$ dependence of the RIXS cross section is a powerful tool for studying the dispersion of low-energy excitations in solids (Ulrich *et al.*, 2009; Kim *et al.*, 2012; Schlappa *et al.*, 2012; Le Tacon *et al.*, 2014). (See Secs. IX.C and XIII.C.)

The electron-phonon scattering involving the linear (Gel'mukhanov, Privalov, and Ågren, 1998b; Privalov, Gel'mukhanov, and Ågren, 1999) and angular momentum (Privalov, Gel'mukhanov, and Ågren, 1999; Beye *et al.*, 2009) of the phonon violates the law (18). The RIXS profile becomes sensitive to temperature due to electron-phonon scattering that increases the incoherent scattering. Angular momentum of the phonon opens the symmetry-forbidden p-p decay channels, as shown in RIXS from crystalline silicon (Beye *et al.*, 2009).

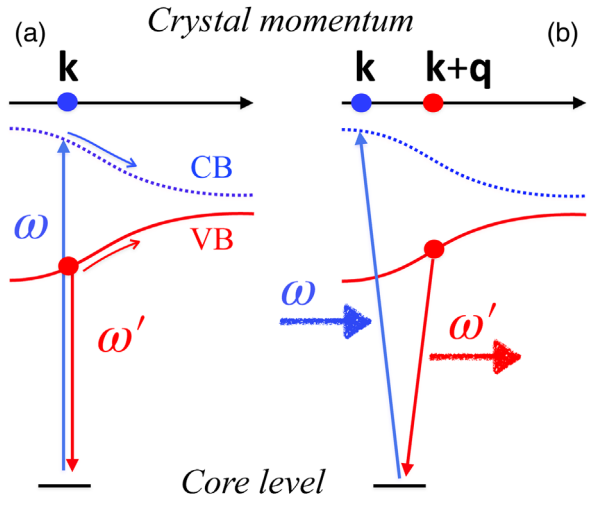

FIG. 5. Physical picture of the evolution with detuning of RIXS resonance in a crystal. (a) Momentum transfer $\mathbf{q}$ is negligible for soft x rays. For this reason the final state consists of a vertical VB-to-CB excitation, whose crystal momentum is selected by the energy of the incoming photon as indicated. A showcase of this is the RIXS of graphite (Carlisle *et al.*, 1995). (b) RIXS transitions cease to be vertical in the hard x-ray region.

Sudden appearance of the core hole leads to an infinite number of low-energy electron-hole pairs generated in the vicinity of the Fermi surface. This results in the edge singularity in the soft XAS and XES spectra of metals known as the Mahan–Noziéres–de Dominicis effect (Doniach and Sondheimer, 1998). This dynamical effect in RIXS was studied by Noziéres and Abrahams (1974), Privalov, Gel'mukhanov, and Ågren (2001), and Hancock *et al.* (2010).

C. Lifetime vibrational interference

Modern RIXS and RAS spectroscopy resolve the vibrational structure (see Sec. VI.B), which is extremely sensitive to the dynamics of nuclei in the intermediate electronic state. It has been firmly established that the formal reason for the nuclear dynamics is the interference of intermediate vibrational states (Gel'mukhanov, Mazalov, and Kondratenko, 1977), which for RIXS on the vibrational ground state coherently forms the scattering amplitude

$$F_{\nu_f}=\sum_{\nu_i}F_{\nu_f,\nu_i}=\sum_{\nu_i}\frac{\langle\nu_f|V_{fi}|\nu_i\rangle\langle\nu_i|D_{i0}|0\rangle}{\omega-\omega_{i0}-w_{\nu_i,0}+\imath\Gamma}, \quad (20)$$

which also can be formulated as the projection of the wave packet $|\Psi\rangle$ onto the final vibrational state $|\nu_f\rangle$:

$$F_{\nu_f}=-\imath\langle\nu_f|\Psi\rangle,$$
$$|\Psi\rangle=\imath\sum_{\nu_i}\frac{V_{fi}|\nu_i\rangle\langle\nu_i|D_{i0}|0\rangle}{\omega-\omega_{i0}-w_{\nu_i,0}+\imath\Gamma}. \quad (21)$$

Here $\omega_{i0}=E_i-E_o$ and $w_{\nu_i,0}=\varepsilon_{\nu_i}-\varepsilon_0$ is a difference of energies of electronic and vibrational states, respectively. As seen in Eq. (21), the wave packet $|\Psi\rangle$ is a coherent superposition of intermediate vibrational states $|\nu_i\rangle$. This is denoted life-vibrational interference (LVI) (Skytt *et al.*, 1997) since it captures vibrational dynamics occurring during the lifetime of the core-excited state $2/\Gamma$. Equations (20) and (21), obtained in the Born-Oppenheimer (BO) approximation from the general KH formula (2), are valid for both RIXS and RAS processes with one intermediate electronic state i. In the first case $V_{fi}=D'_{fi}$, and in the second case $V_{fi}=Q_{fi}$ is a matrix element of the Coulomb interaction between the electrons. Here and to follow, the vibrational state of electronic state i is denoted by a greek letter $|\nu_i\rangle$, $D_{i0}=(\mathbf{e}\cdot\mathbf{d}_{i0})$, and $D'_{fi}=(\mathbf{e}'\cdot\mathbf{d}_{fi})$.

To demonstrate the crucial role of interference, we divide the cross section into direct and interference contributions (Gel'mukhanov, Mazalov, and Kondratenko, 1977):

$$\sigma(\omega',\omega)=\sigma_{\rm dir}(\omega',\omega)+\sigma_{\rm int}(\omega',\omega),$$
$$\sigma_{\rm dir}(\omega',\omega)=\sum_{\nu_f,\nu_i}|F_{\nu_f,\nu_i}|^2\Delta(\varepsilon,\Gamma_f),$$
$$\sigma_{\rm int}(\omega',\omega)=\sum_{\nu_f,\nu_i\neq\nu'_i}F^*_{\nu_f,\nu_i}F_{\nu_f,\nu'_i}\Delta(\varepsilon,\Gamma_f), \quad (22)$$

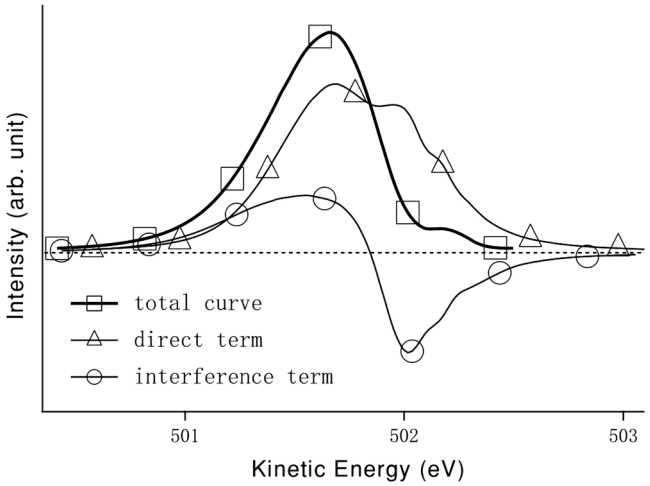

FIG. 6. The LVI line shape of the normal Auger spectral component $1^3\Delta_u$ of the O_2 molecule. The thick line with squares is the total LVI line shape $\sigma(E,\omega)$, the line with triangles is calculated using the direct term $\sigma_{\rm dir}(E,\omega)$ in the LVI formula (22), and the line with circles shows the LVI interference term $\sigma_{\rm int}(E,\omega)$. From Bao *et al.*, 2008.

where $\varepsilon = \omega' - \omega - \omega_{f0} - w_{\nu_f,0}$. Figure 6 shows that taking into account only the direct contribution of $\sigma_{\rm dir}$ leads to a strong deviation from the total cross section of σ. The physical reason for this is that a description of the dynamics of nuclei is impossible without taking into account vibrational interference. The decisive role of interference for intermediate states in a continuous spectrum, as in the case of dissociative states, is obvious. In the wave packet technique presented in Sec. VI.A, the interference is taken into account automatically through the completeness condition

$$\sum_{\nu} |\nu\rangle\langle\nu| = 1. \tag{23}$$

RIXS and RAS theory, which takes into account the LVI of scattering channels through closely spaced intermediate states (Gel'mukhanov, Mazalov, and Kondratenko, 1977), is a necessary tool for a correct description of RIXS and RAS experimental spectra (Neeb *et al.*, 1994; Kjellsson *et al.*, 2021). As examples of recent progress, we mention successful applications of the LVI theory to describe the RIXS and RAS spectra of polyatomic molecules with a large number of vibrational modes and their overtones in water (Vaz da Cruz *et al.*, 2017), methanol (Vaz da Cruz *et al.*, 2019b), acetone (Sun *et al.*, 2011), and ethene (Liu *et al.*, 2011b).

1. Sum rules: Optical theorem

There are certain sum rules for resonant scattering (Gel'mukhanov and Ågren, 1996a; Gel'mukhanov, Ågren, Neeb *et al.*, 1996). The first one follows directly from the optical theorem, which makes the link between the total RIXS cross section and the imaginary part of the scattering amplitude ImF that is proportional to the XAS cross section. This sum rule also implies that the integral of the interference term is equal to zero,

$$\int \sigma_{\rm int}(\omega',\omega)d\omega' = 0, \tag{24}$$

in the FC approximation. There are also sum rules for the center of gravity and for the width of the RIXS and RAS profiles (Gel'mukhanov and Ågren, 1996a; Gel'mukhanov, Ågren, Neeb *et al.*, 1996), which were investigated recently in experiment (Piancastelli *et al.*, 2020).

2. X-ray absorption measured in x-ray Raman mode

An important property of RIXS and RAS is the spectral resolution that is not influenced by a lifetime broadening of core-excited states. This is the origin of the idea to resolve the transitions in XAS beyond the lifetime broadening limit of core-excited states. Tulkki and Åberg (1982) suggested that lifetime broadening free XAS can be achieved by scanning over the frequencies of the incoming photons while keeping the emission frequency fixed at the maximum of an x-ray fluorescence line. Narrowing of x-ray absorption resonances was experimentally evidenced in the RIXS (Hämäläinen *et al.*, 1991) and RAS (Hikosaka *et al.*, 2008) modes; see also (de Groot (2001) and Glatzel and Bergmann (2005). It has even been given a special name: high-energy-resolution fluorescence detected (HERFD) XAS (Glatzel *et al.*, 2002, 2005; Safonova *et al.*, 2006). We point out that an XAS profile measured in the scattering mode is sensitive to the final RIXS or RAS state and can strongly deviate from the true XAS profile (Carra, Fabrizio, and Thole, 1995; Gel'mukhanov and Ågren, 1999; Hikosaka *et al.*, 2008; Glatzel, Sikora, and Fernández-Garćia, 2009). Measurement of XAS in the RIXS mode was recently studied theoretically for the vibrationally excited water molecule (Ignatova *et al.*, 2017a, 2017b), where it was shown that this technique allows for a distinction of XAS contributions from different initial vibrational states.

The second opportunity was recognized by Rubensson (2000), who showed that the low-energy tail of the RIXS spectrum resembles an inverted XAS profile for large negative detuning from the XAS edge (Magnuson *et al.*, 2003; Kikas *et al.*, 2004), giving an alternative way to measure the XAS and extended x-ray absorption fine-structure spectra (Kikas *et al.*, 2004; Błachucki *et al.*, 2014).

VI. DYNAMICS OF RESONANT SCATTERING

Despite the fact that RIXS and RAS measurements are essentially stationary experiments there are, as we later see, many spectral manifestations of nuclear dynamics in resonant scattering. The main characteristic time of this dynamics is the duration of the resonant x-ray scattering; this is due to a purely quantum mechanical effect of interference suppression of the long time contribution to the scattering amplitude. Using the variation of the duration time with the excitation energy detuning from the resonance Ω, one can monitor and even control various microscopic dynamical processes revealed by RIXS and RAS spectral features.

A. Scattering duration

The simplest way to rewrite the KH equations in the time domain is to apply the identity

$$\frac{1}{x+\imath\Gamma}=-\imath\int_0^\infty e^{\imath(x+\imath\Gamma)t}dt \tag{25}$$

to the wave packet $|\Psi\rangle$ [Eq. (21)], and to replace the Lorentzian $\Delta(x,\Gamma)=-\mathrm{Im}[1/(x+\imath\Gamma)]$ in the cross section (2) with an integral over time (25). Then using the completeness condition (23) and the identity $\exp(-\imath\varepsilon_f t)\nu_f\rangle=\exp(-\imath h_f t)\nu_f\rangle$, it is possible to rewrite the KH formula (2) in a temporal representation (Gel'mukhanov, Mazalov, and Kondratenko, 1977; Sałek, Gel'mukhanov, and Ågren, 1999)

$$\begin{aligned}\sigma(\omega',\omega)&=\frac{1}{\pi}\mathrm{Re}\int_0^\infty e^{\imath(\omega-\omega'-\omega_{f0}+\varepsilon_0+\imath\Gamma_f)t}\sigma(t)dt,\\ \sigma(t)&=\langle\Psi|e^{-\imath h_f t}|\Psi\rangle,\qquad |\psi_i(t)\rangle=e^{-\imath h_i t}D_{i0}|0\rangle,\\ |\Psi\rangle&=V_{fi}\int_0^\infty e^{-\Gamma t}e^{\imath\Omega t}e^{\imath\varepsilon_0 t}\psi_i(t)dt,\end{aligned} \tag{26}$$

where h_i is the nuclear Hamiltonian of the electronic state i. The time

$$\tau=\frac{1}{\Gamma-\imath\Omega}=|\tau|e^{\imath\phi},\qquad \Omega=\omega-\omega_{i0}, \tag{27}$$

of formation of the wave packet

$$|\Psi\rangle=V_{fi}\int_0^\infty e^{-(t/\tau)}e^{\imath\varepsilon_0 t}\psi_i(t)dt \tag{28}$$

is a complex number. This time determines the scattering duration (Skytt *et al.*, 1996; Cesar *et al.*, 1997; Gel'mukhanov *et al.*, 1999; Marchenko *et al.*, 2015), which is controlled experimentally by changing the detuning Ω of the frequency of the initial photon ω from the absorption resonance. In practice, the real time $|\tau|=1/\sqrt{\Gamma^2+\Omega^2}$ is used for a description of the scattering duration; its dependence on Γ and Ω is shown in Fig. 7(b). However, the roles of Γ and Ω in the scattering duration are qualitatively different.

The finite lifetime $1/\Gamma$ leads to the decay term $\exp(-\Gamma t)$ in the wave packet $|\Psi\rangle$ [Eq. (26)] and results in irreversible quenching of the excited state. Unlike Γ, the detuning Ω describes undamped, and in principle reversible, dephasing oscillations $\exp(\imath\Omega t)$. These sign-changing oscillations effectively quench the contribution to $|\Psi\rangle$ [Eq. (26)] from the times $t>1/|\Omega|$ due to the destructive interference of contributions from different t [Fig. 7(a)].

As we later see, the concept of the scattering time varied by the detuning (Skytt *et al.*, 1996; Cesar *et al.*, 1997; Gel'mukhanov *et al.*, 1999) allows one to study the electronic-vibrational dynamics with a femtosecond time resolution without using pump-probe methods with short (femtosecond) x-ray pulses. There is yet another powerful method for studying ultrafast dynamics, namely, core-hole-clock spectroscopy (Brühwiler, Karis, and Mårtensson, 2002). The method is used to study the charge-transfer dynamics at interfaces and surfaces with the lifetime of the core hole as an internal reference clock to follow the charge-transfer process.

In conclusion, we note that the time-dependent wave packet technique [Eq. (26)] is one of the main numerical methods for calculating RIXS and RAS spectra and dynamics.

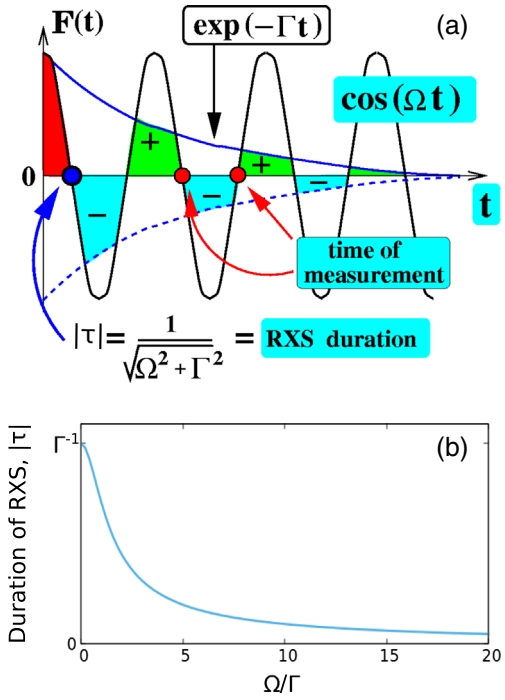

FIG. 7. (a) Irreversible $[\exp(-\Gamma t)]$ and reversible $[\cos(\Omega t)]$ quenching of scattering amplitude F. (b) Scattering duration $|\tau|=1/\sqrt{\Omega^2+\Gamma^2}$ (Skytt *et al.*, 1996; Cesar *et al.*, 1997; Gel'mukhanov *et al.*, 1999).

The advantages of this method relative to the time-independent KH formula (21) are most pronounced in the case of dissociative states.

B. Dynamical spatial quantum beats in quasielastic RIXS

In Secs. V.A and V.B we considered the interference of nearly degenerate electronic intermediate states. Often there are several core-excited states close in energy that can interfere in RIXS. Adachi, Kosugi, and Yagishita (2005) showed that the $1s$ core-ionized paramagnetic oxygen molecule has doublet (D) and quartet (Q) states, with total spin $S=1/2$ and $3/2$. Similarly, with x-ray excitation of the neutral O_2 molecule into the lowest unoccupied MO (LUMO) $1\sigma_g\rightarrow 3\sigma_u$, the doublet and quartet states of the ion, pairing with the electron spin on this orbital, form two closely spaced singlet Σ states (Fig. 8). These dissociative Σ states are also denoted by the letters D and Q. RIXS at excitation energies close to these interfering states was studied by Pietzsch *et al.* (2011) and Kimberg *et al.* (2012). Of particular interest here is the quasielastic scattering channel, the final state of which is the electronic ground state. An extended oscillatory progression in this channel experiences smoothly damped oscillations (Pietzsch *et al.*, 2011) (Fig. 9).

To investigate the unusual nature of these beats, one can employ the extended smoothly damped oscillatory progression in quasielastic RIXS characteristic of dissociation in the intermediate state (Couto *et al.*, 2017; Niskanen *et al.*, 2019; Vaz da Cruz *et al.*, 2019a, 2019b); see Sec. XI. We verify that the cross section for scattering to the final vibrational state ν is proportional to the FC factor $|\langle\nu|\Psi\rangle|^2$, which is simply the

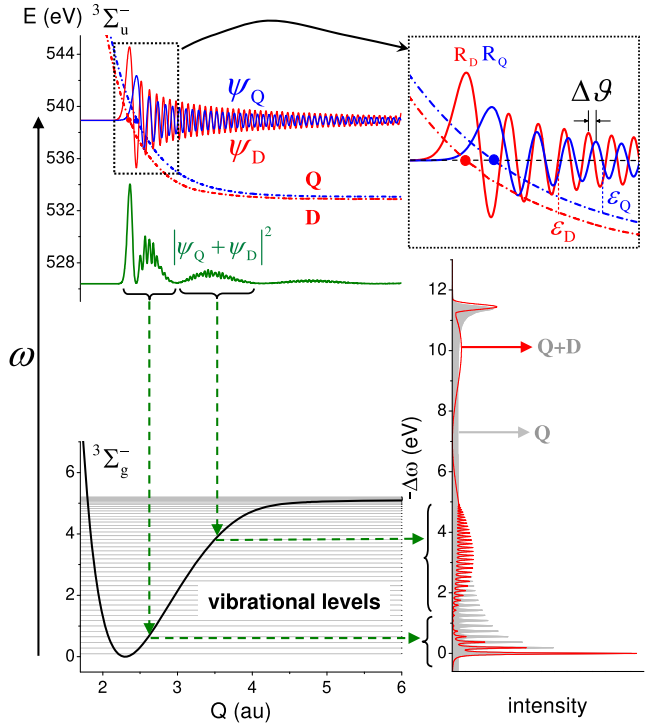

FIG. 8. Dynamical interference of the Q and D core-excited states of O_2 results in the quantum beats of the RIXS cross section. $\Delta\omega = \omega' - \omega$. From Pietzsch *et al.*, 2011.

square of the projection of the wave packet in an intermediate dissociative state

$$\Psi = \Psi_D + \Psi_Q \tag{29}$$

onto $|\nu\rangle$. The superposition expressed in Eq. (29) is valid since the wave packet propagates along the potential energy surface E simultaneously in the field of dissociative potentials $E_D(R)$ and $E_Q(R)$ of states D and Q. The idea now is to compute the phase shift $\Delta\vartheta$ between the wave packets Ψ_D and Ψ_Q. To do this, we use the semiclassical approximation

$$\Psi_i(R) \propto \exp\int_{R_i}^{R}\{\imath P_i(R')dR' - \Gamma dt\}, \qquad t = \frac{dR'}{v_i(R')}. \tag{30}$$

Here $i = D,\ Q$, $P_i(R') = \sqrt{2\mu\varepsilon_i(R)}$, where $\varepsilon_i(R) = E - E_i(R)$ and μ is the reduced mass. Calculations based on Eq. (30) (Pietzsch *et al.*, 2011) lead to the following expression for the phase shift that we are interested in:

$$\Delta\vartheta \approx (P_Q - P_D)(R - R_Q) = \Delta t\Delta E - \varphi, \tag{31}$$

where $\Delta t = (R - R_Q)/v$ is the propagation time of the wave packet to the point R with an average speed $v = (P_D + P_Q)/2\mu$, $\Delta E = E_Q(R_0) - E_D(R_0) \approx 2$ eV is the splitting between the states D and Q near the equilibrium bond length R_0, and φ is the phase shift independent of R. As a result, $|\Psi_D + \Psi_Q|^2$ experiences a beating with increasing bond length R,

$$\cos(\Delta t\Delta E + \varphi)e^{-2\Gamma\tau}, \tag{32}$$

which decays due to the finite lifetime of the intermediate state $2/\Gamma$. Despite the semiclassical approximation (30), Eq. (32) perfectly explains the spatial modulation of the squared wave packet $|\Psi_D + \Psi_Q|^2$, strictly computed by the quantum wave packet method shown in Fig. 8.

With the help of the reflection principle (Gel'mukhanov and Ågren, 1996b; Schinke, 2009) it is possible to obtain an approximate spectral shape from the spatial distribution of the squared nuclear wave function, namely, by reflecting $|\Psi_D + \Psi_Q|^2$ onto the potential energy curve (PEC) of the final state, as illustrated in Fig. 8. This gives a unique opportunity to image nuclear wave functions (Gel'mukhanov and Ågren, 1996b; Pietzsch *et al.*, 2011; Kjellsson *et al.*, 2021). Altogether we obtain a clear physical picture of the effect. The discussed quantum beats were also previously observed in RAS spectra from O_2 (Feifel *et al.*, 2008). Figure 8 shows that the reflection principle allows one to solve an inverse problem: to reconstruct approximately the square of the wave packet $|\Psi|^2$ from the RIXS or RAS spectrum.

In conclusion, we note that the considered effect of quantum beats is inherently dynamical, occurring when the coherent evolution of nuclei along two potential surfaces plays a decisive role. Furthermore, the role of interference between the direct ionization and different resonant ionization channels was studied in the C-K RAS spectra of the CH_3Cl molecule (Nandi *et al.*, 2017).

C. Dynamical collapse of vibrational structure and quenching of soft modes

We proceed by considering another dynamic effect that is inherent in all RIXS spectra and has also been observed in a number of RAS experiments, namely, the collapse of vibrational structure. We discuss two qualitatively different

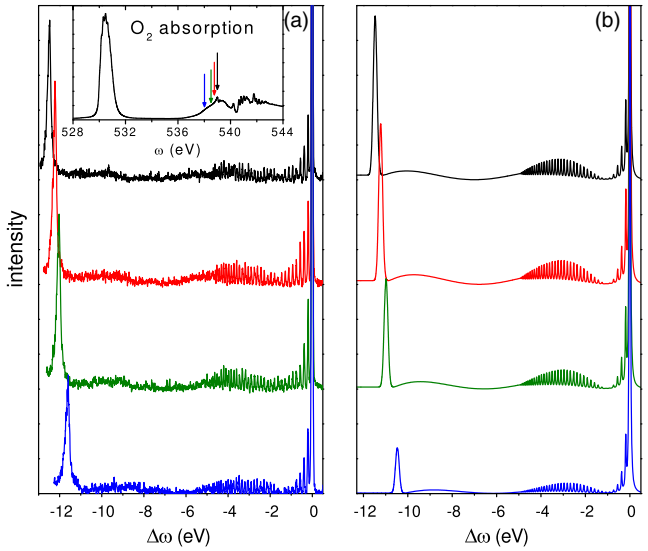

FIG. 9. (a) Experimental and (b) theoretical RIXS spectra of O_2 for $\chi = 90°$ for excitation energies ω shown by arrows in the XAS spectrum. $\Delta\omega = \omega' - \omega$. Adapted from Pietzsch *et al.*, 2011.

transition schemes that are typical for both RIXS and RAS processes.

Collapse of type 1.—We first consider a special case in which the shapes of PECs of the initial $[E_0(R)]$ and final $[E_f(R)]$ states are identical. This is the case in quasielastic RIXS, where the final state is the same as the initial state. When the photon frequency coincides with the vertical transition frequency $[\Omega = \omega - \omega_{i0}(R_0) = 0]$, the scattering duration is quite long ($|\tau| = 1/\Gamma$) [Eq. (27)], so the initial wave packet $|0\rangle$ has time to propagate and get deformed in the intermediate state. Because of differences in the shape of the intermediate $[E_i(R)]$ and final $[E_f(R)]$ states' PEC and the small lifetime broadening, the RIXS spectrum shows a vibrational structure. We now tune the excitation frequency away from the absorption resonance

$$|\Omega| \equiv |\omega - \omega_{i0}(R_0)| \gg \varepsilon_0, \tag{33}$$

making the scattering duration $|\tau|$ [Eq. (27)] shorter than the vibrational period $T = 4\pi/\varepsilon_0$. In this case, the nuclear wave packet $|\Psi\rangle$ has no time to move away from the vertical transition point R_0, and it decays to the final state without changing the original shape ($|\Psi\rangle = |0\rangle$). The amplitude of the RIXS is now proportional to the FC amplitude of the direct transition from the initial to the final state

$$F_f \propto \langle \nu_f | 0 \rangle, \qquad |\tau| = \frac{1}{\sqrt{\Gamma^2 + \Omega^2}} \ll T. \tag{34}$$

Taking into account the identical shape of the initial and final states' PEC, and hence $\langle \nu_f | 0 \rangle = \delta_{\nu_f,0}$, we conclude that at large detuning the spectrum collapses into a single vibrational peak $\nu_f = 0$. Here it is assumed that only lowest vibrational state is initially populated in the ground electronic state. Owing to the dependence of Eq. (34) on the vibration frequency, the "soft" vibrational modes in polyatomic molecules collapse before stiff modes as a function of detuning (Vaz da Cruz *et al.*, 2019b).

This effect, which was predicted by Gel'mukhanov, Privalov, and Ågren (1997a), almost immediately received experimental confirmation in RAS of the CO molecule (Sundin *et al.*, 1997), and later in RAS of the N_2 molecule (Feifel *et al.*, 2002). This collapse in quasielastic RIXS has been observed for different systems, including liquid acetone (Sun *et al.*, 2011), liquid ethylene (Hennies *et al.*, 2005), liquid methanol (Vaz da Cruz *et al.*, 2019b), and gaseous and liquid water (Fig. 10) (Vaz da Cruz *et al.*, 2017). Recently the dynamical collapse of the vibrational structure made it possible to extract the electron-phonon interaction constant ≈0.17 eV from the Ω dependence of the phonon resonance in a RIXS experiment (Rossi *et al.*, 2019a) on the superconductor $NdBa_2Cu_3O_3$.

Collapse of type 2.—The second type of dynamic collapse of the vibrational structure is realized in systems where the shapes of PECs of the intermediate and final states coincide (Sundin *et al.*, 1997; Piancastelli *et al.*, 2020). This situation is realized in RIXS transitions between two core-hole states, such as K_α RIXS in HCl or H_2S molecules (Simon *et al.*, 2006; Piancastelli *et al.*, 2020),

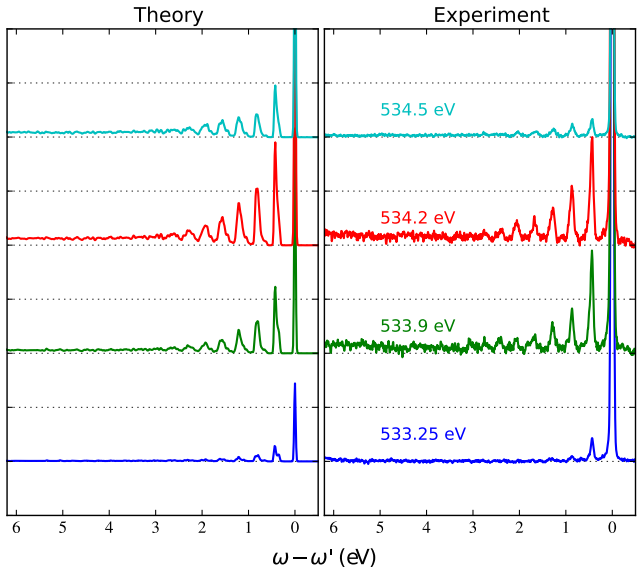

FIG. 10. Detuning from the absorption resonance leads to a collapse of the vibrational structure (Gel'mukhanov, Privalov, and Ågren, 1997a) in RIXS of liquid water (Vaz da Cruz *et al.*, 2019a).

$$\omega + \mathrm{HCl} \rightarrow \mathrm{HCl}(1s^{-1}\sigma^*) \rightarrow \mathrm{HCl}(2p^{-1}\sigma^*) + \omega'. \tag{35}$$

Since the intermediate ($|1s^{-1}\sigma^*\rangle$) and final ($|2p^{-1}\sigma^*\rangle$) states differ only by the character of the core hole, the PEC shapes for these states match with high precision (Simon *et al.*, 2006). In spite of the short lifetime ($1/2\Gamma \approx 1$ fs) of the state $|1s^{-1}\sigma^*\rangle$, the narrowing of both components of the $K_{\alpha_{1,2}}$ doublet when $\Omega \rightarrow 0$ unambiguously indicates the dynamical nature of the collapse (Fig. 11).

This phenomenon is explained by the fact that for $\Omega = 0$ the spectral form of RIXS is determined by the set of frequencies of the emission transitions $\omega_{if}(R) = E_i(R) - E_f(R)$, which collapses into a single narrow resonance when $E_i(R)$ and $E_f(R)$ are parallel ($\langle \nu_f | \nu_i \rangle = \delta_{\nu_f,\nu_i}$). At large detuning, the direct channel is strong [see Eq. (34)] and the vibrational broadening occurs (see Fig. 11) as $\langle \nu_f | 0 \rangle \neq \delta_{\nu_f,0}$ due to the different shapes of $E_f(R)$ and $E_0(R)$. Thus, unlike the collapse of the first type,

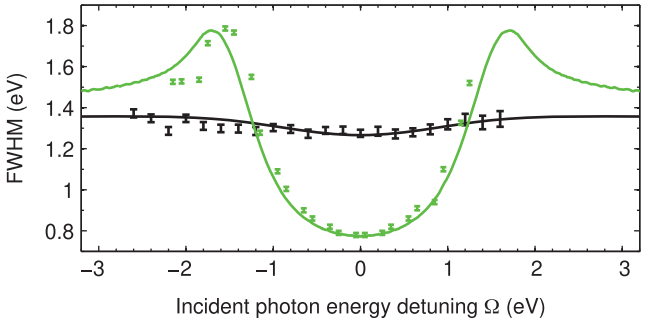

FIG. 11. Collapse of vibrational structure in RIXS. Full width at half maximum (FWHM) of the I L_3-$N_{4,5}$ of CH_3I (black) and Cl K-L of CH_3Cl (green or gray) emission lines as a function of the incident photon energy detuning with respect to the resonance energy. Adapted from Marchenko *et al.*, 2011.

the broadening occurring at large $|\Omega|$ is followed by a narrowing of the peak at $\Omega \to 0$.

Additional confirmation of the dynamic nature of the phenomenon is obtained from a comparison of the Ω dependence of the resonance width for the molecules CH_3Cl and CH_3I (Fig. 11). The intermediate state lifetime with a hole in the L shell of the iodine atom (0.23 fs) in CH_3I is much shorter than that of the intermediate state with a hole in the K shell of the chlorine atom (0.94 fs) in the CH_3Cl molecule. This means that during the lifetime of the intermediate state the nuclei in the CH_3I molecule have much less time to shift their position than those in the CH_3Cl molecule. This explains the less pronounced line narrowing for CH_3I compared to CH_3Cl. The second type of the collapse of the vibrational structure was first observed in RAS of the CO molecule (Sundin *et al.*, 1997). Note that observation of the collapse provides information about the PECs of the states involved in the process.

D. Extraction of potential energy surfaces from RIXS and RAS spectra

Thanks to modern spectrometers with superhigh resolution, in many cases it has become possible to resolve vibrational structure in the RIXS and RAS spectra, which allows one to extract PECs along different vibrational modes from the experimental spectra, as demonstrated in a number of cases (Miron *et al.*, 2012; Schreck *et al.*, 2016; Marchenko *et al.*, 2017; Eckert *et al.*, 2018; Vaz da Cruz *et al.*, 2019a). For example, the RIXS and RAS spectra made it possible to determine from experimental data the dissociative potentials of the intermediate and final single and double hole states of the CH_3Cl and CH_3I molecules (Marchenko *et al.*, 2017). The extended vibrational progression of $1s_O^{-1}\pi^{*1}$ of the quasielastic RIXS channel of liquid acetone and liquid acetone mixed with chloroform made it possible to determine the potentials of the ground electronic state along the C = O coordinate (Schreck *et al.*, 2016). The potentials of the final ion states $1^2\Pi_g$ and $1^2\Phi_g$ of the N_2 molecule were extracted from the RAS spectra (Miron *et al.*, 2012; Kimberg and Miron, 2014).

Note that in a disordered system like a liquid one it is impossible to determine a unique potential energy surface of a molecule due to the fluctuating local environment around it; see Sec. XI.C.3. Therefore, only the confidence interval of the PEC's distribution can be extracted from the experiment, as was done for liquid water (Vaz da Cruz *et al.*, 2019a).

It is advisable to illustrate one of the methods of extracting potential energy surface details using the example of RIXS from the water molecule, which is limited to symmetric and antisymmetric stretching vibrations. Figure 12 shows the potential energy surfaces of the two lowest intermediate core-excited $|1s_O^{-1}4a_1^1\rangle$ (dissociative) and $|1s_O^{-1}2b_2^1\rangle$ (bound) states (Eckert *et al.*, 2018), which were selectively populated by changing the frequency ω of the x rays. The excited nuclear wave packet propagates along the individual O–H bonds in the first (dissociative) case and simultaneously along both O–H bonds in the second case. Since the emission transition to the core hole is determined by the projection of the wave packet onto the ground state, we have a unique opportunity to obtain

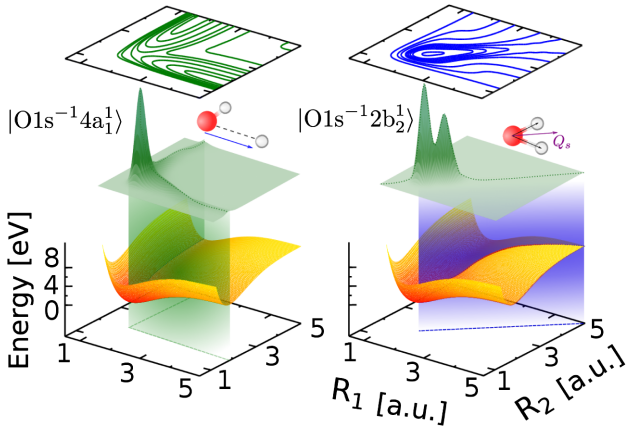

FIG. 12. During the emission transition, a nuclear wave packet of an intermediate state, being projected onto the ground state, allows one to obtain a slice of the potential surface of the ground state along the direction of propagation of the wave packet.

specific cuts through the potential surface along and between the O–H bonds (Fig. 12) by tuning the photon frequency ω to specific intermediate states with the corresponding orientation of the potential valley surfaces (Eckert *et al.*, 2018).

E. RIXS and RAS under dissociation in core-excited state

Figure 9 shows an unusually narrow resonance near $\Delta\omega \equiv \omega' - \omega = -11$ eV. The reason for this, the so-called atomic peak, is emission transition in the core-excited oxygen atom in the region of dissociation of a core-excited oxygen molecule $[O_2]^* \to O^* + O$. This phenomenon was discovered by Morin and Nenner (1986), who studied RAS spectra of the HBr molecule core excited into a dissociative state. To date this effect has been observed in the RIXS and RAS spectra of many diatomic and polyatomic molecules (Björneholm *et al.*, 1997; Sałek *et al.*, 2001; Fuchs *et al.*, 2008; Pietzsch *et al.*, 2011; Kimberg *et al.*, 2012; Couto *et al.*, 2017; Ertan *et al.*, 2018).

As we later see, the physical mechanism inherent in this effect served as an impetus for the discovery of new phenomena. Figure 13 illustrates the physical picture of the

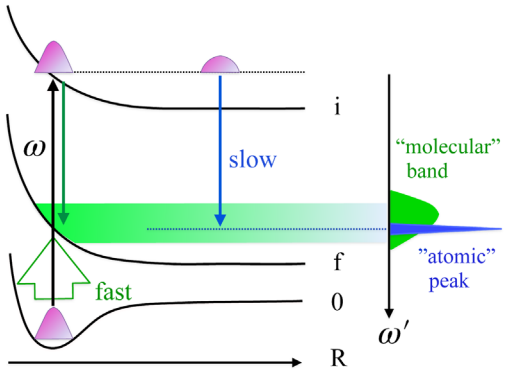

FIG. 13. Physical picture of the formation of fast (molecular) and slow (atomic) scattering channels. In the limit of fast scattering, RIXS corresponds to a sudden transition directly to the final state $0 \to f$ [Eq. (34)].

process that occurs in both RIXS and RAS. The photon excites the initial wave packet $|0\rangle$ to the point of vertical transition ($R = R_0$), where the kinetic energy is zero. We see two qualitatively different peaks, narrow and wide. A wide peak corresponds to the fast decay of the intermediate state to the final one near the equilibrium distance R_0, where the kinetic energy is again close to zero (classical turning point) and the energy of the final state is $E_f(R_0)$. This explains the Raman dispersion law [Eq. (6)] of this so-called molecular peak. The width of this peak is determined (Gel'mukhanov and Ågren, 1999) by the spatial size of the initial vibrational wave function $|0\rangle$. A narrow atomic peak is formed in the dissociation region, far from the equilibrium distance, where the potential is $E_i(R) = E_i(\infty) = \text{const}$. In this region, the decay occurs with the conservation of kinetic energy $P^2/2\mu$ (Gel'mukhanov and Ågren, 1999) and the total energy of the final state $P^2/2\mu + E_i(\infty)$ is a continuous function of nuclear momentum P. As a result of integration over P in the expression for the cross section, the Lorentzian responsible for the Raman dispersion (6) disappears. As a result of this, the position of the narrow resonance ceases to depend on the frequency of the initial photon ω and is equal to the frequency of the emission transition in the core-excited fragment of dissociation (in the case of RAS, $\omega' \to E$)

$$\omega' = E_i(\infty) - E_f(\infty) = \text{const}. \tag{36}$$

For the same reason, the width of the resonance is approximately equal to the natural width of the intermediate state Γ. The transitional region, where $E_i(R)$ deviates slightly from the constant, also contributes to the formation of the narrow peak. Therefore, its width usually exceeds Γ. Owing to the fact that the atom is a fragment of dissociation for diatomic molecules, the name "atomic peak" is generally used. In the case of polyatomic molecules, the fragments of dissociation are not only atoms but molecules. In this case the "atomic" peak may have a vibrational structure characteristic of this fragment (Ertan *et al.*, 2018).

For the appearance of an atomic peak, time is required. This is the time of propagation of the wave packet into the region of dissociation. Consequently, the atomic peak should disappear (Sałek, Gel'mukhanov, and Ågren, 1999) with a shorter scattering time $|\tau|$ achieved by increasing $|\Omega|$. This dynamic effect was experimentally observed by Björneholm *et al.* (1997) and Sałek *et al.* (2001).

F. Dynamical interference hole

Owing to the difference in dispersion law of the molecular [Eq. (6)] and atomic [Eq. (36)] peaks, these peaks can intersect at the corresponding initial photon frequency ω. Quantum mechanically, the molecular and atomic scattering channels are indistinguishable since they lead to the same final state of the continuous spectrum. Therefore, interference from these channels should be expected. In the case of destructive interference, a narrow dip or spectral "hole" may appear in the region of intersection of the peaks. This effect, predicted by Sałek, Gel'mukhanov, and Ågren (1999), was subsequently experimentally confirmed by Feifel *et al.* (2000) in the RAS from the HCl molecule (Fig. 14), where the isotopic sensitivity evidences the dynamical origin of the effect (Sałek, Gel'mukhanov, and Ågren, 1999).

VII. DOPPLER EFFECT CAUSED BY ULTRAFAST DISSOCIATION

The atomic peak is formed far from the equilibrium point R_0, where the potentials of the intermediate $[E_i(R)]$ and final $[E_f(R)]$ states are practically constant, and therefore the fragment of dissociation moves freely with the momenta $\mathbf{P}_i$ and $\mathbf{P}_f$, respectively. This allows one to obtain the momentum conservation law from the FC amplitude of the Auger transition (Gel'mukhanov, Ågren, and Sałek, 1998), $\langle \mathbf{P}_f | \exp(-\imath \mathbf{p}\cdot\mathbf{R}) | \mathbf{P}_i \rangle \propto \delta(\mathbf{P}_f + \mathbf{p} - \mathbf{P}_i)$. Consider a RAS of diatomic molecule in the soft x-ray region, where the small photon momentum $\mathbf{k}$ can be neglected in favor of the Auger electron momentum $\mathbf{p}$:

$$k \ll p. \tag{37}$$

Applying the momentum and energy conservation laws for the transition from the intermediate core-excited to the final state, we find the energy shift of the Auger electron ($E = k^2/2$) (Gel'mukhanov, Ågren, and Sałek, 1998)

$$E = \omega_{if}(\infty) + \mathcal{D} + E_{\text{rec}}, \tag{38}$$

which consists of the electron Doppler shift $\mathcal{D}$ and the recoil energy E_{rec}, experienced by the dissociation fragment when the Auger electron leaves it:

$$\mathcal{D} = \mathbf{p}\cdot\mathbf{v}, \qquad E_{\text{rec}} = \frac{p^2}{2\mu}. \tag{39}$$

Here $\omega_{if}(\infty) = E_i(\infty) - E_f(\infty)$ is the transition energy and $\mathbf{v} = \mathbf{P}_f/\mu$ is the fragment velocity in the final state. We neglect here the small recoil energy. Taking into account the kinetic energy released upon the dissociation $\Delta E = \mu v^2/2$–5 eV, we obtain for atoms of the oxygen type $\mathcal{D} \sim 1$ eV, which is more than an order of magnitude greater than Doppler broadening due to thermal motion. This makes the effect easily observable (Gel'mukhanov, Ågren, and Sałek, 1998), at least by measuring the broadening of the atomic peak.

A. Doppler splitting of RAS resonance

There is an elegant way to visualize the effect under discussion (Björneholm *et al.*, 2000). To do this, remember that the probability of excitation of a molecule is highly anisotropic,

$$\sigma_{\text{abs}} \propto (\mathbf{e}\cdot\mathbf{d}_{i0})^2, \tag{40}$$

and it reaches a maximum when $\mathbf{d}_{i0} \| \mathbf{e}$. When $1s \to \sigma^*$ is excited, the dipole moment of the transition $\mathbf{d}_{i0}$ is parallel to the axis of the molecule $\mathbf{R}$ along which it dissociates. This means that the velocity $\mathbf{v}$ of the fragment is predominantly parallel or antiparallel to the polarization vector $\mathbf{e}$. Thus, half

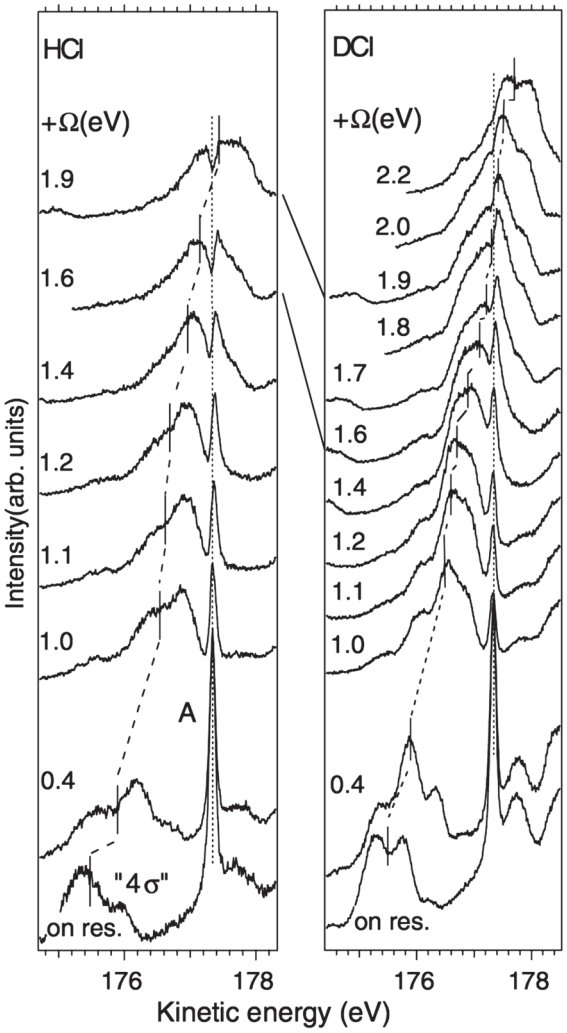

FIG. 14. RAS spectra of HCl and DCl. The spectral hole seen in HCl for $\Omega = 1.9$ eV has completely disappeared for DCl for the same detuning value, which is in full agreement with the theoretical prediction (Sałek, Gel'mukhanov, and Ågren, 1999). From Feifel *et al.*, 2000.

of the fragments move preferentially along **e**, and the other half move against **e**.

If the electron detector is installed on the axis **e**, the atomic resonance splits into two peaks with the opposite Doppler shifts: $\mathcal{D} = \pm pv$. $\mathcal{D} \approx 0$ if the momentum of Auger electron **p** is perpendicular to **e**. Experimental data (Travnikova *et al.*, 2010) on Fig. 15 illustrate the Doppler splitting at $\mathbf{p}\|\mathbf{e}$ and its absence if $\mathbf{p}\perp\mathbf{e}$ for the RAS of the SF_6 molecule when ω is tuned to the F $1s \rightarrow a_{1g}^*$ dissociative resonance (688 eV). The Doppler splitting was observed also for the circular polarized light when the Auger electron was detected in the polarization plane (Travnikova *et al.*, 2010).

It is necessary to explain why Doppler splitting was not observed in RIXS. The main reason is the small momentum of the photon [Eq. (37)], which makes the photon Doppler shift negligible relative to the width of the atomic peak and the electronic Doppler shift ($kv \ll pv \sim 1$ eV).

The effect of Doppler splitting has been identified in a few applications. Doppler Auger splitting of the atomic peak confirmed in RAS experiments with molecules O_2

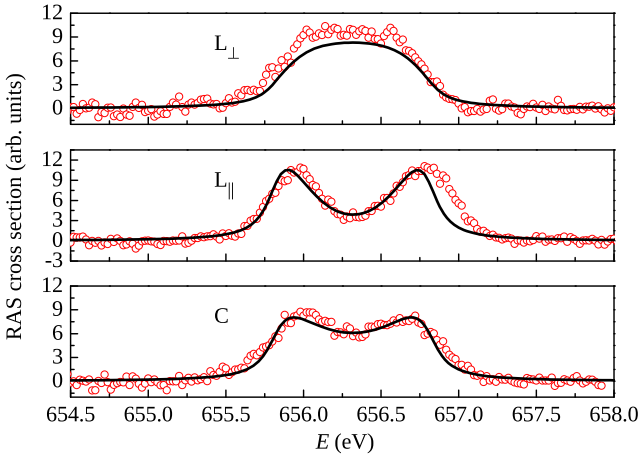

FIG. 15. Doppler splitting of the atomic peak in RAS from the SF_6 molecule. $L_\parallel$ and $L_\perp$ mark parallel ($\mathbf{e}\|\mathbf{k}$) and perpendicular ($\mathbf{e}\perp\mathbf{k}$) geometries for linear polarization. C, circular polarization. Circles show the experimental data. The theoretical simulations are indicated by sold lines. From Travnikova *et al.*, 2010.

(Björneholm *et al.*, 2000; Baev *et al.*, 2002), CO (Sorensen *et al.*, 2007), O_3 (Rosenqvist *et al.*, 2001), CF_4 (Ueda *et al.*, 2003), CH_3F (Liu *et al.*, 2005), and SF_6 (Kitajima *et al.*, 2003; Travnikova *et al.*, 2010). The effect unequivocally allows us to establish that the resonance under study is an atomic peak, which, in turn, unambiguously indicates dissociation in the intermediate state. The magnitude of the splitting determines an important parameter, namely, the kinetic energy released during dissociation (Björneholm, 2001). The dependence of the Doppler splitting on ω provides information on the femtosecond dynamics of dissociation (Björneholm, 2001; Kitajima *et al.*, 2003).

B. Einstein-Bohr recoiling double-slit gedanken experiment performed at the molecular level

The Doppler effect in RAS recently allowed Liu *et al.* (2015) to experimentally confirm the validity of Bohr's reasoning in his discussion with Einstein about wave-particle duality in a YDSE experiment on two slits [Fig. 16(a)], where they discussed the question of whether the measurement of the momentum exchange between the particle and the movable slit, highlighting the slit through which the particle passed, can destroy the interference structure in the YDSE (Bohr, 1983). Einstein believed that the measurement of recoil on the moving slit after the particle has passed cannot affect the process and the interference on the screen should remain. Bohr, on the basis of the uncertainty principle, argued that this is impossible: any attempt to select the slit (particle path) leads to degradation of the interference structure [Fig. 16(c)].

Two RAS channels were studied, with a bound $|1\sigma_g^{-1}4p\sigma_u\rangle$ and a dissociative $|1\sigma_g^{-1}3\sigma_u\rangle$ core-excited state. These states decay to the final state, emitting Auger electrons detected in coincidence with the product of fast dissociation in one of the final states O^+. The direction of cation propagation "fixes" the molecular axis. A channel with a bound state corresponds to motionless slits [Figs. 16(a) and 16(b)], where the Auger electron momentum is transferred to the entire molecule

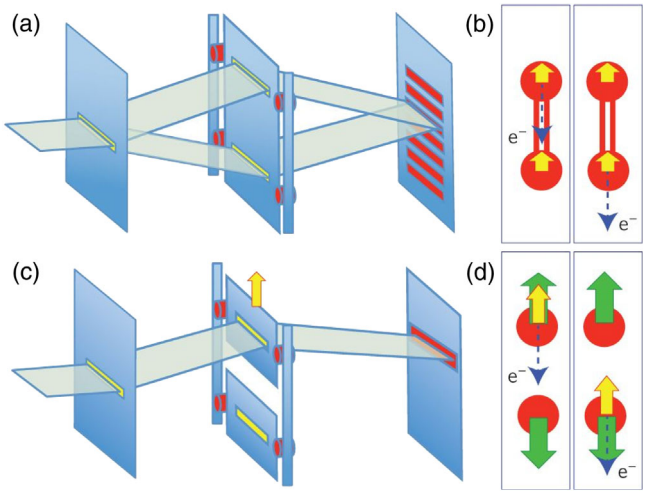

FIG. 16. Analogy of the YDSE experiment with macroscopic slits and RAS implementation of the YDSE experiment with fixed-in-space oxygen molecules. The RAS experiment was performed with oriented molecules by simultaneously detecting the electron and the cation O^+ using the coincidence technique. From Liu *et al.*, 2015.

(center of gravity) O_2. In this case, the experiment shows the interference structure $\cos(\mathbf{p}\cdot\mathbf{R}) = \cos(pR\cos\beta)$ [Figs. 17(a) and 17(b)], as it should be for stationary atoms or slits. A similar structure was previously discussed for photon scattering [Eq. (12)]. In the case of a dissociating molecule, the momentum is transmitted to a freely moving atom (mobile slit), from which the Auger electron is ejected, as shown in Figs. 16(c) and 16(d). Recall that Auger decay in a freely moving atom corresponds to an atomic peak and this atom is marked with a Doppler shift. This shift has the opposite sign for the second atom moving in the opposite direction.

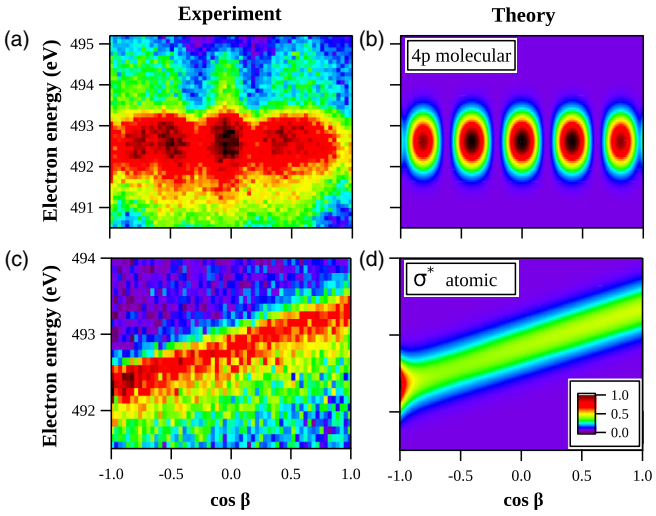

FIG. 17. Both (a) experiment and (b) theory display the interference pattern for the molecular band. (c),(d) The absence of the interference structure of the atomic peak upon dissociation in the $|1\sigma_g^{-1}3\sigma_u\rangle$ state, in contrast to the "rigidly bonded" atoms in the bound $|1\sigma_g^{-1}4p\sigma_u\rangle$ condition, is consistent with Bohr's conclusion. Here β is the angle between the Auger momenta of the electron and the cation O^+. Adapted from Liu *et al.*, 2015.

Figures 17(c) and 17(d) demonstrate the absence of any interference structure, which is consistent with Bohr's prediction.

VIII. DYNAMICAL MANIFESTATIONS OF ELECTRON-VIBRATIONAL INTERACTION

Previously, we investigated resonance scattering in the framework of the adiabatic BO approximation, which allows us to separate nuclear and electronic degrees of freedom. The justification for this approximation is the smallness of the electron mass in comparison with the mass of nuclei. However, instead of this rather crude criterion, one should use the strict condition of applicability of the BO approximation (Köuppel, Domcke, and Cederbaum, 2007)

$$|V_{\rm VC}| = |\langle\psi_i|V|\psi_j\rangle| \ll |E_i(R) - E_j(R)|, \tag{41}$$

where V is the operator of electron-vibrational, also known as VC, or electron-phonon (in the case of a solid), interaction. This relation means that the BO approximation is completely violated if the diabatic potential surfaces intersect or are close in the region of the spectral transition. The corresponding adiabatic surfaces, computed using most conventional quantum-chemical methods, are split at the intersection point of the diabatic surfaces at a distance of $2|V_{\rm VC}|$. According to calculations, typical magnitude of this splitting

$$2|V_{\rm VC}| \sim \omega_0 \tag{42}$$

is comparable with the vibrational frequency ω_0, which indicates a need to take into account electron-vibrational interaction (Köuppel, Domcke, and Cederbaum, 2007) in this case. Without claiming to give a complete overview of this dynamic problem, we consider two important cases, namely, violation of the BO approximation in the intermediate and final states in soft x-ray RIXS process.

A. Breakdown of selection rules in RIXS

In this section, we restrict ourselves to analyzing the situation in symmetric molecules (CO_2, C_2H_4, etc.), which also allows us to understand the physics of the phenomenon in crystals. Omitting the details of the theory, which is described in the literature (Cesar *et al.*, 1997; Gel'mukhanov, Privalov, and Ågren, 1997b; Privalov, Gel'mukhanov, and Ågren, 1999; Hennies *et al.*, 2007; Köuppel, Domcke, and Cederbaum, 2007), we focus on the physical picture of the phenomenon, considering RIXS in the planar symmetric C_2H_4 ethylene molecule with gerade ground state $|^1A_g\rangle$ (Hennies *et al.*, 2005, 2007). The excitation photon frequency ω is set near the resonance with the transition of the carbon $1s$ electron to the first unoccupied MO $1b_{2g}(\pi^*)$. We consider the emission transitions from the first occupied MOs $1b_{1u}$, $1b_{1g}$, $3a_g$, and $1b_{2u}$, taking into account that, due to the weak interaction of $1s$ electrons localized at different carbon atoms, the $1s$ shell is only slightly split ($2|V_{\rm VC}| < 0.1$ eV) to gerade $1a_g$ and ungerade $1b_{3u}$ levels. Applying the dipole selection rules to the absorption and emission processes and ignoring the nuclear vibrations for a while, we obtain the following allowed transition for RIXS:

$$\omega + |^1A_g\rangle \to |1b_{3u}^{-1}1b_{2g}^1\rangle \to \begin{cases} |1b_{1g}^{-1}1b_{2g}^1\rangle, \\ |3a_g^{-1}1b_{2g}^1\rangle. \end{cases} \tag{43}$$

Scattering into ungerade final states $|1b_{2u}^{-1}1b_{2g}^1\rangle$ and $|1b_{1u}^{-1}1b_{2g}^1\rangle$ is prohibited. We now take into account the antisymmetric C-H stretch vibration b_{3u}. During this vibration, a periodic symmetry breaking occurs, which mixes intermediate states of opposite parity

$$|\psi\rangle = a|1b_{3u}^{-1}1b_{2g}^1\rangle + b|1a_g^{-1}1b_{2g}^1\rangle, \tag{44}$$

thereby periodically creating a hole in the $1a_g$ shell, and therefore opening the forbidden decay channels to ungerade final states $|1a_g^{-1}1b_{2g}^1\rangle \to |1b_{2u}^{-1}1b_{2g}^1\rangle$ and $|1a_g^{-1}1b_{2g}^1\rangle \to |1b_{1u}^{-1}1b_{2g}^1\rangle$; see Fig. 18.

B. Dynamical restoration of selection rules

The described dynamic symmetry breaking takes time. Indeed, a violation of the symmetry will occur as a result of the symmetry breaking vibration, which is characterized by a period of vibration $2\pi/\omega_0$. Symmetry breaking will not occur if the scattering duration [Eq. (27)] $|\tau|$ is shorter than $2\pi/\omega_0$. Considering the dependence [Eq. (27)] $|\tau|$ on the detuning Ω, we should expect a violation of the selection rules at $\Omega \approx 0$ and their restoration with increasing $|\Omega|$ ($|\tau| < 2\pi/\omega_0$) (Cesar *et al.*, 1997; Gel'mukhanov, Privalov, and Ågren, 1997b; Privalov, Gel'mukhanov, and Ågren, 1999).

Given that a qualitative picture of the phenomenon explains the results of RIXS experiments with the ethylene (Hennies *et al.*, 2005, 2007) and CO_2 (Skytt *et al.*, 1996; Cesar *et al.*, 1997; Maganas *et al.*, 2014; Söderström *et al.*, 2020) molecules, presented in Figs. 18 and 19, respectively, as well as RIXS experiments with the benzene (Hennies *et al.*, 2007) molecule and crystalline silicon (Shin *et al.*, 1996) and graphite (Harada *et al.*, 2004).

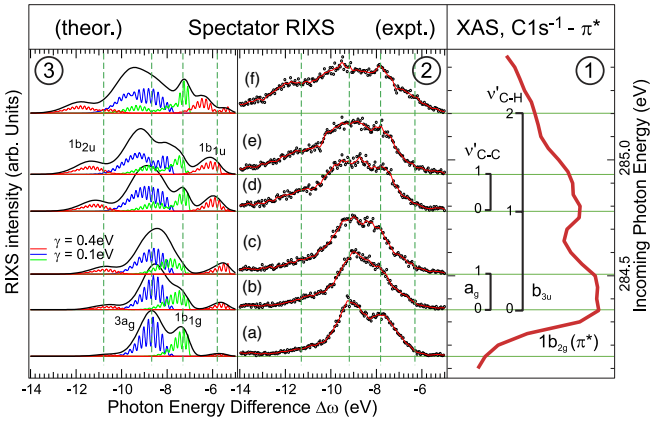

FIG. 18. Restoration of the selection rules in RIXS of the C_2H_4 molecule for $C1s \to 1b_{2g}$ core excitation (Hennies *et al.*, 2005, 2007). $\Delta\omega = \omega' - \omega$. RIXS to the final (forbidden by symmetry) ungerade states $|1b_{2u}^{-1}1b_{2g}^1\rangle$ and $|1b_{1u}^{-1}1b_{2g}^1\rangle$ becomes forbidden upon shortening the scattering duration $|\tau|$ by increasing the detuning $|\Omega|$. From Hennies *et al.*, 2005.

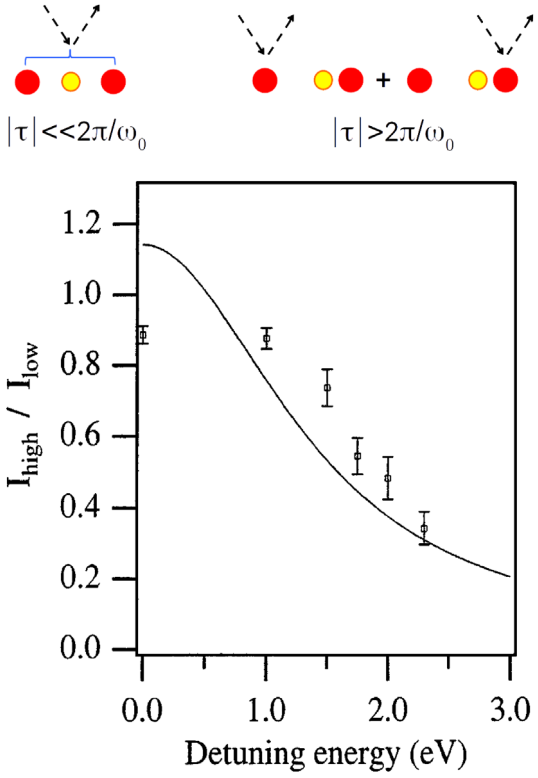

FIG. 19. A decrease in the relative intensity of the symmetry-forbidden peak $|1\pi_g^{-1}2\pi_u^1\rangle$ in the RIXS of the CO_2 molecule. Upper panel: symmetry breaking in the course of the vibration. Adapted from Skytt *et al.*, 1996.

C. Electron-vibrational interaction in the final states of RIXS

In Sec. VIII.B, the mixing of electronic states in symmetric systems by exclusively electron-vibrational interaction was considered. In most cases, the diabatic Hartree-Fock (HF) electronic states of $\psi_i^{\rm el}$ are mixed by the Coulomb interaction V_{ij}. The effect of such a mixing of close-lying configurations

$$\Psi(R, r, t) = \sum_i \psi_i(R, t)\psi_i^{\rm el}(r) \tag{45}$$

may be important in both the intermediate and final states (Vaz da Cruz *et al.*, 2019b; Ekholm *et al.*, 2020). The mixing of the electronic states with different potential energy curves $E_i(R)$ strongly affects the electron-vibrational spectrum since the nuclear wave packet propagating near the crossing of the diabatic states $E_i(R)$ and $E_j(R)$ jumps between the PECs according to

$$\imath\frac{\partial\psi_i}{\partial t} = \sum_j h_{ij}\psi_i,$$
$$h_{ij} = \delta_{ij}\left(-\frac{d^2}{dR^2} + E_i(R)\right) + (1-\delta_{ij})V_{ij}. \tag{46}$$

This can be demonstrated in RIXS from the CO molecule ($X^1\Sigma^+[1\sigma^1 2\sigma^2 3\sigma^2 1\pi^4 5\sigma^2]$) with scattering through the intermediate $O1s^{-1}$ state $|1\sigma^{-1}2\pi^1\rangle$. Here the strong state mixing happens in the final state manifold (Couto *et al.*, 2016a, 2016b)

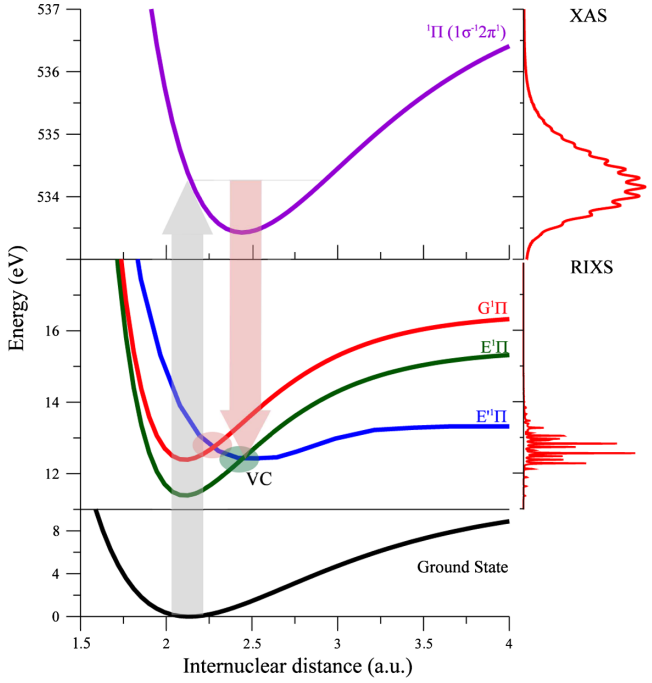

FIG. 20. Potential energy curves of the ground, core-excited O $1s^{-1}2\pi^1$ and final valence-excited states of CO. Right panel: XAS and RIXS spectra. Adapted from Couto *et al.*, 2016b.

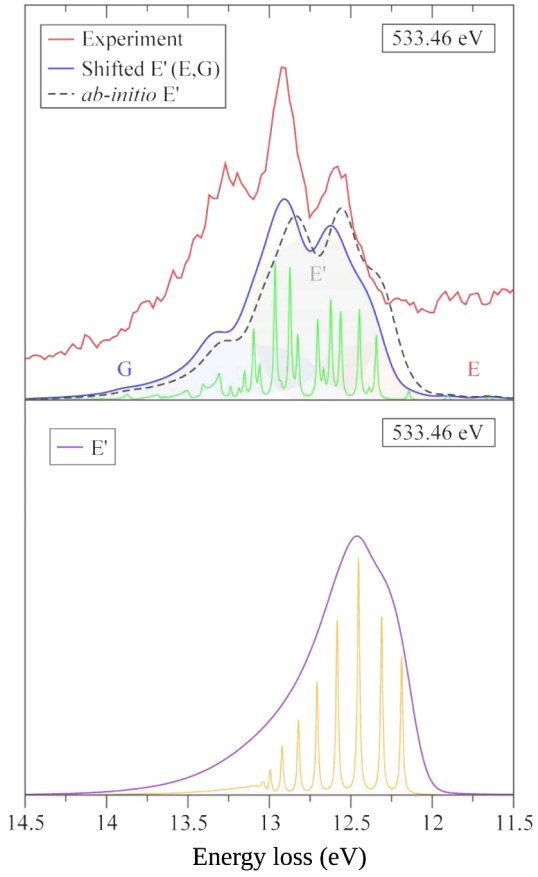

FIG. 21. The experimental and theoretical RIXS spectra of CO vs energy loss $\omega - \omega'$. Lower panel: RIXS profile computed without accounting for the VC between the final states. Adapted from Couto *et al.*, 2016b.

due to the intersection of the PECs of the $E^1\Pi(5\sigma^{-1}3p_\pi^1)$ and $G^1\Pi(5\sigma^{-1}3d_\pi^1)$ states with the PEC of the state $E'^1\Pi(4\sigma^{-1}2\pi^1)$ (Fig. 20). In the HF approximation, only the one-electron emission transition $|1\sigma^{-1}2\pi^1\rangle \to E'$ is allowed, while the two-electron transitions $|1\sigma^{-1}2\pi^1\rangle \to E$ and $|1\sigma^{-1}2\pi^1\rangle \to G$ are forbidden. The admixture of the E' allowed state to the E and G states opens these forbidden RIXS channels. Calculations using the wave packet technique [Eqs. (26) and (46)] reproduce the experimental data (Fig. 21).

IX. VIBRATIONAL SCATTERING ANISOTROPY

In Sec. VII.A we discussed the Doppler splitting of the atomic peak in RAS, which shows abnormally strong sensitivity of the nuclear dynamics to the polarization of incoming radiation. The question arises: Does the form of the vibrational progression of RIXS and RAS depend on polarization? The first impression is that the answer is negative. Indeed, in the framework of the BO approximation the nuclear and electronic degrees of freedom are separated providing that the polarization dependence, which affects only the amplitudes of the electronic transitions, enters as just a prefactor for the vibrational part of the scattering amplitude [Eq. (21)] if the R dependence of these transition amplitudes is neglected. Apparently the polarization dependence of a vibrational progression appears when the BO approximation is violated and electronic states of different symmetries are mixed (see Sec. VIII.A), giving rise to the phenomenon of vibrational scattering anisotropy (VSA).

We consider two qualitatively different cases that demonstrate a strong dependence of the vibrational progression on polarization in the RIXS (Sun *et al.*, 2013) and RAS (Miron *et al.*, 2010) spectra.

A. Interference of resonant and Thomson inelastic scattering channels

In the soft x-ray range, Thomson scattering [Eq. (2)] is associated with an elastic peak ($\nu_f = 0$). For elastic scattering, the Thomson term, proportional to the number of electrons $\propto N$, far exceeds the contribution of resonance scattering (Pietzsch *et al.*, 2011). The first term in the expansion of the Thomson amplitude $[\exp(\imath\mathbf{q}\cdot\mathbf{r}) \approx 1 + \imath\mathbf{q}\cdot\mathbf{r})]$ opens an inelastic Thomson channel through a dipole transition, known in the hard x-ray region as Compton scattering (Hämäläinen and Manninen, 2001). Nevertheless, the amplitude of Thomson inelastic scattering or nonresonant inelastic x-ray scattering (NIXS), being N times smaller than the amplitude of elastic scattering, becomes comparable to the amplitude of the resonant term (2), thereby making the interference of these channels significant, as experimentally found in the RIXS from O_2 (Sun *et al.*, 2013). In this experiment, the incoming x-ray photon resonantly populated the dissociative intermediate state $X^3\Sigma_g^- \to {}^3\Sigma_u^-(1\sigma_g^{-1}3\sigma_u^1)$. Then, because of the electron-vibrational interaction, the molecule jumps to the bound state ${}^3\Sigma_u^-(1\sigma_u^{-1}3s_g^1)$, from which the radiative decay to the final state ${}^3\Sigma_g^-(3\sigma_g^{-1}3s_g^1)$ takes place. Besides the RIXS channel [Fig. 22(c)], the same final state can be populated by the direct dipole transition $X^3\Sigma_g^- \to {}^3\Sigma_g^-(3\sigma_g^{-1}3s_g^1)$ from the ground state

by the Thomson inelastic scattering channel. Taking into account different scattering anisotropy in NIXS ($\propto \sin^2\chi$) and RIXS ($\propto 1+\sin^2\chi$) [Fig. 22(a)] and different FC amplitudes of direct $\langle 0|\nu_f\rangle$ and resonant $\langle 0|\nu_i\rangle\langle\nu_i|\nu_f\rangle$ channels, it is possible to understand the dependence of the relative intensities of the vibrational resonances $\nu=0$ and $\nu=1$ on the scattering angle $\chi=\angle(\mathbf{k}',\mathbf{e})$ [Fig. 22(b)].

The contribution of Thomson scattering to the elastic peak was studied for acetone (Sun *et al.*, 2011) and oxygen molecule (Pietzsch *et al.*, 2011). Carniato *et al.* (2012) found interference of the elastic Thomson and resonance channels in Cl K-edge RIXS of the HCl molecule.

B. Interference of direct and resonant ionization scattering channels in RAS

We now consider the second mechanism of VSA, observed in RAS (Miron *et al.*, 2010) from the acetylene molecule C_2H_2 near the $1\sigma_u \rightarrow 1\pi_g$ absorption resonance. X-ray excitation of the intermediate state $1\sigma_u^{-1}1\pi_g^1$ is accompanied by the subsequent Auger decay to the final state $1\pi_u^{-1}\psi_{\mathbf{k}}^1$. The final electronic state can also be reached by the direct ionization of the valence electron $1\pi_u \rightarrow \psi_{\mathbf{k}}$. Different orientations of the dipole moments of the interfering resonant and direct ionization channels explain the difference in polarization dependence of these channels; see Eq. (4). In turn, different FC amplitudes of the direct and resonant channels (see Sec. IX.A) lead to a strong change of vibrational progression in RAS measured for the difference angle between the x-ray polarization vector and the photoelectron moment $\angle(\mathbf{e},\mathbf{k})=0°$ and 90°; see Fig. 23.

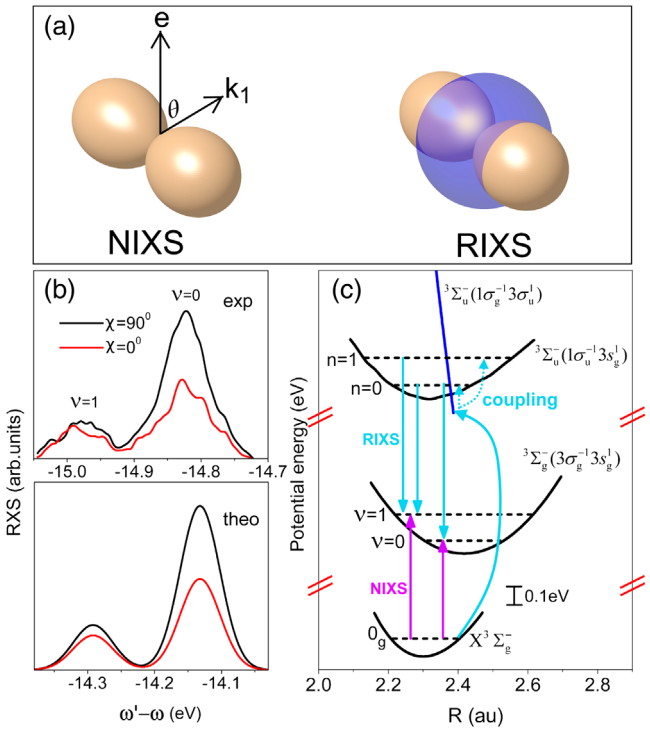

FIG. 22. The interference of the Thomson and resonance scattering channels in O_2 leads to a different polarization dependence of the vibrational resonances $\nu=0$ and $\nu=1$. Adapted from Sun *et al.*, 2013.

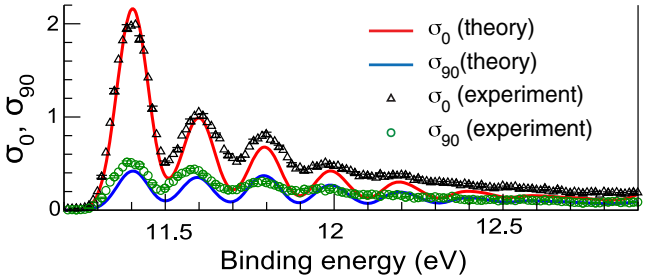

FIG. 23. The interference of the direct and resonant scattering channels leads to a different polarization dependence of the vibrational resonances (the VSA effect) in RAS from the acetylene molecule C_2H_2. Adapted from Miron *et al.*, 2010.

Difference in the anisotropy parameters for different final vibrational states was observed in RAS experiments with NO (Demekhin, Petrov, Sukhorukov *et al.*, 2010a, 2010b) and CO (Demekhin, Petrov, Tanaka *et al.*, 2010) molecules. This was quantitatively described while taking into account the LVI interference as well as the interference of the direct and resonant ionization channels. For N-K ionization of N_2O, another mechanism, caused by non-Frank-Condon transitions near shape resonances, is active for the polarization dependence of the vibrational progression (Lucchese *et al.*, 2007).

C. Recoil-induced inelastic Thomson scattering

In the hard x-ray region the recoil effect opens an inelastic channel in the Thomson scattering amplitude. As mentioned in Sec. IX.A, the momentum exchange between the hard x-ray photon and electrons results in the Compton scattering. The momentum exchange between photon and phonons results in a phonon band near the elastic peak. Thomson scattering $S(\mathbf{q},\omega-\omega')$ [Eq. (2)], playing a dominant role in the nonresonant scattering, is a powerful phonon research tool. In studies of cuprates (Blackburn *et al.*, 2013; Le Tacon *et al.*, 2014) it was possible to resolve low-energy phonons (Fig. 24) due to the ultrahigh spectral resolution (~1 meV) for x-ray photons with an energy of 23.7 keV. This enabled measurements of their temperature dependence in the dispersion in the temperature range $T=5$–150 K in the high-temperature superconductor $YBa_2Cu_3O_{6.6}$.

D. Recoil-induced Doppler splitting

The degree of manifestation of the recoil effect is determined by the momenta of the photon and photoelectron. In the soft x-ray range, the role of the photon momentum in the recoil is small. This explains why the recoil effect in this area is studied mainly by means of photoelectron spectroscopy. Significant attention in x-ray photoelectron spectroscopy is paid to the recoil-induced excitation of vibrations in free molecules (Domcke and Cederbaum, 1978; Felicíssimo, Guimarães, and Gel'mukhanov, 2005; Liu *et al.*, 2006; Gel'mukhanov *et al.*, 2007; Suga *et al.*, 2009; Kukk *et al.*, 2018; Liu, Vaz da Cruz *et al.*, 2019) and phonons in solids (Takata *et al.*, 2007, 2008) accompanied by a corresponding

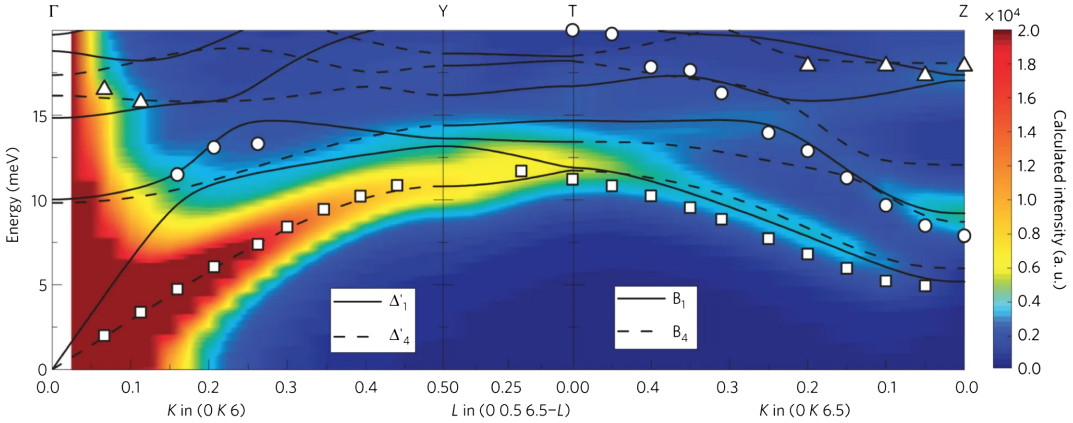

FIG. 24. Phonon dispersion along the lines of high symmetry of a superconductor $YBa_2Cu_3O_{6.6}$: Γ-Y, Y-T T-Z ($T \approx 300$ K). White symbols, momentum resolved RIXS experiment; color map and lines, density-functional theory (DFT) calculation. Adapted from Le Tacon *et al.*, 2014.

shift of the center of gravity of the photoelectron line. Calculations showed (Liu, Vaz da Cruz *et al.*, 2019) that the contributions of the photon and electron momenta are balanced in the hard x-ray range ($\omega \gtrsim 10$ keV). One of the most striking manifestations of the photonic recoil effect is the Compton effect (Kane, 1992; Hämäläinen and Manninen, 2001); see Sec. IX.A. We later discuss a recent development in studies devoted to the excitation of rotational degrees of freedom (Thomas *et al.*, 2009). To get a general idea of the role of the recoil effect in the motion of nuclei, we look at the photoelectron spectrum of the H_2 molecule in a wide energy range (Liu, Vaz da Cruz *et al.*, 2019). Figure 25 shows that the recoil effect leads not only to the excitation of vibrations but also to the dissociation of the molecule when the recoil energy exceeds the dissociation energy D_i.

X. RECOIL EFFECT: TRANSLATIONAL AND ROTATIONAL MOTION

Previously we showed that the momenta of photons and Auger electrons can lead to specific effects. Here we focus on the Auger process after photoionization by the initial photon. We investigate the role of recoil by the emitted photoelectron, which affects the initial state of the Auger decay.

A. Preparation of the initial state for Auger decay

Consider RIXS and RAS experiments with an intrinsic pump-probe character, where the incoming photon pumps the system and the emitted photon or Auger electron probes it.

If the photon energy is much larger than the $1s$ ionization potential I of the atom, a fast photoelectron with a momentum $\mathbf{p}_i$ is ejected. As a result of the recoil, the atom acquires momentum $\mathbf{p}_{\rm at} \approx -\mathbf{p}_i$, which far exceeds the thermal momentum $\bar{p}_{\rm at} = M\bar{v}_{\rm at} = \sqrt{2k_BT}$. The probability of $1s$ ionization

$$\sigma_{\rm ion} \propto |\mathbf{e}\cdot\mathbf{d}_{i0}|^2 \propto |\mathbf{e}\cdot\mathbf{p}_i|^2 \tag{47}$$

reaches the maximum for photoelectrons emitted along the polarization vector ($\mathbf{p}_i \| \mathbf{e}$) since the dipole moment of $1s$ ionization is parallel to the momentum: $\mathbf{d}_{i0} \| \mathbf{p}_i$. This means that, as a result of the recoil, there is a far from equilibrium distribution of atomic velocities (Gavrilyuk *et al.*, 2010) with two islands moving in opposite directions along $\mathbf{e}$; see Fig. 26(c).

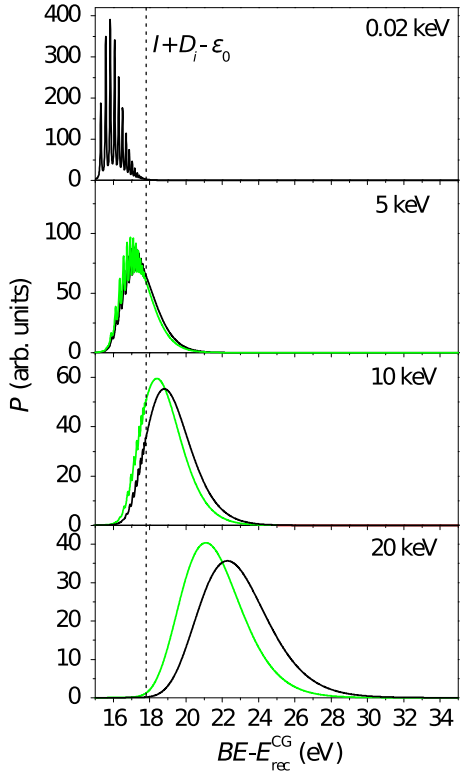

FIG. 25. Photoelectron spectrum of the H_2 molecule for $\omega = 0.02$, 5, 10, and 20 keV. Binding energy $BE = E - \omega$, $E^{\rm CG}_{\rm rec}$ is the recoil energy of the center of gravity. Green (gray) and black lines correspond to the angles between momenta of the photon and photoelectron: 90° and 145°, respectively. The vertical dashed line marks the dissociation threshold. Adapted from Liu, Vaz da Cruz *et al.*, 2019.

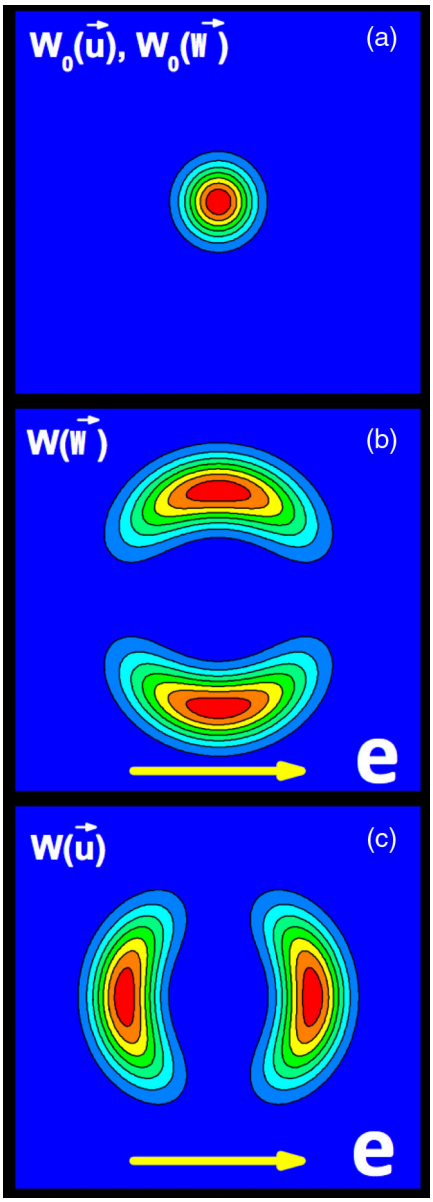

FIG. 26. (a) Initial Boltzmann distribution. Distributions over (b) angular velocities and (c) velocities induced by recoil from an ejected fast photoelectron. Adapted from Céolin *et al.*, 2019.

B. Experimental observation of recoil-induced nonequilibrium distribution over velocities

The created nonequilibrium distribution can be probed using the corresponding Doppler splitting (Gavrilyuk *et al.*, 2010) of the resonance of fluorescence or Auger resonance, as was done in the Auger experiment with Ne atoms (Simon *et al.*, 2014) (Fig. 27). In the latter case, the nonequilibrium distribution is probed by the Auger electron with the momentum $\mathbf{p}$, which has a certain orientation with respect to $\mathbf{e}$ in angular-resolved measurements. When the Auger electron is detected along the polarization vector $\mathbf{p}\|\mathbf{e}$, two islands in the velocity distribution [Fig. 26(c)] result in two peaks with opposing Doppler shifts $\mathcal{D} = \mathbf{p}_i \cdot \mathbf{k}/M \approx \pm p_i(\mathbf{e}\cdot\mathbf{p})/M = \pm p_i p/M$. Since the Doppler splitting $2\mathcal{D} \approx 2p_i p/M$ depends on the photoelectron momentum $p_i \propto \sqrt{\omega - I}$, the splitting increases with increasing ω, which is in agreement with the measurements (Fig. 27).

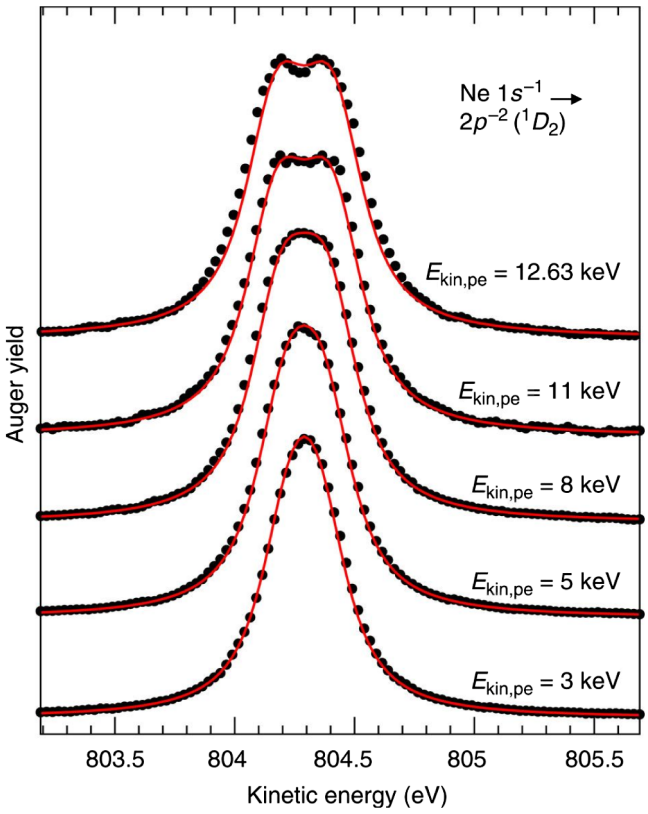

FIG. 27. Recoil-induced Doppler splitting of an Auger resonance in a Ne atom. From Simon *et al.*, 2014.

C. Dynamical rotational Doppler effect

The previously considered Doppler splitting should also be observed in molecules. But in molecules, in addition to the "translational" Doppler effect as predicted earlier there is also a rotational Doppler effect (Sun, Wang, and Gel'mukhanov, 2010). The reason for this effect is that, in the course of core ionization of the diatomic molecule AB, the photoelectron is ejected only from atom A where $1s$ is localized. Therefore, the recoil momentum $\mathbf{k}$ creates an angular momentum $\mathbf{j_p} = \eta[\mathbf{R}\times\mathbf{p}]$, where $\eta = M_B/M$ and $M = M_A + M_B$. Using the analogy between rotational and translational degrees of freedom, one can guess the expression for the rotational Doppler shift (Sun, Wang, and Gel'mukhanov, 2010) $\mathcal{D}_{\rm rot} = \mathbf{j_p}\cdot\mathbf{w}$, where $\mathbf{w}$ is the initial angular velocity of the molecule (for example, thermal velocity). The rotational Doppler shift leads to additional broadening of x-ray photoelectron resonances, which was experimentally verified for N_2 (Thomas *et al.*, 2011; Miao *et al.*, 2015) and HCl (Miron *et al.*, 2014).

We now consider an Auger experiment (Céolin *et al.*, 2019) on the CO molecule, in which photons with energy $\omega = 2.5$, 8, and 12 keV ionized the $1s$ electron of the carbon atom with the momentum $\mathbf{p}_i$. Because of the recoil, the molecule passed into a state of ultrafast rotation with an angular velocity $\mathbf{w} = \eta[\mathbf{R}\times\mathbf{p}_i]$. The created nonequilibrium distribution over angular velocities $w = |\mathbf{w}|$, as with translational velocities, depends on the polarization vector $\mathbf{e}$ and has two islands, as shown in Fig. 26(b). After a short time, the intermediate core-ionized state i decays into a final state, emitting an Auger

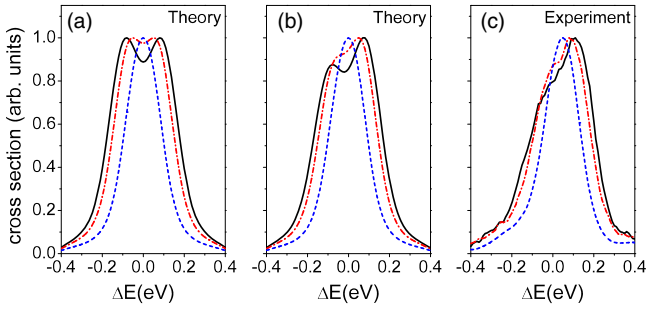

FIG. 28. The delay of Auger decay with respect to ionization leads to a change in the Doppler shift with time [Eq. (48)]. This makes the (a) Doppler doublet (b),(c) asymmetric. From Céolin *et al.*, 2019.

electron with a momentum $\mathbf{p}$ creating the angular momentum $\mathbf{j}_{\mathbf{p}}(t) = \eta[\mathbf{R}(t) \times \mathbf{p}]$. As with translational recoil-induced Doppler splitting, one can expect similar splitting for rotational degrees of freedom into a symmetric doublet. This is the case if we assume that ionization and Auger decay happen at the same instant; see Fig. 28(a). However, there is on average a time delay ($t \approx 1/\Gamma$) between the ionization act and the Auger decay. During this delay the molecule will reorient its molecular axis $\hat{\mathbf{R}} \to \hat{\mathbf{R}}(t)$, and thereby change the Dopper shift $\mathcal{D}_{\rm rot}(t)$:

$$\dot{\hat{\mathbf{R}}}(t) = [\mathbf{w} \times \hat{\mathbf{R}}(t)], \qquad \mathcal{D}_{\rm rot}(t) = \mathbf{j}_{\mathbf{p}}(t) \cdot \mathbf{w}. \tag{48}$$

This happens due to the large angular velocity w imparted to the molecule by the recoil. Here $\hat{\mathbf{R}}(t)$ is the unit vector along $\mathbf{R}(t)$ at the instant t. The rotation of the molecular axis during the Auger process makes the rotational Doppler double asymmetric [Fig. 28(b)], which is in full agreement with the experiment [Fig. 28(c)].

XI. RIXS OF LIQUIDS

Unlike the previously considered gaseous and crystalline media, a liquid is a more difficult object of study due to its inherent disorder and the fluctuations of the local structure. The absence of crystalline ordering makes the diffraction peaks in x-ray and neutron scattering weaker and more diffuse than Bragg peaks in crystals (Soper and Ricci, 2000; Fischer, Barnes, and Salmon, 2006; Sivia, 2011). For the same reason, theoretical modeling of fluids is much more complicated and less informative. For computational reasons it is also less accurate. Accordingly, more sophisticated methods of analysis of experimental data are required in order to extract useful quantitative information from them about the local structure and other properties. Therefore, the use of a set of complementary physical methods [diffraction, x-ray spectroscopy (XAS, RIXS, RAS, and XPS), NMR, Raman, IR, etc.] is necessary to obtain a consistent picture of the liquid. Taking into account the main direction of the review, we try to answer the following question: Which useful information can we extract from RIXS measurements on liquids and solutions? Owing to the fact that intermediate states in RIXS are created as a result of x-ray absorption, we highlight the role of XAS in the study of liquids. For the discussion to be substantive, we consider four different fluids: acetone, water, methanol, and acetic acid.

As previously demonstrated, RIXS is a proper tool for studying electron-nuclear dynamics since modern spectrometers can be used to acquire RIXS spectra of liquids with vibrational resolution.

However, previously at much lower resolution dynamical effects have also been identified by making a comparison between valence XPS and XES (Brena *et al.*, 2004), which share the same final valence-ionized states. Furthermore, isotope substitution has been widely employed to study dynamical effects in RIXS of hydrogen-bonded solutions and liquids (Odelius *et al.*, 2005; Fuchs *et al.*, 2008; Tokushima *et al.*, 2008; Lange *et al.*, 2011; Blum *et al.*, 2012; Lange and Aziz, 2013; Jeyachandran *et al.*, 2014). The phenomenon in which the introduction of ions into the water network reduces the dissociative character of the water molecules was observed in the spectator emission (Jeyachandran *et al.*, 2014; Yin *et al.*, 2015). In addition to a reduction of the dissociation, a direct influence of the ions on the electronic structure of the water molecules can be observed. The derived third spectral component (dR), associated with the water molecules that are influenced by the KCl ions, shows a spectral signature similar to the signature of intact water molecules. This again indicates that the salt ions cause a molecular reorganization of the water molecules around the ions. The recently achieved superhigh resolution in RIXS opens the way for more detailed studies.

Because of intrinsic fluctuating disorder in the liquid phase one cannot use the solid-state theoretical tools. Instead, the simulations of vibrationally resolved RIXS spectra of liquids have to be carried out employing a hybrid classical-quantum approach. First, the liquid is simulated using *ab initio* molecular dynamics of a N-molecule model in periodic boundary conditions. Second, transition dipole moments and cuts through the potential energy surfaces along vibrational modes are sampled from the molecular dynamics (MD) simulation. In a study of liquid water (Vaz da Cruz *et al.*, 2019a), the sampling was performed over molecules in a single configuration for comparison against earlier classical simulations of the core-hole dynamics (Odelius, 2009a, 2009b). These potential energy curves are used in quantum wave packet simulations of the partial RIXS cross sections $\sigma_k(\omega', \omega)$ for each kth molecule in the configuration. The total RIXS cross section is calculated as the sum over these partial contributions

$$\sigma(\omega', \omega) = \sum_{k=1}^{N} \sigma_k(\omega', \omega). \tag{49}$$

A. RIXS of liquid acetone: Mechanisms of line broadening

Acetone is a typical representative of aprotic polar liquids with a relatively weak dipole-dipole interaction that was studied both experimentally and theoretically by Sun *et al.* (2011). The role of the hydrogen bond, as we later see, is negligible for pure acetone liquid, since the C-H groups have limited hydrogen bonding capability. However, in mixed solutions of acetone with chloroform, the RIXS spectrum shows sensitivity to hydrogen bonding (Schreck *et al.*, 2016).

The acetone molecule $(CH_3)_2CO$ has 24 vibrational modes ($3N-6$ modes for $N=10$ atoms). Of these modes, as many as eight can be considered active in RIXS, and the most active modes are CO stretching, CO out-of-plane wagging, and CH_3 torsion modes (Sun *et al.*, 2011). Soft intermolecular modes where neglected in the analysis (Sun *et al.*, 2011).

The scheme of transitions and experimental RIXS spectra of liquid acetone for the $1s_O^{-1}\pi^{*1}$ core-excited state are shown in Fig. 29. The measurements displays a clearly resolved CO vibrational progression in quasielastic RIXS. However, the RIXS in the excited final state $f=n^{-1}\pi^*$ does not display vibrational structure. According to single-mode simulations of the free acetone molecule (Fig. 30) (Sun *et al.*, 2011) here should be resolved CO vibrations. This motivates us to look more carefully at the mechanism of line broadening.

First, we recognize the role of the environmental broadening given by the dipole-dipole interaction

$$\gamma_S \approx \tfrac{4}{3}\sqrt{\pi \ln 2}|\mu_S \Delta d_{f0}|\sqrt{\rho/a^3}, \tag{50}$$

where $\Delta d_{f0}=d_{ff}-d_{00}$, ρ is the concentration of the solvent molecules, and a is the radius of the solute (Weisskopf radius). This broadening is absent for quasielastic RIXS since $\Delta d_{f0}=0$. More advanced calculations of the environmental broadening based on the quantum mechanics–molecular mechanics method (Aidas *et al.*, 2011) coupled to the dynamical averaging scheme give the same broadening in neat acetone $\gamma_S^{\mathrm{MD}}(\mathrm{HWHM})\approx 0.04$ eV, which is not sufficient to wash out the vibrational structures in RIXS. However, the environmental broadening for aqueous acetone ($\gamma_S^{\mathrm{MD}}\approx 0.11$ eV; Fig. 31) is expected to play a more important role in spectral broadening due to the effect of the hydrogen bond between the "solute" acetone molecule and "solvent" water molecules.

However, to our surprise we discovered that the environmental inhomogeneous broadening is not the dominant source of the broadening in the lowest inelastic feature. Instead, in pure acetone the large broadening of the $n^{-1}\pi^*$ band is due to the low-frequency torsion modes, i.e., to the two CH_3 rotors and the C-O bending mode; see Figs. 30 and 31. During the short lifetime of core-excited state ($\omega_{\mathrm{tors}}/\Gamma\approx 0.14$) the methyl groups do not have time to rotate. Hence, the ground-state torsion wave packet is directly transferred to the final $n^{-1}\pi^*$ state. As a result, the soft torsion modes affect only the direct transition $0\to f$ characterized by the FC amplitude $\langle 0|\nu_f\rangle$. In this limit of fast scattering the dynamics of the soft modes in the intermediate state can be neglected. This is confirmed by the lack of soft mode broadening in the scattering to the ground electronic state. The prediction is that the broadening of the $n^{-1}\pi^*$ band will be observed also in RIXS of gas-phase acetone.

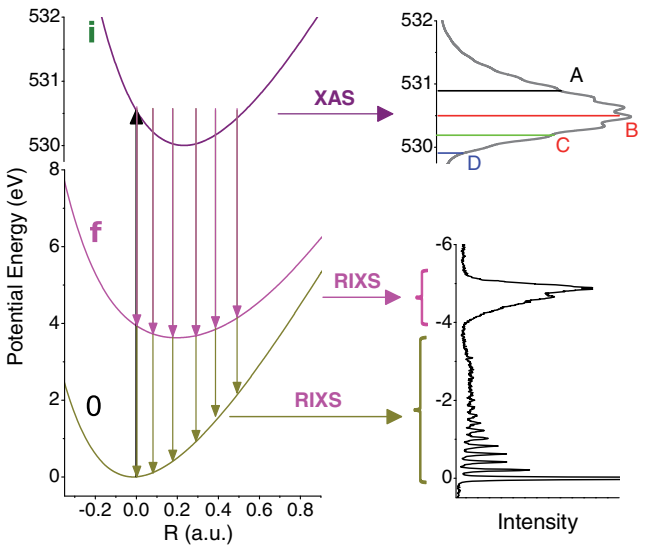

FIG. 29. Transition scheme and experimental RIXS spectrum of liquid acetone. $\omega=529.9$ (D), 530.2 (C), 530.5 (B), and 530.9 eV (A). Adapted from Sun *et al.*, 2011.

Thus, the total broadening of the profile is caused by following three different broadening mechanisms: (1) the width of incident light and instrumental broadening (≈0.025 eV), (2) environmental broadening (≈0.04 eV), and (3) multimode excitation including the CO out-of-plane wagging and torsion modes (≈0.075 eV). This together results in good agreement between the theory and the experiment (Fig. 32). One can also see the narrowing of the RIXS band as a function of detuning due to the shortening of the scattering duration.

B. Nuclear dynamics in RIXS of free water molecules

To understand the x-ray spectra of water in the liquid phase, it is instructive to shed light on RIXS of water in the gas phase. The water molecule has three vibrational modes: bending (b), symmetric (s), and antisymmetric (a) stretching modes. The vibrational energy levels up to the dissociation limit of the ground electronic state of free water molecules have been studied with one-photon (Carleer *et al.*, 1999; Naus *et al.*, 2001; Coheur *et al.*, 2002; Kassi *et al.*, 2005), two-photon (Grechko *et al.*, 2008), and three-photon (Grechko *et al.*, 2009) IR techniques and using high-level *ab initio* calculations (Barletta *et al.*, 2006; Császár *et al.*, 2010; Polyansky *et al.*, 2013) to interpret the measurements. It was established that the strongly coupled symmetric and antisymmetric stretching modes can be treated independently of the bending motion.

1. Quasielastic RIXS of free water molecules

The advantage of quasielastic RIXS is that it allows one to probe highly excited vibrational levels of the electronic ground state, with a selectivity arising from the shape of the potential energy surfaces of different core-excited states. The reason for this is that the nuclear wave packet can move far away from the equilibrium in the core-excited state. This is illustrated in Fig. 33, where the PESs of the ground and first three core-excited states are presented together with the simulated x-ray absorption spectrum in Fig. 33(a). In Fig. 33(b), we notice that the bending potential is merely softened in the $|1s_O^{-1}4a_1^1\rangle$ core-excited state relative to the ground state, whereas $|1s_O^{-1}2b_2^1\rangle$ and $|1s_O^{-1}2b_1^1\rangle$ exhibit an opening of the H-O-H angle. The $|1s_O^{-1}2b_1^1\rangle$ core-excited state is of Rydberg character and has a stretching potential with a shape similar to the ground state, as seen in Fig. 33(c). The

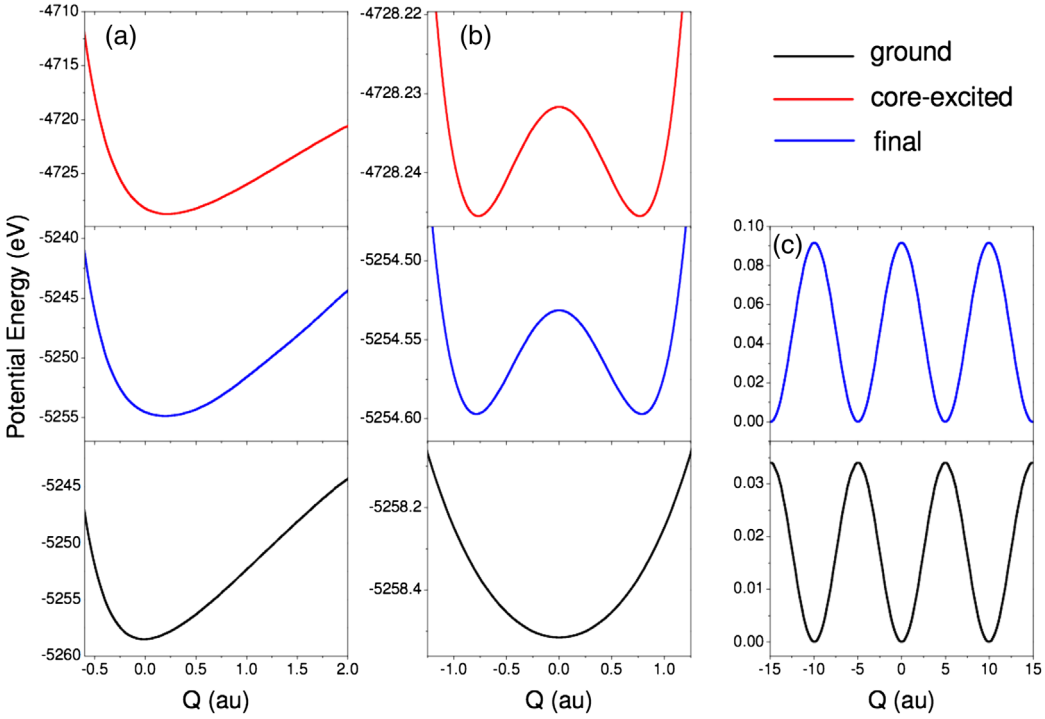

FIG. 30. The potential energy surfaces of the three most active modes of the acetone molecule. (a) CO stretching mode. (b) CO out-of-plane wagging mode. (c) CH_3 torsion mode. The ground (lower panels), core-excited (upper panels), and final (middle panels) state potentials are shown; in (b) and (c) potentials were extracted from experimental UV data (Baba, Hanazaki, and Nagashima, 1985).

$|1s_O^{-1}4a_1^1\rangle$PES is dissociative along the individual O–H bonds, whereas in the bound $|1s_O^{-1}2b_2^1\rangle$PES there is a valley along the symmetric normal coordinate. These qualitative differences of the PESs are crucial to understanding the RIXS, as it can probe the wave packet propagation in each of the core-excited states (Fig. 33).

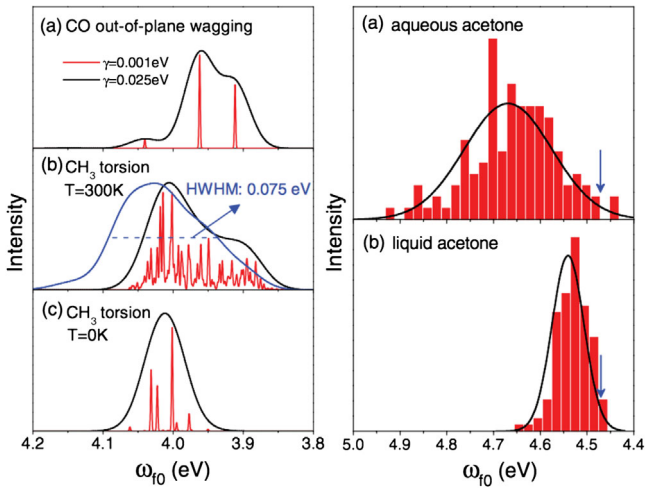

FIG. 31. The broadening mechanisms of $n^{-1}\pi^{*1}$ RIXS of the acetone spectrum. Left panel: spectra of the "direct transition" $0 \to f$ for (a) the CO out-of-plane wagging mode and the torsion mode at (b) $T = 300$ K and (c) $T = 0$ K. The blue (thick gray) line in (b) displays a spectrum taking into account both modes for $\gamma = 0.025$ eV. The spectra are computed using potential energy curves shown in Fig. 30. Right panel: distribution of transition energy ω_{f0} for (a) pure liquid acetone and (b) aqueous acetone from MD simulations. The blue arrow corresponds to the vertical transition energy for gas acetone. From Sun *et al.*, 2011.

Figure 34 shows how vibrational modes are excited differently depending on the intermediate states. One can see how the specific direction of the propagation of the wave packet in the dissociative $|1s_O^{-1}4a_1^1\rangle$ and bound $|1s_O^{-1}2b_2^1\rangle$ states determines the vibrational structure of the stretching overtones (ν_s, ν_a). This is observed in the experiment (Couto *et al.*, 2017) via slight shifts of the stretching vibrational peaks, although the actual fine structure is not resolved in the current experiment. As shown in Sec. VI.D, the state-specific high confinement of the nuclear wave packet in the core-excited state allows one to reconstruct from experimental spectra one-dimensional (1D) cuts of the ground-state potential energy surface in different directions.

2. Dynamical origin of the splitting lone-pair RIXS resonance in gas-phase water and methanol

As noted in Sec. VI.C, the potential surfaces of core-excited and final states are similar for decay transitions between core-hole states, e.g., K_α RIXS in the HCl or H_2S molecules. Here we show that this situation also happens in the soft x-ray region where the final state has the hole in the valence lone-pair orbital. We consider the RIXS channels that lead to the first valence-excited final state $1b_1^{-1}4a_1^1$ of the water molecule with a hole in the lone pair $1b_1$. This has been studied experimentally (Weinhardt *et al.*, 2012) and theoretically (Ertan *et al.*, 2018; Vaz da Cruz *et al.*, 2019a). As we later see, the gas-phase RIXS sheds light on the dynamical origin of the observed splitting of the lone-pair resonance in liquid water $(1b_1)$ (Fuchs *et al.*, 2008; Tokushima *et al.*, 2008;

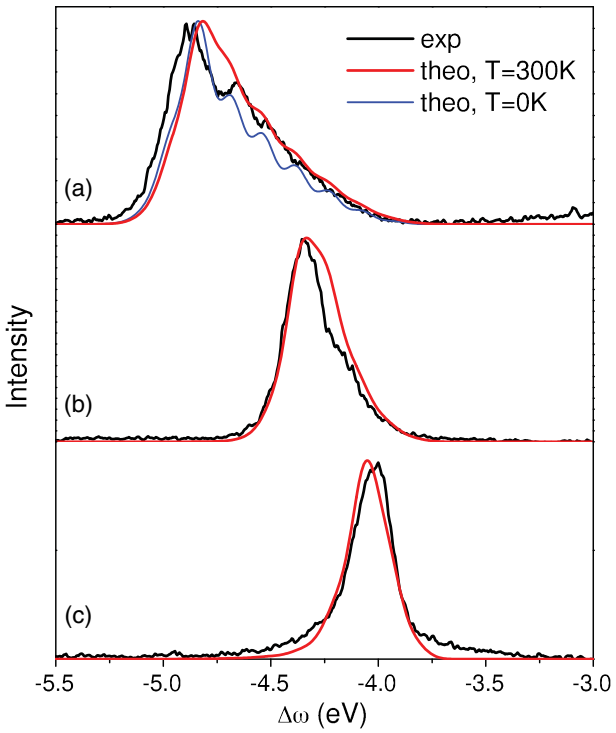

FIG. 32. The experimental and theoretical $n^{-1}\pi^{*1}$ RIXS profiles (Sun *et al.*, 2011) of liquid acetone for excitation frequencies from Fig. 29. $\gamma = 0.025$ eV. $\angle(\mathbf{k}', \mathbf{e}) = 90°$. $\Delta\omega = \omega' - \omega$. From Sun *et al.*, 2011.

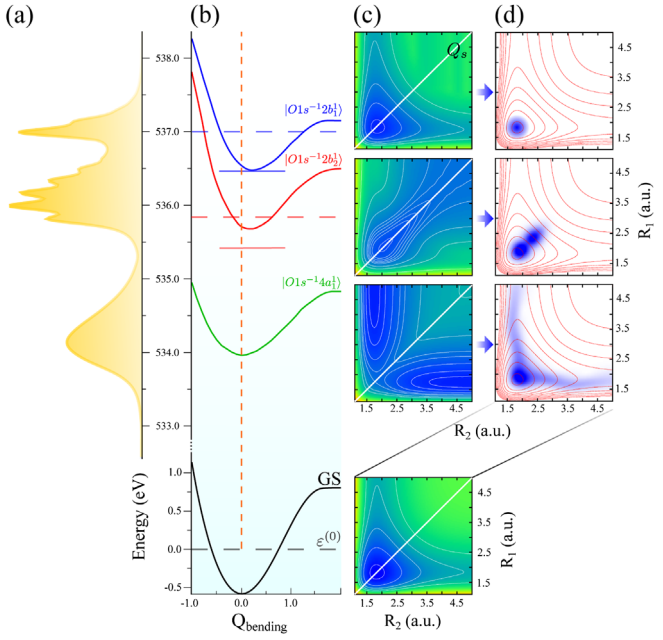

FIG. 33. X-ray absorption spectrum and potential energy surfaces of gas-phase water. (a) Simulated XAS spectrum for the three lowest core-excited states of water. (b) Potential energy curves (1D) of the bending vibrational mode for the ground states (GSs) and core-excited states. (c) Stretching potential energy surfaces (2D) as a function of bond lengths for the core-excited states. The color bars represent the energy range of the surfaces in eV relative to the bottom of the GS potential. Q_s is the symmetric stretching coordinate. (d) Squared integral wave packet $|\Psi|^2$ for each of the core-excited states for 2D stretching motion in 2D stretching potential energy surfaces of the ground electronic state. From Couto *et al.*, 2017.

Vaz da Cruz *et al.*, 2019a) and methanol ($2a''$) (Schreck *et al.*, 2014; Benkert *et al.*, 2016; Vaz da Cruz *et al.*, 2019b).

The similar nonbonding characters of $1s_0$ and lone-pair $1b_1$ orbitals already make the potential surfaces of the core-excited and final states almost parallel at moderate distortions; see Fig. 35(e). Decay transition at these distances have the same transition energy as the decay transition in the fragment of dissociation O*H in the region of dissociation. Note that, due to the small lifetime quenching of the wave packet for small propagation distances, the intensity of these transitions is significantly higher than intensity of the atomic peak. We name this transition "pseudoatomic" to distinguish it from the atomic transition that occurs in the region of dissociation, which is far away from equilibrium (Sec. VI.E).

Simulations shown in Fig. 35(c) explain the previously discussed splitting of the $1b_1$ peak in terms of molecular and pseudoatomic peaks. The dynamical origin of this splitting is confirmed by the observed dependence (Weinhardt *et al.*, 2012) of the $1b_1$ doublet on the isotope substitution. Theory nicely reproduces the isotope sensitivity (Ertan *et al.*, 2018; Vaz da Cruz *et al.*, 2019a).

A similar effect was also observed for free methanol molecules (Vaz da Cruz *et al.*, 2019b) for the $|2a''^{-1}8a'^{1}\rangle$ final state. Simulations (Vaz da Cruz *et al.*, 2019b) explain the dynamical origin of splitting of the lone-pair $2a''$ peak seen in the experiment through the sensitivity to isotope substitution (Fig. 36).

Exactly the same phenomenon should be present in the liquid phase because both molecular and pseudoatomic peaks are formed near the *equilibrium* distance, where the HB influence on the shape of the potentials is weak; see Sec. XI.C.

C. RIXS of liquid water and methanol

Water is a highly polar liquid with strong hydrogen bonds and a number of unusual thermodynamic properties (Palmer, Car, and Debenedetti, 2013; Millot *et al.*, 2018; Menshikov, Menshikov, and Fedichev, 2020). For example, unlike ordinary liquids its density decreases at low temperatures. The anomalous behavior of water's thermodynamic response functions begins near ambient conditions and can be significantly more pronounced in the supercooled state, when liquid water becomes metastable with respect to ice. To understand the thermodynamic behavior of supercooled water, the hypothesis of coexistence of low-density liquid (LDL) and high-density liquid (HDL) has been invoked (Röntgen, 1892; Caupin and Anisimov, 2019).

However, it remains an experimental challenge to reach the deeply supercooled region of water (so-called no-man's land) due to crystallization in the region of the expected liquid-liquid phase transition (Soper and Ricci, 2000; Palmer, Car, and Debenedetti, 2013), although liquid droplet (Kim *et al.*, 2017) and thin water film (Kringle *et al.*, 2020) experiments are used to delay crystallization. Recently this problem was

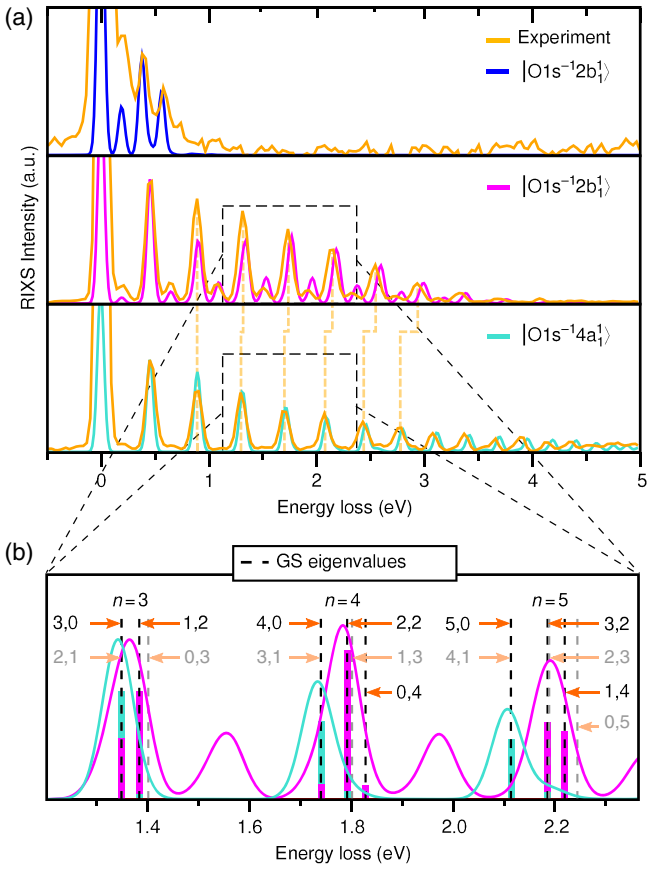

FIG. 34. (a) Quasielastic RIXS spectra for the $|1s_0^{-1}2b_1^1\rangle$, $|1s_0^{-1}2b_2^1\rangle$, and $|1s_0^{-1}4a_1^1\rangle$ core-excited states of a water molecule. (b) Fine structure of RIXS caused by overtones. Adapted from Couto *et al.*, 2017.

attacked by decompressing the high-density amorphous ice (Kim *et al.*, 2020).

1. RIXS versus x-ray and neutron scattering, IR, Rayleigh-Brillouin scattering, and XAS

The elemental sensitivity of x-ray diffraction is determined by the dynamical structure factor of this element $S(\mathbf{q},\omega) \propto Z$. Therefore, this method provides extremely limited information about hydrogen with $Z = 1$ (Fischer, Barnes, and Salmon, 2006). X-ray scattering, which is sensitive mainly to oxygen, measures the O-O radial distribution, providing information about the first three coordination spheres. From the measurement data, it is difficult to single out information about the O-O correlations of higher order. The situation with neutron scattering is similar, with the exception of hydrogen, because neutron scattering also gives the positions of the hydrogen atoms, particularly if hydrogen or deuterium isotope contrast is used (Fischer, Barnes, and Salmon, 2006). Both methods require theoretical modeling for an accurate and reliable interpretation. Usually, classical MD and Monte Carlo methods, possibly in combination with the Feynman quantum path integral method, are used. Modern x-ray and neutron experiments indicate that water is homogeneous under normal conditions (Soper and Ricci, 2000; Clark *et al.*, 2010; Soper, Teixeira, and Head-Gordon, 2010; Soper, 2019), in contrast to

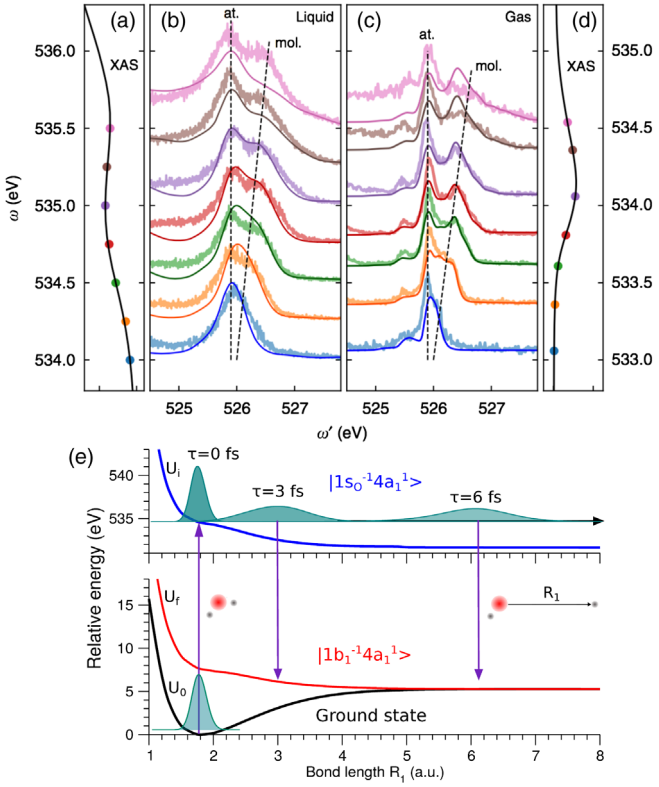

FIG. 35. Dynamical origin of the splitting of the $1b_1$ peak. (a), (d) Corresponding excitation energies in the XAS preedge region for liquid- and gas-phase water. Comparison of the dispersion of the split components in experimental RIXS spectra of (b) liquid- and (c) gas-phase water at the preedge region. Solid lines in (b) and (c) show theoretical spectra. Both (b) liquid- and (c) gas-phase spectra display a nondispersive component (pseudoatomic peak) and a molecular band following the Raman dispersion law. (e) Schematic illustration showing how the pseudoatomic peak is formed near equilibrium ($R = 3$ a.u.) as the PECs of the core-excited $[E_i(R)]$ and final $[E_f(R)]$ states become almost parallel: $\Delta U = E_i(R) - E_f(R) \approx$ const. The splitting between molecular and pseudoatomic peaks on top of the XAS resonance is approximately 0.45 eV. Adapted from Ertan *et al.*, 2018, and Vaz da Cruz *et al.*, 2019a.

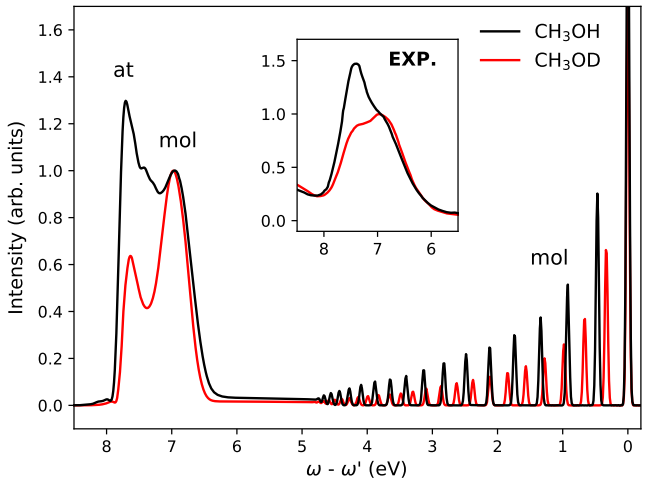

FIG. 36. Isotope effect for $2a''$ RIXS in gas-phase methanol: theory and experiment. From Vaz da Cruz *et al.*, 2019b.

the widespread hypothesis that HDL and high LDL fractions are present in water. These diffraction experiments have recently been strengthened in experiments on the Rayleigh-Brillouin scattering of optical radiation (532 nm) (Zykova *et al.*, 2017) over the range from 249 to 365 K. The theoretical modeling also supports the homogeneity of water under stationary conditions (English and Tse, 2011). HDL and LDL are expected to coexist during the phase transition of liquid to ice. There is an interesting approach (Russo and Tanaka, 2014; Shia, Russo, and Tanaka, 2018) that supports the two-state model. This theory is based on an order parameter that determines how close the nearest nonbonded molecule is to any given water molecule. However, the bimodal distribution obtained here is a consequence of the way in which the order parameter is defined rather than a representation of different populations of two states of water (Soper and Ricci, 2000). In spite of this remark, the search for the proper order parameter (Russo and Tanaka, 2014; Shia, Russo, and Tanaka, 2018) is crucial to understanding the possible liquid-liquid phase transition in water.

Note that one cannot infer that ambient water may be described as a mixture of two liquids (Röntgen, 1892), HDL and LDL (Wernet *et al.*, 2004; Nilsson and Pettersson, 2015), as stressed by recent reexamination of small-angle x-ray scattering (Soper and Ricci, 2000; Head-Gordon and Johnson, 2006; Clark *et al.*, 2010; Soper, Teixeira, and Head-Gordon, 2010; Soper, 2019), XAS (Chen, Wu, and Car, 2010; Kühne and Khaliullin, 2013; Sun *et al.*, 2017; Niskanen *et al.*, 2019), and MD studies (English and Tse, 2011; English, Kusalik, and Tse, 2013). However, there has been uninterrupted interest in supercooled water, named the no-man's land (Palmer *et al.*, 2018), where one can expect the coexistence of two phases. However, no definitive experimental proof exists to date (Amann-Winkel *et al.*, 2016). Because of this, simulations play an important role in this area. Whether two liquid phases have actually been identified in computer experiments (Smallenburg and Sciortino, 2015; Palmer *et al.*, 2018; Shi and Tanaka, 2020) or not (English and Tse, 2011; English, Kusalik, and Tse, 2013; Limmer and Chandler, 2013; Chandler, 2016) is currently being vigorously debated.

X-ray absorption spectra are used to probe properties of different liquids (Nagasaka, Yuzawa, and Kosugi, 2020), and especially the local structure of liquid water. Some time ago, an XAS study of liquid water (Wernet *et al.*, 2004; Nilsson and Pettersson, 2015) stirred controversy by concluding that a majority (>80%) of H bonds are broken in liquid water, which contrasts with the conventional near-tetrahedral picture supported by diffraction (Soper and Ricci, 2000; Head-Gordon and Johnson, 2006; Clark *et al.*, 2010; Soper, Teixeira, and Head-Gordon, 2010; Soper, 2019), x-ray photoelectron data (Nishizawa *et al.*, 2011), thermodynamic, and spectroscopic data (Stillinger, 1980). Moreover, later higher-level simulations, based on the Bethe-Salpeter equation (Chen, Wu, and Car, 2010; Sun *et al.*, 2017), do not support the main conclusion made by Wernet *et al.* (2004), which also is in contradiction to MD simulations of liquid water (Chen, Wu, and Car, 2010; Nilsson and Pettersson, 2011; Sun *et al.*, 2017); see also Kühne and Khaliullin (2013). Recently (Niskanen *et al.*, 2019) the areas of the preedge XAS peak (≈534–535 eV) of the gas phase, liquid water, and ice were used to attack this problem. This peak in the free water molecule corresponds to the core excitation of the dissociative $1s_0^{-1}4a_1^1$ state; see Fig. 33. A comparison of areas of the preedge peaks for gas, liquid, and ice was used to determine the average number of hydrogen bonds per molecule ($N = 3.48$) for liquid water under ambient conditions (Niskanen *et al.*, 2019). This value, which is significantly different than $N = 2.2$ (Wernet *et al.*, 2004), agrees with the x-ray and neutron scattering data (Soper and Ricci, 2000), as well as the MD simulations (Vaz da Cruz *et al.*, 2019a).

2. Dynamical origin of the lone-pair peak splitting in RIXS of liquid water and methanol

The local HB environment has also been probed in electronically inelastic processes (Fuchs *et al.*, 2008; Tokushima *et al.*, 2008; Odelius, 2009a, 2009b; Pietzsch *et al.*, 2015; Zhovtobriukh *et al.*, 2018): decay channels for RIXS and XES in which the $1s_0$ core hole is filled by a transition from the occupied lone-pair orbital $1b_1$. This transition forms a split peak [Fig. 35(b)] that in XES of liquid water has been attributed either to two distinct ground-state structural motifs (Tokushima *et al.*, 2008; Nilsson and Pettersson, 2015; Zhovtobriukh *et al.*, 2018) or to nuclear motion after core excitation (Fuchs *et al.*, 2008; Odelius, 2009a, 2009b; Pietzsch *et al.*, 2015; Ertan *et al.*, 2018; Niskanen *et al.*, 2019; Vaz da Cruz *et al.*, 2019a). The importance of improved spectral resolution in RIXS and XES to liquid measurement is striking in the gradually increased insight from early observations of dynamical effects in XES (Odelius *et al.*, 2005) and of the peak splitting in high-resolution RIXS and XES (Fuchs *et al.*, 2008), as well as direct evidence of proton dynamics in vibrationally resolved RIXS (Pietzsch *et al.*, 2015).

The experimental RIXS spectra shown in Fig. 35(b) display a striking quantitative coincidence of the ω dependence of the $1b_1$ splitting in the liquid and gas phases of water. This together with the isotope effect (Fuchs *et al.*, 2008) is an indication that the splitting in RIXS at the preedge resonance is of the same dynamical origin as for the gas phase (Ertan *et al.*, 2018) associated with the different dispersion laws of the pseudoatomic and molecular peaks; see Sec. XI.B.2. This conclusion is also supported by simulations (Ertan *et al.*, 2018; Vaz da Cruz *et al.*, 2019a). The main idea behind simulations is that the physical mechanism of the splitting for free water molecules is the same as for liquid water because the formation of the molecular and pseudoatomic peaks happens near equilibrium, where the role of the surrounding HB is weak; Sec. XI.B.2.

A similar splitting is also observed in RIXS for scattering in the main-edge and postedge regions and for nonresonant XES (Fuchs *et al.*, 2008; Tokushima *et al.*, 2008; Nilsson *et al.*, 2013; Yamazoe *et al.*, 2019). According to DFT-based MD simulations, the doublet in the region of the $1b_1$ peak for nonresonant excitations is related to atomic or pseudoatomic features arising from the $3a_1$ and $1b_1$ levels, which approach each other in the course of the O–H bond elongation in the core-ionized state, which as confirmed by the simulations (Odelius, 2009b) is dissociative in the local hydrogen bond

environment in liquid water. Notice that this splitting for higher excitation energies is absent in the gas phase (Weinhardt *et al.*, 2012), where (unlike in the liquid phase) the OH potential is bound (Odelius, 2009a). Since both molecular and pseudoatomic $1b_1$ peaks arise from decay near equilibrium, the splitting under excitation into the lowest core-excited state is not sensitive to differences in the HB environments (Vaz da Cruz *et al.*, 2019a). Hence, we conclude that the splitting cannot be regarded as a fingerprint of specific local structures. Notice that the lone-pair $2a''$ splitting observed for liquid methanol (Schreck *et al.*, 2014) can also be described in a dynamical context (Vaz da Cruz *et al.*, 2019b), but here there is an alternative interpretation of this splitting for liquid methanol based on the two structural motives (Ljungberg *et al.*, 2017).

3. Role of hydrogen bond on vibrations and fluctuations of OH potential energy curves: RIXS versus IR spectroscopy

The holy grail of the RIXS of liquids is to understand the competition roles of nuclear dynamics in the core-excited state and the strongly fluctuating surrounding HB. A step toward more detailed understanding can be taken by comparing the vibrational progression in quasielastic RIXS of a gas and a liquid (Fig. 37) under core excitation in the dissociative sate. Theoretically this was achieved by determining, based on configurations from a MD simulation, the stretching potentials (OH PECs) of water molecules in different environments in the liquid, which occasionally deviate strongly from the potential of the gas-phase molecule (Vaz da Cruz *et al.*, 2019a). The propagation of the nuclear wave packet results in the long vibrational progression seen in both theory and experiment. In the liquid, however, we observe a strong shortening of the vibrational progression relative to the gas phase [Figs. 37(a) and 37(b)]. This shortening arises from variations in the OH PECs, reflecting the different local HB environments [Fig. 37(c)] in liquid water. These variations mainly affect the long-range part of the OH PEC and result in a variation of the high vibrational levels, which is seen in the partial density of vibrational states of OH vibrations [Fig. 37(d)].

RIXS provides a vibrational probe complementary to IR spectroscopy. Therefore, it is pertinent to compare the RIXS and IR spectra of water (Fig. 38). Unlike in RIXS, the main contribution in IR absorption originates from the $0 \rightarrow 1$ dipole-allowed OH transition [higher lying dipole forbidden IR transitions are more than 2 orders of magnitude smaller (Bertie and Lan, 1996)]. Hence, the majority of IR studies of liquid water (Bakker and Skinner, 2010; Perakis *et al.*, 2016) have focused on this transition, which probes the bottom of the OH potential well. However, we notice that the liquid-gas shift in IR absorption ($\approx$280 cm^{-1}) is significantly larger than in RIXS ($\approx$140 cm^{-1}), and the RIXS and IR peaks are shifted in opposite directions with respect to the theoretically derived maximum of the OH vibrational density of states at $\approx$3490 cm^{-1} (Fig. 38).

To a large extent, the sensitivity of IR spectroscopy stems from the strong dependence of the IR intensity of the OH stretch on the hydrogen bond environment (Auer and Skinner, 2008; Yang and Skinner, 2010; Perakis *et al.*, 2016). The IR absorption transition dipoles of the OH stretching modes with a broken HB (located in the high-frequency region) are significantly smaller than those of hydrogen-bonded OH modes (located in the low-frequency region) (Yang and Skinner, 2010). The situation is reversed in RIXS, where the molecules with a weak or broken hydrogen bond are preferentially excited. This explains the opposite shifts of the RIXS and IR absorption resonances with respect to the maximum of the density of vibrational states; see the inset in Fig. 38. Thus, IR and RIXS spectroscopy complement each other and already deliver structural information at the lowest $0 \rightarrow 1$ transition: this OH transition in IR absorption predominantly shows the existence of structures with strong HB, contrary to the case of RIXS, where the peak position of the $0 \rightarrow 1$ transition is associated with both broken and strong HB structures (Vaz da Cruz *et al.*, 2019a). IR Raman spectra

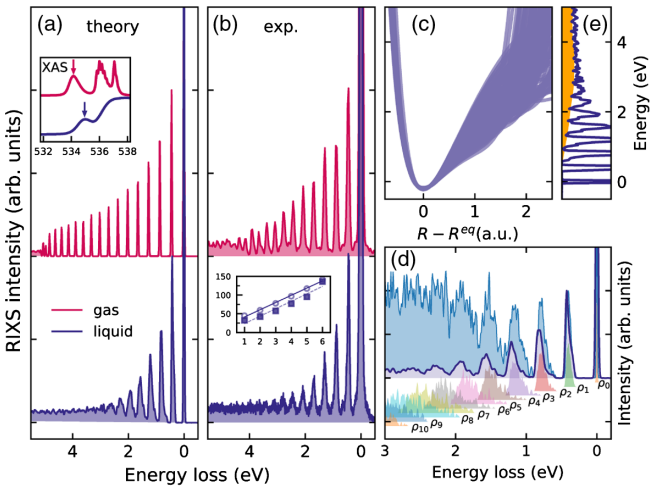

FIG. 37. Quasielastic RIXS of water in the gas and liquid phases under $4a_1$ preedge core excitation. Theory takes into account only OH vibrations. From Vaz da Cruz *et al.*, 2019a.

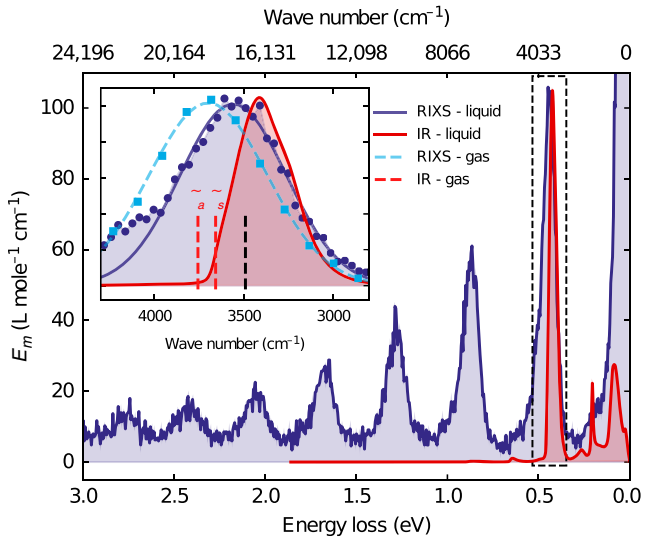

FIG. 38. Comparison of RIXS under preedge core excitations and IR spectra of water in the gas and liquid phases. From Vaz da Cruz *et al.*, 2019a.

(Auer and Skinner, 2008; Yang and Skinner, 2010; Perakis *et al.*, 2016) show a similar trend as the IR absorption spectra.

Because of long-range nuclear dynamic in the intermediate dissociative state, O–H bonds stretch into the long-range part of the potential energy curve, which makes the x-ray probe more sensitive than IR spectroscopy to the local environment. This makes the OH potential sensitive to the local surrounding and results in a broad distribution of the potentials [Fig. 37(c)]. One can exploit this property to effectively probe hydrogen bond strength via the distribution of intramolecular OH potentials derived from measurements (Vaz da Cruz *et al.*, 2019a). The role of soft vibrational modes (bending and intermolecular) was discussed by Pietzsch *et al.* (2015), Harada *et al.* (2017), and Vaz da Cruz *et al.* (2019a).

There is a nontrivial consequence of strong sensitivity of the OH potential to the local structure [Fig. 37(c). Namely, there is not necessarily (Vaz da Cruz *et al.*, 2019a) a strict one-to-one correspondence (Harada *et al.*, 2013) between the peak number in the RIXS spectrum and the actual quantum number of the vibrational state that contributes to it. The reason for this is random shifts of vibrational levels starting from $\nu = 3$ caused by the fluctuating HB network; see Fig. 3(e) of Vaz da Cruz *et al.* (2019a).

D. Anomalous role of the hydrogen bond on RIXS of liquid acetic acid

Carboxylic acids have attracted much experimental and theoretical interest over more than a century. The local structure of liquid acetic acid (ACA) is more complex and is still heavily debated; see Savchenko *et al.* (2021) and references therein. Recent RIXS measurements of liquid ACA and simulations (Savchenko *et al.*, 2021) show the absence of a vibrational progression of the OH stretch mode under preedge core excitation of hydroxyl oxygen unlike the cases of liquid water and methanol; see Fig. 39 and Sec. XI.C. This behavior was attributed to an unusually strong influence of HB, which changes the character of the intermediate state and quenches the vibrational progression in RIXS (Savchenko *et al.*, 2021). To understand this effect we look at two distinct

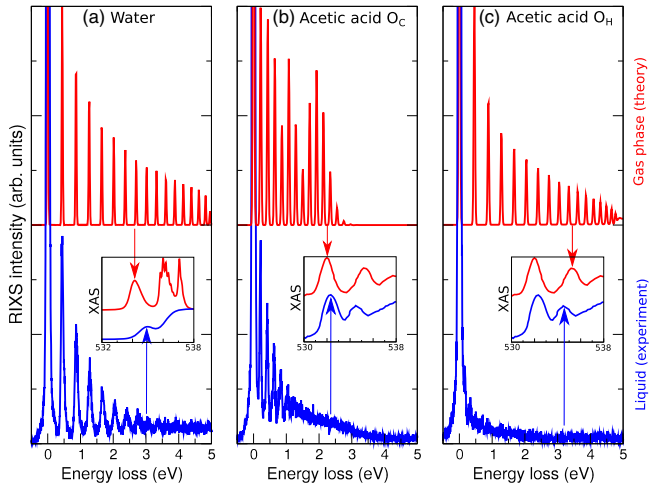

FIG. 39. Quasielastic RIXS of acetic acid and water. Top panels: gas phase. Bottom panels: liquid. From Savchenko *et al.*, 2021.

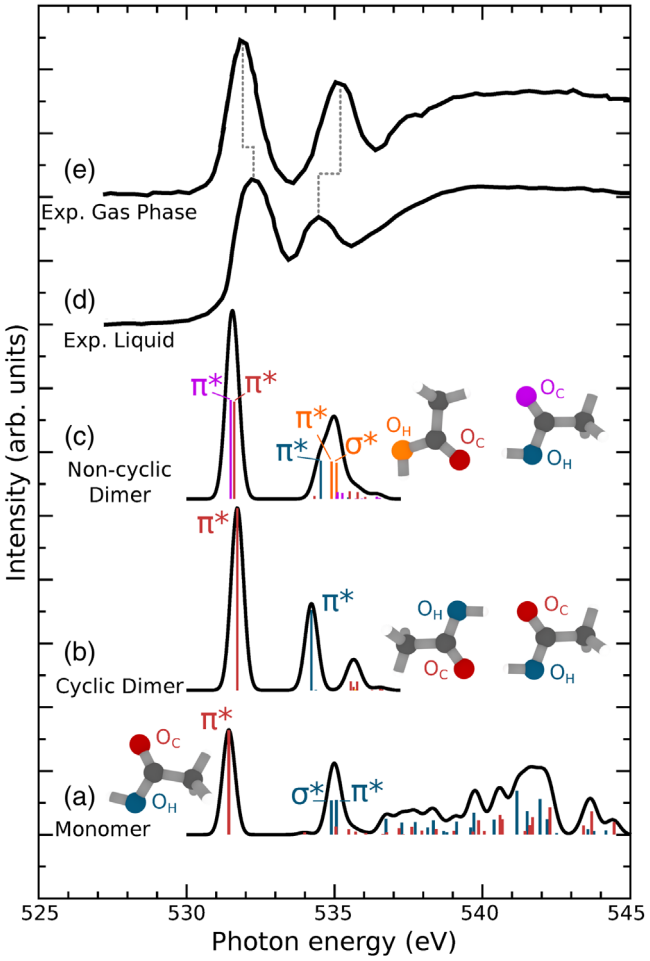

FIG. 40. Calculated XAS spectra of (a) the acetic acid monomer, (b) the regular dimer, and (c) the inverted dimer, showed in comparison to the measured XAS spectra of (d) acetic acid liquid given by Tokushima *et al.* (2009) and (e) the gas phase given by Robin *et al.* (1988). The calculated oscillator strengths are shown as bar graphs, where each bar is colored according to the atom of origin depicted in the molecular structure next to each spectrum. Adapted from Savchenko *et al.*, 2021.

dimers, namely, the regular dimer (a centrosymmetric cyclic dimer, which also exists in the gas phase) and the inverted dimer (an asymmetric noncyclic dimer, which is the shortest representative of the chain present in the liquid). Calculations show that only "in" OH groups are affected by HB: The $1s^{-1}_{O_H}\sigma^*$ dissociative core-excited state (which leads only to the long OH vibrational progression in RIXS) does not contribute at all in the 535 eV peak in the XAS (Fig. 40). This effect allows one to put an upper limit on the average concentration of "end" OH groups in the liquid ACA that are not strongly involved in HBs, implying that the average length of chains must be larger than 3 and/or there must be a significant abundance of cyclic structures (Savchenko *et al.*, 2021).

XII. RIXS IN STUDIES OF CORRELATED MATERIALS

The elementary excitations in solids (van den Brink, 2016) span a broad range of physical processes from charge-transfer (CT) excitations at 4–10 eV, metal centered *d-d* excitations

$\lesssim$4 eV, and magnons ($\lesssim$0.5 eV) down to phonons ($\sim$10–50 meV) at the meV scale; see also Fig. 24 and Schlappa *et al.* (2018). Since the x-ray photon transfers significant momentum to the material, RIXS can measure the momentum transfer [Eq. (17)] dependence or dispersion of the excitation energy of these modes (Ament *et al.*, 2011; Schlappa *et al.*, 2012; Le Tacon *et al.*, 2014; Comin and Damascelli, 2016; Dean *et al.*, 2016; Hariki, Wang *et al.*, 2020); see Sec. V.B and Fig. 24. As with free molecules (Sec. IV), the polarization of x rays gives rise to new opportunities for RIXS experiments on solids. A polarization analysis of the spectral features allows one to gain information on the symmetry of the excitations and therefore on their nature (Murakami *et al.*, 1998; Braicovich *et al.*, 2014; Hunault *et al.*, 2018).

Spin waves (spinons), also referred to as magnon quasiparticles, are energetically low-lying excitations of the spin lattice in crystalline materials (Faddeev and Takhtajan, 1981; Haldane, 1981; Khaliullin and Oudovenko, 1997; Doniach and Sondheimer, 1998; Kitaev, 2006). Special attention was paid to 1D (Haldane, 1981; Voit, 1995; Giamarchi, 2004; Giamarchi, 2016) and 2D (Kitaev, 2006; Hermanns, Kimchi, and Knolle, 2018) spin liquids due to unusual physical properties and because these systems can be described by strictly solvable models.

Systems with strongly correlated electrons, in particular, transition-metal (TM) compounds, present an interesting class of materials with extremely rich properties (Kugel' and Khomskii, 1982; Ishihara, 2017; Ishii, 2017; Streltsov and Khomskii, 2017). Among them are metals, insulators of a special kind, and systems with metal-insulator transitions; they exhibit different types of ordering [magnetic ordering, charge ordering, and orbital ordering (OO)], the cooperative Jahn-Teller (JT) effect, and high-temperature superconductivity. This richness is due mainly to strong electron correlations and the many degrees of freedom involved in mutual interplay: charge, spin, and orbital, all of this on the background of the lattice, with which all of these electronic degrees of freedom often strongly interact.

Spin-resolved valence band excitations were also studied using magnetic circular dichroism and magnetic linear dichroism (Luo *et al.*, 1997; Yablonskikh *et al.*, 2001; Miyawaki *et al.*, 2017; Zimmermann *et al.*, 2018; Elnaggar *et al.*, 2020) in RIXS with an external magnetic field for magnetization of the sample (Magnuson *et al.*, 2006; Elnaggar *et al.*, 2019; Umetsu *et al.*, 2019).

A. Charge transfer

CT excitation TM compounds lead to final states in which electrons are transferred between the ligand band and the 3*d* orbitals at the TM site. In particular, ligand-to-metal CT (LMCT) is frequently detected in RIXS. These excitations are typically at higher energies than the *d-d* excitations (as shown in Fig. 41) and are also inherently broader since they involve transitions having the broad ligand band.

In the RIXS and RAS studies (Woicik *et al.*, 2018, 2020) of CT excitations in solids, one uses the polarization, momentum, and excitation energy dependence of the spectra. The stage of this direction of investigation prior to 2010 was

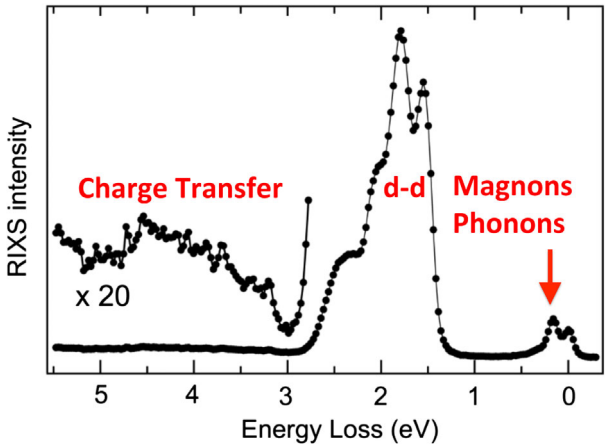

FIG. 41. The typical energy scale of elementary excitations in solids is exemplified for the RIXS spectrum at the Cu L_3 edge of the cuprate antiferromagnet $Ba_2Cu_3O_4Cl_2$; see also Rossi *et al.* (2019a). The elastic peak is at energy loss $\omega - \omega' = 0$. From Fatale *et al.*, 2017.

previously reviewed (Rueff and Shukla, 2010; Ament *et al.*, 2011). Here we stress only the main physical processes involved.

Charge transport in solids is determined by the energetics of moving electrons from one site to another. The process in TM compounds is defined by competition between the energy of charge transfer $\Delta_{CT} = E(d^{n+1}L^{-1}) - E(d^n)$ and the *d-d* Coulomb interaction $(U = E(d^{n-1}) - E(d^n) - [E(d^n) - E(d^{n+1})])$, the latter of which is associated with moving a *d* electron from one metal site to another. Here L^{-1} denotes a hole on the ligand site. This nontrivial problem was solved by Zaanen, Sawatzky, and Allen (1985) strictly in the framework of the single-ion Anderson model (SIAM). The SIAM approach, invented by Anderson (1961), has been extended to an interpretation of core-level spectra (Gunnarsson and Schönhammer, 1983).

For the case of a Mott-Hubbard (MH) insulator $\Delta_{CT} > U$, the top of the valence band is composed primarily of 3*d* states, and the band gap is of a *d-d* type (U). For the case of a CT insulator where $U > \Delta_{CT}$, the U is large enough to push the occupied 3*d* states deep into the VB, meaning that the top of the valence band is primarily of ligand 2*p* character; see Fig. 42. Transition-metal oxides, including cuprates, nickelates, and manganites, are the CT insulators with the lowest optical CT excitations across the optical gap. According to the nonresonant x-ray emission experiment (Olalde-Velasco *et al.*, 2011) (Fig. 43), almost all MF_2 difluorides are MH insulators, which is in agreement with the Zaanen-Sawatzky analysis (Zaanen and Sawatzky, 1990). Figure 43 shows a MH-to-CT insulator transition between CoO and NiO, leaving CuO as an obvious CT insulator.

One can identify two approaches used in simulations of RIXS: the cluster method and the more accurate SIAM approach.

A widely used and computationally efficient cluster method is the semiempirical ligand-field multiplet model. In this atomic model (de Groot *et al.*, 1990), which takes into account SO interactions, electron correlation is accounted for

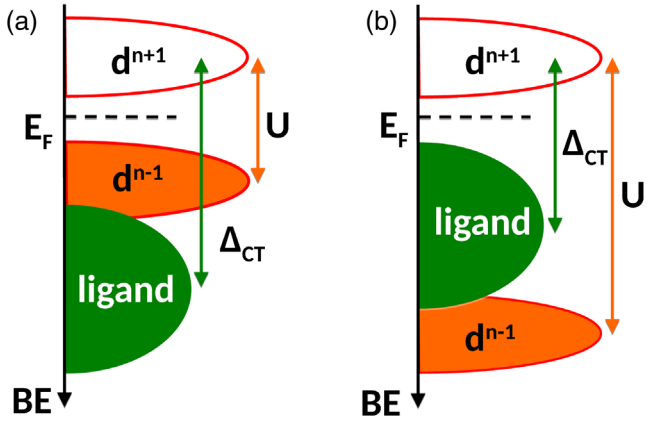

FIG. 42. Sketch of the Zaanen-Sawatzky-Allen (Zaanen, Sawatzky, and Allen, 1985) classification of transition-metal compounds into (a) a *d-d* character Mott-Hubbard insulator and (b) a character charge-transfer insulator. Filled areas show the occupied *d* states of metal and ligand states, while hollow areas depict electron affinity states d^{n+1}. Δ_{CT} is the charge-transfer energy, while *U* is the Coulomb repulsion energy of *D* electrons at the same site. Adapted from Chainani *et al.*, 2013.

by a full configuration interaction (CI) including the 3*d* orbitals and by reducing the Hartree-Fock electron-electron repulsion integrals. Ligands are described by an empirical ligand-field splitting of the 3*d* orbitals. For highly covalent complexes, the effects of CT excitations are modeled using additional configurations, where one electron has been transferred from or to the ligand. Adding these configurations to the CI gives the semiempirical charge-transfer multiplet model (Tanaka and Jo, 1994; de Groot, 2005; de Groot and Kotani, 2008). There are also *ab initio* cluster methods (Josefsson *et al.*, 2012; Pinjari *et al.*, 2014; Kunnus *et al.*, 2016b), which offer better predictive power than semiempirical methods, at least in principle. In the *ab initio* model, the basis for the CI calculations are MOs calculated for small clusters, typically the central atom and first-shell ligands. An alternative strong

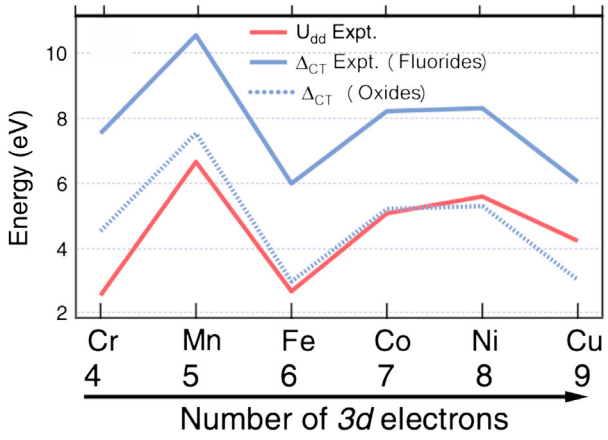

FIG. 43. Experimental picture of the MH-to-CT transition for 3*d*-TM difluorides (MF_2) and oxides (MO_2). *M* = Cr or Zn. The values for Δ_{CT} were decreased by 3 eV for oxides to compensate for the difference in electronegativity between F and O. Adapted from Olalde-Velasco *et al.*, 2011.

approach to model x-ray spectra in the condensed phase was developed on the basis of localized Wannier orbitals from periodic DFT calculations (Haverkort, Zwierzycki, and Andersen, 2012). Thereby a multiconfigurational treatment can be obtained that takes the crystal environment into account.

The cluster method well describes the *d-d* excitation in RIXS ($\omega - \omega' \lesssim 4$ eV) but not in the CT band ($\omega - \omega' \sim 4$–10 eV), which is too localized and strong. The main shortcoming of the cluster model is that it takes into account hybridization only with the nearest neighbors, leading to CT configurations centered at a single energy Δ_{CT}. However, in real solids the ligand 2*p* electrons form a wide band. To properly understand and describe the CT excitations, it was recognized that taking into account only the ligand band structure leads to the wide band of CT excitations seen in the experiment (Fig. 41). Such an extension of the cluster approach leads to the SIAM with full multiplet effects, which is widely used in modern semiempirical simulations of RIXS (Magnuson, Butorin, Agui, and Nordgren, 2002; Magnuson, Butorin, Guo, and Nordgren, 2002; Ghiringhelli *et al.*, 2005, 2006; Chiuzbăian *et al.*, 2008) of the RIXS. The combination of the local density approximation to the density-functional theory and the dynamical mean-field theory (Hariki, Winder *et al.*, 2020) eliminates most of the empirical parameters of the traditional cluster method.

The RIXS together with XAS is used to get information about the valence and conductivity bands, the parameter of the SIAM model, and the band gap of materials. Applications of band gap engineering are extensive in materials science and are found in fields such as optoelectronics, water-splitting photocatalysts, and solar cells. For example, an ideal photocatalyst should have a band gap of around 2 eV. However, the native band gap of promising materials, such as different forms of TiO_2, are in the range of 3.0–3.2 eV. Thus, one needs to reduce the band gap of TiO_2 and other potential materials such as ZnO, In_2O_3, and GaN to a desired region of 2 eV by insertion of other transition metals into semiconductors and insulators. For example, a band reduction from 8 eV (pure TiO_2) to 4.1 eV was found for SiO_2:TiO_2 mixtures (Green *et al.*, 2013), and a band reduction from 3.4 eV was found for pure ZnO down to 2.9 eV in $Zn_{1-x}NiO$ (Das *et al.*, 2013).

The NIXS governed by the Thomson term F_f^T [see Eq. (2)] gives in crystals a unique opportunity for imaging of core orbitals to probe the orbital anisotropy in solids without the necessity of any modeling (Yavaş *et al.*, 2019).

Wang *et al.* (2017) studied high-resolution 2*p*3*d* RIXS of CoF_2, $CoCl_2$, $CoBr_2$, and CoS compounds. The improved spectral resolution allowed them to analyze *d-d* and CT excitations in more detail. Systematical analysis allowed for an accurate determination of the charge-transfer parameters of the LMCT model.

XIII. RESONANT ELASTIC X-RAY SCATTERING IN SOLIDS: ORBITAL AND CHARGE ORDERING

The elastic resonant x-ray scattering (anomalous x-ray scattering) deserves special attention because of the enhancement of the cross section near the XAS resonance, but mainly due to the qualitatively different polarization dependence of

the resonant term in the KH amplitude [Eq. (2)] at resonance (Ishihara, 2017), $\propto(\mathbf{e}'\cdot\mathbf{d}_{0i})(\mathbf{e}\cdot\mathbf{d}_{i0})$, to a magnitude comparable with the nonresonant Thomson contribution, $\propto(\mathbf{e}'\cdot\mathbf{e})$.

A. Hard x-ray region: Orbital ordering versus Jahn-Teller distortion

A while ago pioneering RIXS experiments (Murakami *et al.*, 1998; Murakami, Kawada *et al.*, 1998) demonstrated the possibility of using this effect to shed light on properties of perovskite-type manganites $La_{0.5}Sr_{1.5}MnO_4$ and $LaMnO_3$. Depending on the composition, manganites show a variety of magnetic and electric phenomena, including ferromagnetic, antiferromagnetic, charge, and orbital ordering, leading to high-temperature superconductivity and colossal magnetoresistance (Salamon and Jaime, 2001). These highly correlated systems, where charge, spin, and lattice degrees of freedom are intimately interrelated (see Fig. 44), deserve a microscopic examination of their properties.

Contrary to nonresonant Thomson scattering, the polarization of x rays is rotated in the resonant scattering $\mathbf{e}^{\sigma}\to\mathbf{e}^{\pi'}$ due to the crystal-field anisotropy in the $4p$ shell, in which the components are split into Δ components. Here $\mathbf{e}^{\sigma}$ and $\mathbf{e}^{\pi}$ denote the polarizations parallel and perpendicular to the scattering plane, respectively.

For the usual Thomson reflection, the intensity is independent of the azimuthal angle, but a resonant reflection shows a characteristic oscillation (Fig. 45) (Murakami *et al.*, 1998; Murakami, Kawada *et al.*, 1998)

$$\sigma^{\mathrm{res}}_{\sigma\pi'}\propto\frac{\Delta^2\sin^2\psi}{[(\Omega-2\Delta)^2+\Gamma^2][(\Omega+\Delta)^2+\Gamma^2]}. \tag{51}$$

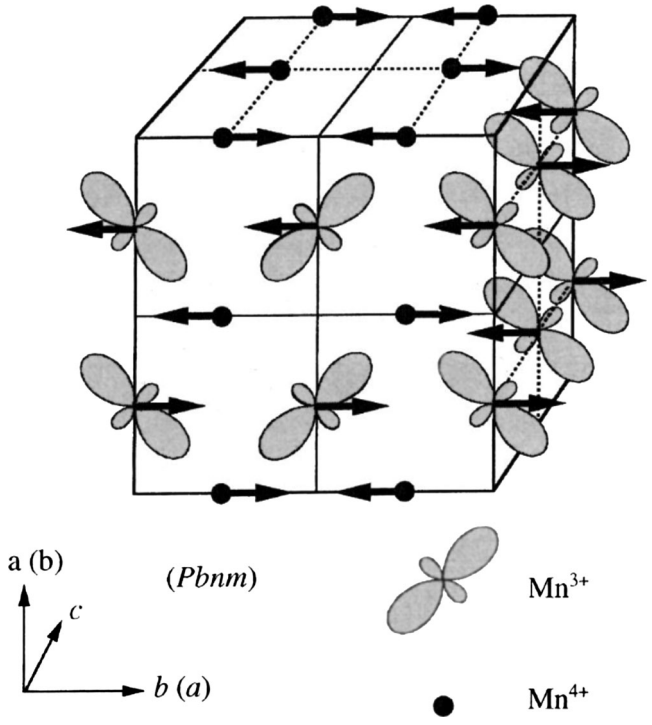

FIG. 44. Spin, charge, and orbital ordering pattern of the charge-exchange antiferromagnetic type. From Salamon and Jaime, 2001.

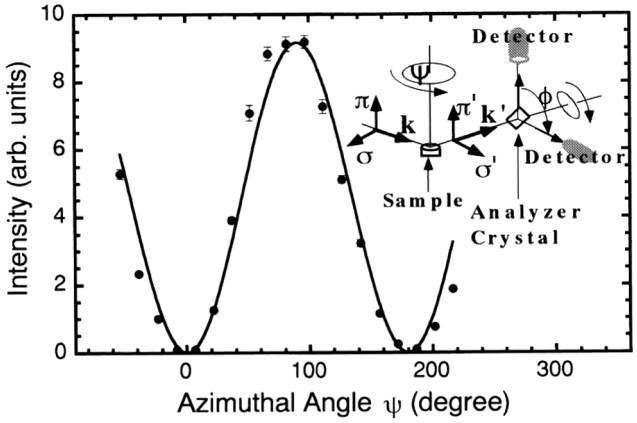

FIG. 45. Azimuthal-angle dependence of the intensity of the orbital ordering reflections $(3,0,0)$. From Murakami *et al.*, 1998.

The azimuthal angle ψ is zero when the crystal stacking vector (c axis) is normal to the scattering plane, and $\psi=90°$ when it is in the scattering plane; see Fig. 44 and Murakami *et al.* (1998). The resonant $1s\to4p$ dipole-allowed transitions at the Mn K edge correspond to core excitations to the $4p$ band, which is split by Δ both due to the Coulomb interaction with the polarized $3d$ band (related to OO) and because of JT distortion (Fabrizio, Altarelli, and Benfatto, 1998; Murakami *et al.*, 1998):

$$\Delta=\Delta_{\mathrm{OO}}+\Delta_{\mathrm{JT}}. \tag{52}$$

The signs of the splitting are opposing for these mechanisms (Murakami *et al.*, 2007), which were studied for different compounds both theoretically (Fabrizio, Altarelli, and Benfatto, 1998; Elfimov, Anisimov, and Sawatzky, 1999; Mizokawa, Khomskii, and Sawatzky, 1999) and experimentally (Iga *et al.*, 2004; Murakami *et al.*, 2007).

The experiment (Fig. 46) shows that the orbital ordering persists until $T_O=780$ K, while magnetic order occurs at or below T_O (Turner *et al.*, 2008). This transition is accompanied by a dramatic increase in the intensity observed at the fundamental reflection $(2,0,0)$, which was interpreted (Murakami *et al.*, 1998) in terms of an orthorhombic-to-orthorhombic structural phase transition. This transition in $LaMnO_3$ was studied earlier (Wold and Arnott, 1959; Jonker, 1966).

Later a similar technique was applied to the study of charge and orbital order in doped manganites (Zimmermann *et al.*, 1999) $Pr_{1-x}Ca_xMnO_3$, with $x=0.4$ and 0.5. Orbital and charge order below $T_O\approx245$ K enhances the antiferromagnetic correlations, and thereby promotes the magnetic phase transition. It was found that the $(0,1,0)$ magnetic phase charge order reflection for $x=0.5$ shows only a slight broadening corresponding to a correlation length of ≥2000 Å. While, the $(0,2.5,0)$ orbital-order reflection is substantially broadened, with a correlation length of ≈160 Å (Fig. 47). Below the first-order-like phase transition at T_O the charge and orbital-order parameters exhibit identical temperature dependencies.

The resonant enhancement of coherent x-ray scattering allowed researchers to study the slow (few minute) orbital

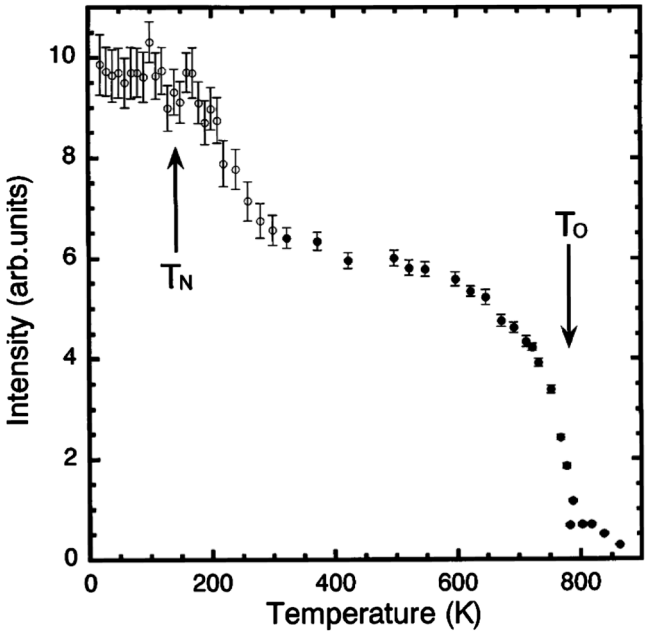

FIG. 46. Temperature dependence of the normalized intensity of the orbital ordering reflection $(3, 0, 0)$ at $\omega = 6.555$ keV. Empty symbols correspond to results obtained at an azimuthal angle $\psi = 127°$ and cooling with a Displex cryostat; filled symbols were obtained for $\psi = 90°$ by heating with an oven. The two datasets were scaled to be equal at $T = 300$ K. From Murakami *et al.*, 1998.

domain dynamics in a half-doped manganite near the orbital-order phase transition temperature (Turner *et al.*, 2008).

B. Charge-density waves in the cuprates

We now turn to the discussion of resonant x-ray scattering studies of charge order, or equivalently a charge-density wave (CDW), which competes and coexists with superconductivity in underdoped cuprates. Bednorz and Müller (1986) found a new family of high-temperature superconducting materials, cuprate superconductors, made of layers of copper oxides (CuO_2) alternating with layers of other metal oxides, which act as charge reservoirs. The electrons within a CDW form a periodic pattern incompatible with the periodicity of the underlying lattice. Referring readers interested in a detailed description to the review by Comin and Damascelli (2016), we outline some key achievements in this field later.

Both resonant (Achkar *et al.*, 2012; Ghiringhelli *et al.*, 2012; Blanco-Canosa *et al.*, 2013; Thampy *et al.*, 2013; Le Tacon *et al.*, 2014; Comin *et al.*, 2015) and nonresonant (Chang *et al.*, 2012; Blackburn *et al.*, 2013) x-ray scattering experiments demonstrated CDW order with domain sizes of up to 20 unit cells. CDW has emerged as a universal feature of hole-doped cuprates. Resonant soft x-ray scattering (RSXS) measurements of the electron-doped cuprate $Nd_{2-x}Ce_xCuO_4$ also indicate CDW formation in electron-doped cuprates (da Silva Neto *et al.*, 2015).

The electron-phonon interaction is a major factor influencing the competition between collective instabilities in correlated-electron materials. The role of phonons (Fig. 24) in a narrow range of momentum space around the CDW ordering vector and the interference of dynamical CDW excitations with the lattice were studied in $YBa_2Cu_3O_{6.6}$ (Le Tacon *et al.*, 2014), $Bi_2Sr_2LaCuO_{6+\delta}$, and $Bi_2Sr_2CaCu_2O_{8+\delta}$ superconductors (Chaix *et al.*, 2017; Li *et al.*, 2020).

High-brightness x-ray sources opened a new frontier in the context of high-magnetic-field studies (Comin and Damascelli, 2016). Femtosecond XFEL pulses synchronized with the high-magnetic-field (32.1 T) pulses were used to explore the magnetic field–induced 3D CDW correlations in high quality ortho-II and ortho-VII $YBa_2Cu_3O_x$ (YBCO) crystals by RSXS measurements at the Cu L_3 edge (Jang *et al.*, 2016).

C. RIXS from low-dimensional systems

The lowering of the real or effective dimensionality of the systems brings unusual physical properties. A two-dimensional electronic gas can be formed at the interface between appropriate materials. A typical example of 2D materials is graphene. Nanowires are representative of 1D fermions. Often a real 3D system exhibits strong 1D properties due to effective lowering of the dimensionality along a certain orientation of the orbitals in the solids (for example, *d* orbitals). There are many families of organic and inorganic quasi-1D materials that deviate strikingly from 3D Fermi liquid behavior in their normal state and undergo a variety of low-temperature phase transitions into, e.g., charge-density or spin-density wave insulating phases or even become superconducting (Jérome and Schulz, 1982; Dressel, 2018). The excitations in the 1D electron gas are approximate bosons, rather than fermions, and bear resemblance to the Tomonaga-Luttinger liquid model (Tomonaga, 1950; Luttinger, 1963), which was solved exactly by Mattis and Lieb (1965). Efetov and Larkin (1976) and Haldane (1981) gave Luttinger liquid theory the form it has today.

Although the state of an electron is characterized by spin, charge, and orbital degrees of freedom, the electronic excitations break up into deconfined spinons, holons, and orbitons in 1D systems. This effect is one of the most unusual manifestations of collective low-energy quantum physics of interacting particles in low-dimensional systems.

Spin-charge separation in 1D.—In 1D electron systems, theory predicts that collective excitations of electrons produce, instead of the quasiparticles in ordinary Fermi liquids, two new particles known as "spinons" and "holons." Unlike ordinary quasiparticles, these particles do not carry the spin and charge information of electrons together. Instead, they carry spin and charge information separately and independently. Unlike spinons, which have spin $1/2$ but no charge, holons carry zero spin and charge e. The spinon and holon are decoupled and propagate with different velocities. This novel and exotic phenomenon was predicted theoretically (Lieb and Wu, 1968; Haldane, 1981) and is commonly known as spin-charge separation. The spin-charge separation, and thus spinons and holons, was observed in the 1D copper oxide chain compound $SrCuO_2$ using angle-resolved photoemission spectroscopy (Kim *et al.*, 1996, 1997, 2006). The interpretation of the experiment is supported by the observed distinct dispersions of spinon and holon and quantitative agreement with the theory.

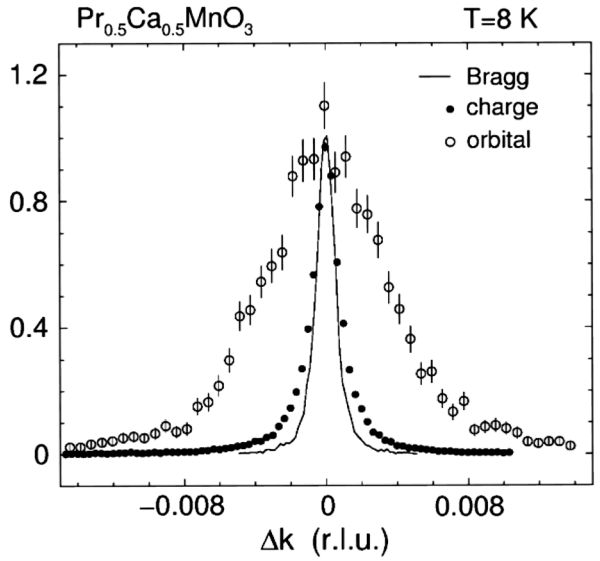

FIG. 47. Longitudinal scans of the $(0, 2, 0)$ Bragg reflection, the $(0, 1, 0)$ charge order peak, and the $(0, 2.5, 0)$ orbital-order peak. The orbital-order peak is significantly broadened. From Zimmermann *et al.*, 1999.

Spin-orbiton separation in 1D.—In addition to spin, the orbital degrees of freedom play an important role in the low-energy physics of various correlated TM compounds. In MH insulators, the Kugel'-Khomskii model (Kugel' and Khomskii, 1982; Streltsov and Khomskii, 2017) is the effective low-energy superexchange model for coupled spin and orbital excitations. Jackeli and Khaliullin (2009) recognized that SO coupling in crystals results in an exchange interaction that depends on the spatial orientation of a given bond ij. Instead of the Heisenberg interaction $H = J\sum_{ij}\mathbf{S}_i\cdot\mathbf{S}_j$, the interaction of pseudospins is described by the Kugel'-Khomskii-Kitaev Hamiltonian (Kugel' and Khomskii, 1982; Kitaev, 2006; Streltsov and Khomskii, 2017)

$$H = \sum_{\langle ij\rangle} K^{\gamma} S_i^{\gamma} S_j^{\gamma}, \tag{53}$$

which entangles in general the orbital and spin degrees of freedom. In the exactly solvable and experimentally relevant Kitaev honeycomb model (Kitaev, 2006; Hermanns, Kimchi, and Knolle, 2018), the spin degrees of freedom interact via a strongly anisotropic nearest-neighbor Ising exchange, where the easy axis $\gamma = x, y, z$ depends on the bond direction $\langle ij\rangle$ (Fig. 48).

However, the orbital and spin degrees of freedom are decoupled in the 1D systems in the peculiar regime where spinons are propagating faster than orbitons. The spin-orbital (spinon and orbiton) separation is conceptually analogous to the spin-charge separation in the 1D system and was predicted by Wohlfeld *et al.* (2011) and Chen *et al.* (2015). The spin-orbiton separation was observed using RIXS (Schlappa *et al.*, 2012; Bisogni *et al.*, 2015); see Fig. 49.

The electronic quasiparticle is unstable in 1D systems and the elementary excitations in the low-energy region are the spinon, the holon, and the orbiton, propagating with different

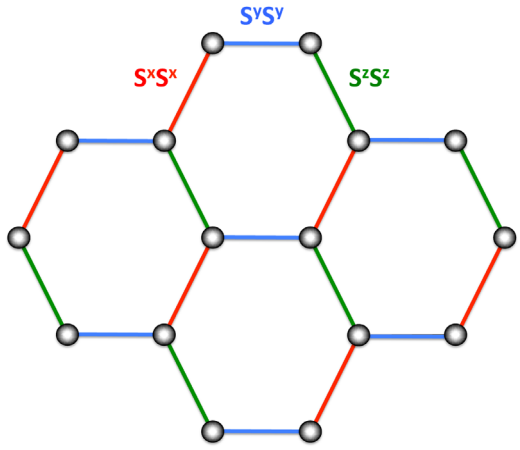

FIG. 48. Kitaev interactions on a honeycomb lattice indicating the three kinds of bonds (x, y, and z) and spins sitting on the vertices of a lattice.

velocities. However, real materials are never strictly 1D. In spite of this, RIXS measurements of the anisotropic ladder system $CaCu_2O_3$ combined with simulations (Bisogni *et al.*, 2015) show that spin-orbital separation occurs along the leg direction x through the x-z orbital channel as in a 1D system, while no fractionalization is observed for the x-y orbital, which extends in both the leg (x) and rung (y) directions, unlike in a 1D system. Therefore, the $3d_{xy}$ orbital excitation is affected by interladder couplings, and hence behaves as in a

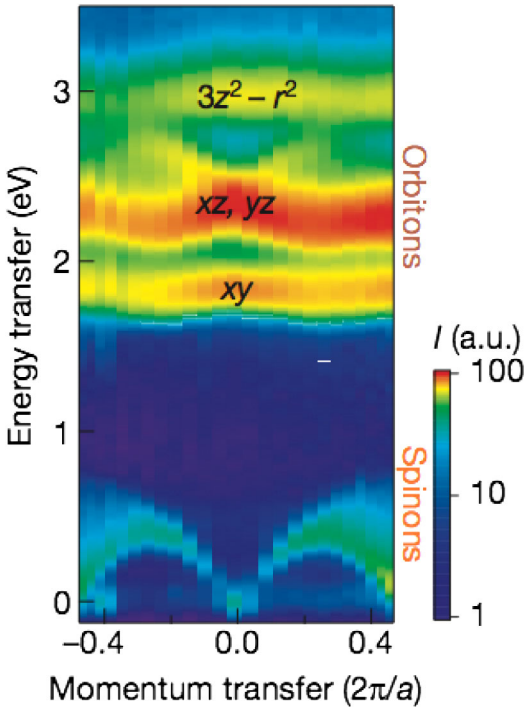

FIG. 49. Measured spin-orbital separation process in an antiferromagnetic spin chain, emerging after exciting a ground-state copper $3d_{x^2-y^2}$ orbital to an excited copper $3d_{xy}$ or $3d_{xz}$ orbital. RIXS intensity map of the dispersing spin and orbital excitations in quasi-one-dimensional Mott insulator Sr_2CuO_3 as functions of photon momentum transfer along the chains and photon energy transfer. Adapted from Schlappa *et al.*, 2012.

2D system. This means that various orbital symmetries allows one to select different degrees of dimensionality in the same system. Moreover, Bisogni *et al.* (2015) showed that spin-orbital separation is, in general, much more robust than spin-charge separation.

D. Dynamics of multispinon excitation in RIXS

RIXS is an adequate and unique tool to study magnetic excitations (Ishii, 2017) and provides access to nonlocal spin correlation functions, as recently demonstrated in an experiment (Schlappa *et al.*, 2018). The theoretical details of spinon excitation in RIXS were given by Ament *et al.* (2009, 2011), Haverkort (2010), and Kumar *et al.* (2018). To explain the magnetic spin-flip transitions one needs the combination of core and valence SO coupling, crystal-field splitting, and core-valence and valence-valence electron-electron interactions (Das *et al.*, 2018; Elnaggar *et al.*, 2019; Nag *et al.*, 2020). Double spin-flip RIXS [Fig. 50(a)] across two Cu sites at the oxygen K edge along Cu-O-Cu chains in the quasi-1D spin-chain cuprate Sr_2CuO_3 allows one to probe two- and four-spinon continuum excitations [Fig. 50(b)] (Schlappa *et al.*, 2018). The spin dynamics in the intermediate state (see the upper panel of Fig. 50) is defined by the competition between the spin hopping rate (inverse exchange constant J) and the lifetime $1/\Gamma$ of the core-excited state. Simulations (Schlappa *et al.*, 2018) show the decrease of intensity of magnetic excitations in O-K RIXS upon decreasing the core-hole lifetime. Moreover, the four-spinon excitations decrease faster than the two-spinon ones. One can expect direct time-resolved XFEL studies to facilitate the study of such a spin dynamics at the femtosecond timescale.

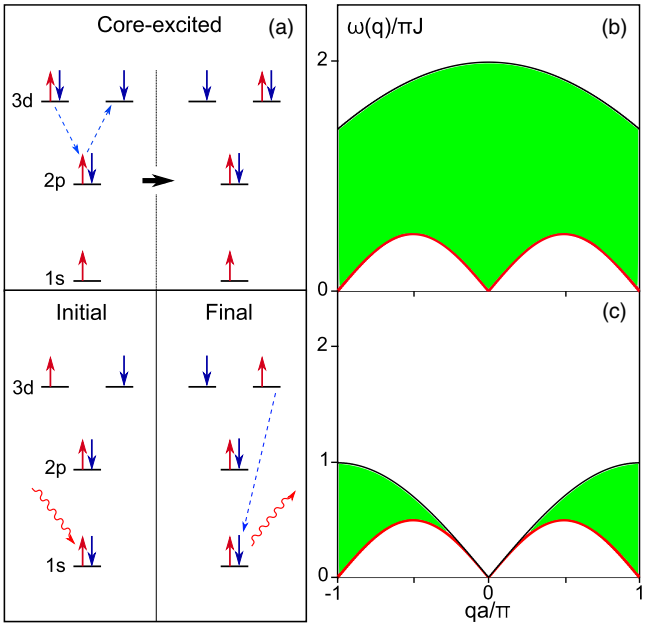

FIG. 50. (a) Sketch of double spin-flip RIXS process in a Cu-O-Cu chain. (b) Two- $[\omega_{2s}(q)]$ and four- $[\omega_{4s}(q)]$ spinon continua: $(1/2)|\sin(qa)| \le \omega_{2s}(q)/\pi J \le \sin(qa/2)$, $(1/2)|\sin(qa)| \le \omega_{4s}(q)/\pi J \le \sqrt{2[1+\cos(qa/2)]}$ (Caux and Hagemans, 2006). The dispersion law of the single spinon $\omega_{1s}(q) = (1/2)|\sin(qa)|$ is depicted by the red line.

XIV. NONLINEAR PHENOMENA IN STRONG FIELD OF XFEL PULSES

A. Stimulated RIXS, four-wave mixing, pulse compression, superfluorescence, and suppression of the Auger decay channel

We previously highlighted the current state of RIXS and RAS studies based on long-pulse synchrotron x-ray sources. For more than a decade new XFEL and HHG sources (Johnson *et al.*, 2018; Duris *et al.*, 2020) of short (down to attoseconds), coherent, and intense (up to gigawatt) x-ray pulses have been operating, making it possible to investigate ultrafast electronic and nuclear dynamics as well as high-energy-density systems (Humphries *et al.*, 2020). Intense XFEL radiation allows one to study such nonlinear RIXS-related processes (Kowalewski *et al.*, 2017; Young *et al.*, 2018; Rossbach, Schneider, and Wurth, 2019) as stimulated RIXS (Sun, Liu, and Gel'mukhanov, 2009a, 2009b; Sun, Liu *et al.*, 2010; Beye, Schreck *et al.*, 2013; Kimberg and Rohringer, 2013, 2016; Weninger *et al.*, 2013; Kimberg *et al.*, 2016) and x-ray lasing (Miao *et al.*, 2012; Rohringer *et al.*, 2012), two-photon RIXS (Sun, Rinkevicius *et al.*, 2010; Hopersky, Nadolinsky, and Novikov, 2018), x-ray pulse compression (Sun, Liu, and Gel'mukhanov, 2009a, 2009b; Sun, Liu *et al.*, 2010; Kumar *et al.*, 2020; Li, Labeye *et al.*, 2020), four-wave mixing (Tanaka and Mukamel, 2002; Mukamel, 2005; Sun, Liu, and Gel'mukhanov, 2009a, 2009b; Sun, Liu *et al.*, 2010; Bencivenga *et al.*, 2015), and nonlinear wave mixing of x-ray and near-infrared beams (Glover *et al.*, 2012). Special attention was paid to the competition between stimulated x-ray emission and Auger decay (Rohringer and Santra, 2008; Liu *et al.*, 2010; Sun *et al.*, 2018).

Soft x-ray lasing was first observed in neon vapor (Rohringer *et al.*, 2012) at the Stanford Linac Coherent Light Source (LCLS) and later extended to the hard x-ray range by lasing in a Cu foil with 20 mm thickness (Yoneda *et al.*, 2015), performed at SPring-8 Angstrom Compact Free-Electron Laser (SACLA) facility. The first demonstration of stimulated RIXS (SRIXS) was performed by resonant excitation of a dense neon gas target with femtosecond, high-intensity x-ray pulses from the LCLS; see Fig. 51. Compared to the spontaneous RIXS process, signal enhancement of 7–9 orders of magnitude was achieved. Later stimulated x-ray emission was observed in $5M$ solution of $MnCl_2$ complex (Kroll *et al.*, 2018) (Fig. 52). That the stimulated x-ray emission regime was reached was proven by the observation of exponential growth of the number of photons with an increase of the pump pulse energy and by the narrowing of the line shape of the SRIXS (Kroll *et al.*, 2018). Seeded amplified $K\beta$ x-ray emission with a signal enhancement of more than 10^5 was recently observed in a $NaMnO_4$ solution using two colors of XFEL pulses (Kroll *et al.*, 2020).

Recently an unusual manifestation of the recoil effect in SRIXS was observed, namely, the recoil-less stimulated RIXS (Eichmann *et al.*, 2020). The random distribution of momenta of spontaneously emitted photons gives a broad velocity

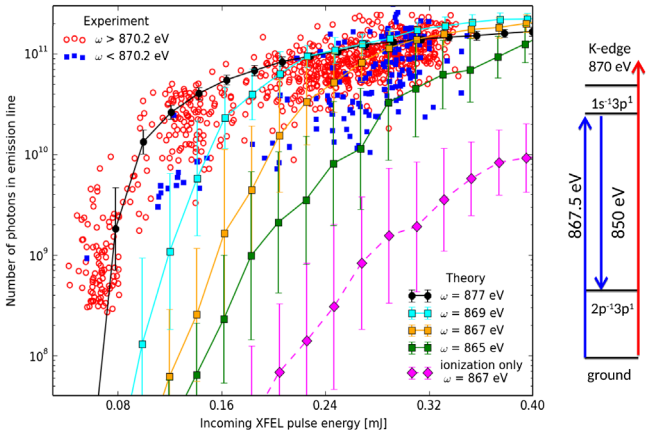

FIG. 51. Pump energy dependence of the SRIXS signal from Ne: measured number of photons in the emission line as a function of the incoming pulse energy for $\omega > 870$ eV (average $\bar{\omega} = 876$ eV) and $\omega < 870$ eV (average $\bar{\omega} = 868$ eV) along with the theoretical results. Adapted from Weninger *et al.*, 2013, and Weninger and Rohringer, 2013.

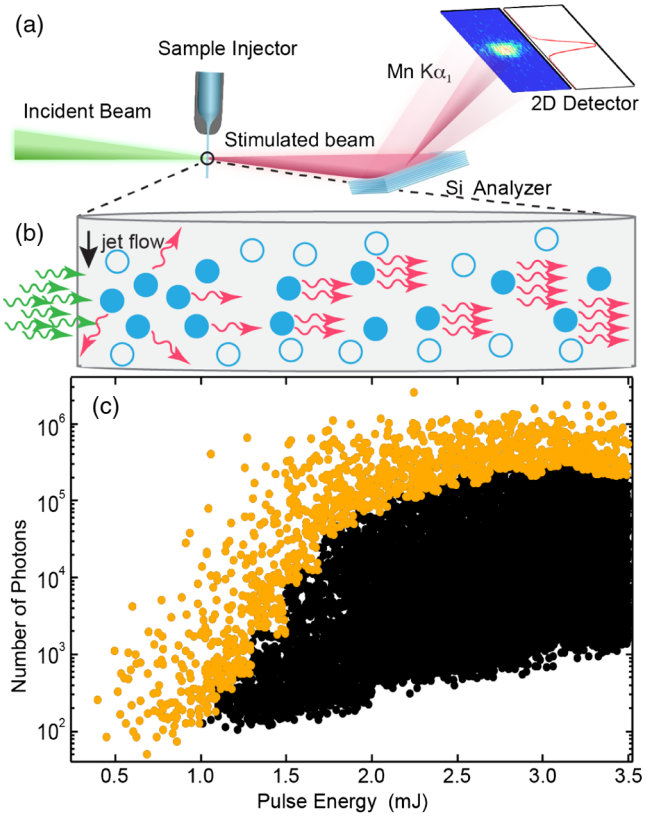

FIG. 52. (a) Experimental setup of the stimulated x-ray emission from a $5M$ solution of a $MnCl_2$ complex. The incoming XFEL pulses are focused onto the liquid jet. (b) Sketch of the stimulated x-ray emission. The arrows represent incoming (green) and emitted (red) photons, while the circles indicate the excited (filled) and nonexcited (open) Mn ions, respectively. (c) Detected number of photons in the Mn K_{α_1} region (5 eV integration window) as a function of the nominal incoming XFEL pulse energy for the $5M$ $MnCl_2$ solution. The actual pulse energy on the target is ~20% of the nominal pulse energy shown. The 50 strongest shots in each 0.1 mJ interval are shown in orange; all other shots are shown in black. From Kroll *et al.*, 2018.

distribution of the atoms in the course of RIXS. The situation is qualitatively different in stimulated RIXS, where the recoil momentum from the absorbing photon is almost exactly compensated for by the recoil momentum of the SRIXS photon emitted in the forward direction. This results in a narrow recoil-less peak in the broad velocity distribution due to the recoil from spontaneous photons. This effect is in close analogy to both the Doppler-free two-photon absorption peak in a standing wave (Popova *et al.*, 1970) and laser cooling (Kazantsev, Surdutovich, and Yakovlev, 1990).

The stimulated elastic scattering into the forward direction of the incident narrow bandwidth XFEL pulses was evidenced by the characteristic disappearance of both charge and magnetic diffraction contrast at the Co L_3 resonance scattering (778 eV) of the Co/Pd multilayer worm domain sample (Wu *et al.*, 2016).

A two-color all x-ray pump-probe experiment with sub-70 fs temporal resolution selectively probes the response of orbital and charge degrees of freedom in the prototypical functional oxide magnetite after photoexcitation (Pontius *et al.*, 2018). It was found that the electronic order was quenched on a timescale of ~30 fs, and hence most likely faster than what is expected for any lattice dynamics. One of the main applications of XFELs is related to a unique opportunity to study the dynamics of quantum systems in real time using time-resolved RIXS (Beye, Wernet *et al.*, 2013); see Sec. XIV.E.

B. Second-harmonic generation

High pulse intensities of XFEL create room for studies of nonlinear effects such as second-harmonic generation (SHG) in the x-ray energy range. SHG is a nonlinear optical process of sum frequency generation that produces new photons with twice the frequency. SHG has traditionally been studied as an even-order nonlinear optical effect allowed in the media without inversion symmetry and is one of the best-understood nonlinear effects in optics (Boyd, 2010). Pioneering studies by Shwartz *et al.* (2014) and Yudovich and Shwartz (2015) recently gave experimental evidence for "off-resonant" SHG in diamond in the hard x-ray region with a pump frequency of 7.3 keV and a SHG efficiency of 5.8×10^{-11}. Note the theoretical studies of x-ray SHG in solids (Nazarkin *et al.*, 2003) and the gas phase (Liu, Miron *et al.*, 2019), where this process is also allowed due to inversion symmetry.

C. Superfluorescence and superradiance

Superfluorescence (SF) is a fundamental collective process (Bonifacio and Lugiato, 1975) in which a short pump pulse excites the initially incoherent ensemble of N atoms. SF starts from spontaneous emission that couples the radiation phases of different atoms building up a macroscopic dipole. This gives rise to a SF pulse delayed by the time $\tau_D \propto (\ln N)/N$ needed for the individual dipoles to become phase locked. The intrinsic properties of SF are the scaling law for the intensity of the coherent process ($\propto N^2$) and the Burnham-Chiao ringing (Burnham and Chiao, 1969; Sun, Liu *et al.*, 2010). One should distinguish SF from the superradiance (SR) of Dicke (1954), where a macroscopic dipole moment is created

in advance by the collective excitation process. The time delay τ_D is unique for SF, yet absent in SR and amplified spontaneous emission.

The SF was observed in the extreme ultraviolet (XUV) region in the course of the propagation of partially coherent XFEL SACLA pulses with a wavelength of 24.3 nm through a dense helium gas (Harries *et al.*, 2018). Intense, highly directional emission on the $2p \rightarrow 1s$ transition (30.4 nm/40.79 eV) in pumped He^+ ions was observed and interpreted as yoked SF (Brownell, Lu, and Hartmann, 1995).

The SF was detected by measuring its fingerprint as a decrease of the delay time τ_D with an increase of the pressure; see Fig. 53. Combined experimental (the CAMP end station of the FLASH facility) and theoretical study of XUV SF was done in xenon gas pumped by photons of 73 and 92 eV, tuned below and on the giant $4d$ resonance, respectively (Mercadier *et al.*, 2019). Population inversion is achieved by Auger pumping via the rapid Auger decay following the photoionization of the $4d$ shell of Xe. It was speculated that the emission at 65.18 and 68.14 nm could stem from SF, based on the measured line broadening and emission yield (Mercadier *et al.*, 2019). However, no other proof that this is SF was presented.

The SR in crystals at the Mössbauer transition of nuclei was predicted by Afanas'ev and Kagan (1965) and Hannon and Trammell (1989). A speedup of decay relative to the natural decay was observed in the $^{57}FeBO_3$ crystal (14.4 keV ^{57}F nuclear transition) (van Bürck *et al.*, 1987) at the Bragg condition. Chumakov *et al.* (2018) used resonant diffraction of x rays from the SACLA XFEL (the Mössbauer 14.4 keV nuclear transition of ^{57}Fe nuclei) to investigate SR decay in $^{57}FeBO_3$.

D. Self-induced x-ray transparency

Another milestone phenomenon related to resonant pulse propagation is the effect of self-induced transparency, which is well known in optical-laser spectroscopy (Allen and Eberly, 1987). In fact, there are two effects named self-induced transparency. The first one is the self-induced transparency by McCall and Hahn (1967), which takes place for $n\pi$ pulses shorter than the inverse homogeneous broadening of the spectral transition. This effect was used successfully for the compression and enhancement of optical pulses (Allen and Eberly, 1987) and analyzed theoretically for intense x-ray pulses (Sun, Liu *et al.*, 2010; Li, Labeye *et al.*, 2020). The second one is caused by the saturation of the spectral transition when the absorption probability $\sigma_{\rm abs} \propto \rho_{11} - \rho_{00} \rightarrow 0$ because the populations of the excited ρ_{11} and ground ρ_{00} states become equal for a high intensity of the pump pulse (McCall and Hahn, 1967). The self-induced transparency caused by the saturation effect was recently observed in the x-ray range (Chen *et al.*, 2018) in the Co/Pd multilayer sample using 2.5 and 25 fs SASE pulses at the LCLS with the photon energy around a Co L_3 resonance of 778 eV (Fig. 54).

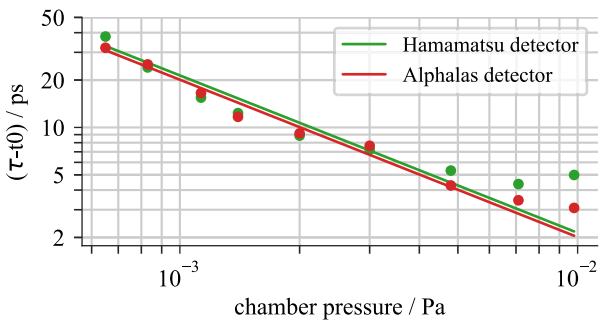

FIG. 53. Higher number densities lead to larger peaks with shorter delays, a hallmark of superfluorescence. From Harries *et al.*, 2018.

E. Time-resolved RIXS studies of magnetic excitations

Investigation of the dynamics of magnetic correlations in doped Mott insulators sheds light on our understanding of the pseudogap, non-Fermi liquids, and high-temperature superconductivity. Recently time-resolved magnetic RIXS (tr-RIXS) at XFELs was used to directly determine the magnetic dynamics after photodoping the Mott insulator Sr_2IrO_4 (Dean *et al.*, 2016; Cao *et al.*, 2019). Pump laser pulses with an energy of 620 meV (2 μm) drive carriers from the lower Hubbard band to the upper Hubbard band. The incident x-ray pulses excite an Ir $2p$ core electron into the $5d$ valence band to couple to the spin degree of freedom. Through the resonant magnetic x-ray scattering mechanism, photons scattered at around 90° were measured as a function of the momentum transfer $\mathbf{Q}$, the energy loss E, and time delay t. The chosen pump level 6 mJ cm^{-2} corresponds to what was required for destroying 3D magnetic order. Orbital excitations $J_{\rm eff} = 1/2 \rightarrow 3/2$ appear in the RIXS spectra at around 600 meV. Figure 55(a) shows the experimental RIXS spectra at equilibrium (50 ps before the pump) and in the transient state after pumping. The low-energy excitation spectrum features a dispersing spin wave below 200 meV and an orbital excitation at around 600 meV.

Despite the almost-complete destruction of the magnetic Bragg peak in the transient state, magnons are still observed at both $\mathbf{Q}$ points. One can see that the magnon at $(\pi, 0)$ is identical before and after the pump. At (π, π), however, there is an appreciable change. This indicates that the high-energy ~200 meV correlations at $(\pi, 0)$ are more robust than the lower-energy spin wave at $(\pi, \pi) \lesssim 100$ meV. A possible reason for this is that higher-energy magnons recover their

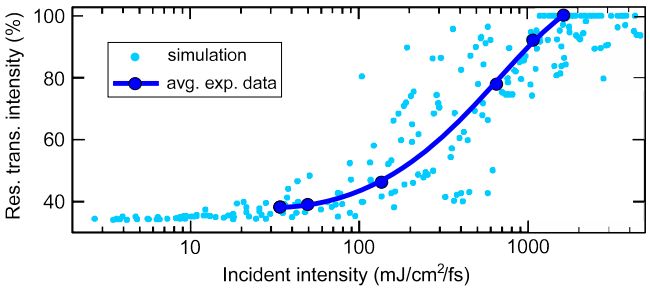

FIG. 54. Experimentally observed change in the transmitted intensity as a function of the incident intensity (solid blue circles and line). Each data point is an average over multiple shots. The open blue circles correspond to the simulated shot-by-shot response. Adapted from Chen *et al.*, 2018.

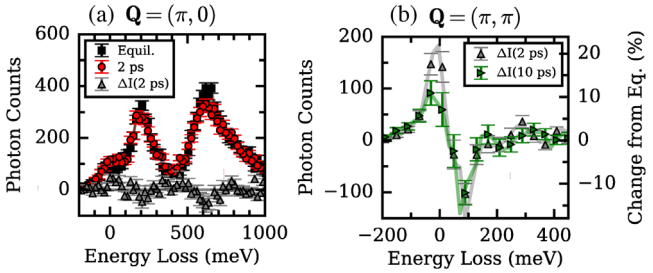

FIG. 55. (a) tr-RIXS spectra showing magnetic excitations (0–200 meV) and orbital excitations (∼600 meV) in equilibrium states of 50 ps before photoexcitation (labeled Equil.) and 2 ps after photoexcitation. (b) Intensity difference spectra ΔI between the equilibrium state and the 2 ps transient state and between the equilibrium state and 10 ps. This shows a depletion of approximately 20% of the magnetic spectral weight of ∼100 meV and additional spectral intensity appearing at low energy. Adapted from Dean *et al.*, 2016.

equilibrium configuration in less than 2 ps because a higher-energy excitation can decay into lower-energy multiparticle excitations in a greater number of different ways than can the lower-energy magnons. The current stage of time-resolved RIXS in pumped Mott insulators was given by Chen *et al.* (2019) and Wang *et al.* (2020).

Mitrano *et al.* (2019a, 2019b) exploited tr-RIXS to characterize photoinduced decoherence of charge excitations in stripe-ordered $La_{2-x}Ba_xCuO_4$, where transient superconductivity had previously been observed (Nicoletti *et al.*, 2014).

F. Dynamics of liquid-liquid phase transitions revealed by ultrashort optical pump and XFEL probe pulses

Unique properties of XFELs allow one to study the melting dynamics and, more generally, liquid-liquid phase transitions, as demonstrated recently for crystalline silicon (Beye *et al.*, 2010). Silicon is one representative out of an entire class of so-called tetrahedral network formers, spanning from IV-V and III-V semiconductors like silicon, germanium, indium antimonide to silica, carbon, and water. These materials commonly share a phase diagram with many stable phases, including the ability to form glasses and different liquid phases. Many predictions about the existence of a liquid-liquid phase transition have been made in theory (Ganesh and Widom, 2009). However, it is difficult experimentally to directly access the relevant temperatures and pressures because the phases of interest are metastable on a picosecond timescale.

The optical excitation of electrons in a crystalline silicon from the valence to the conduction band by a 3.1 eV femtosecond pump laser pulse generates enough energy in the form of "hot electrons." Because of electron-phonon coupling, the excited electrons lose their energy to the lattice (Beye *et al.*, 2009), the temperature and pressure in the sample increases, and the sample melts into a liquid state. The electronic structure of the liquid phase was characterized by x-ray emission induced by the time-delayed soft x-ray pulse from FLASH (Ganesh and Widom, 2009). It was found that the molten silicon is semimetallic with a pseudogap in the density of states around the Fermi level, which is characteristic of the

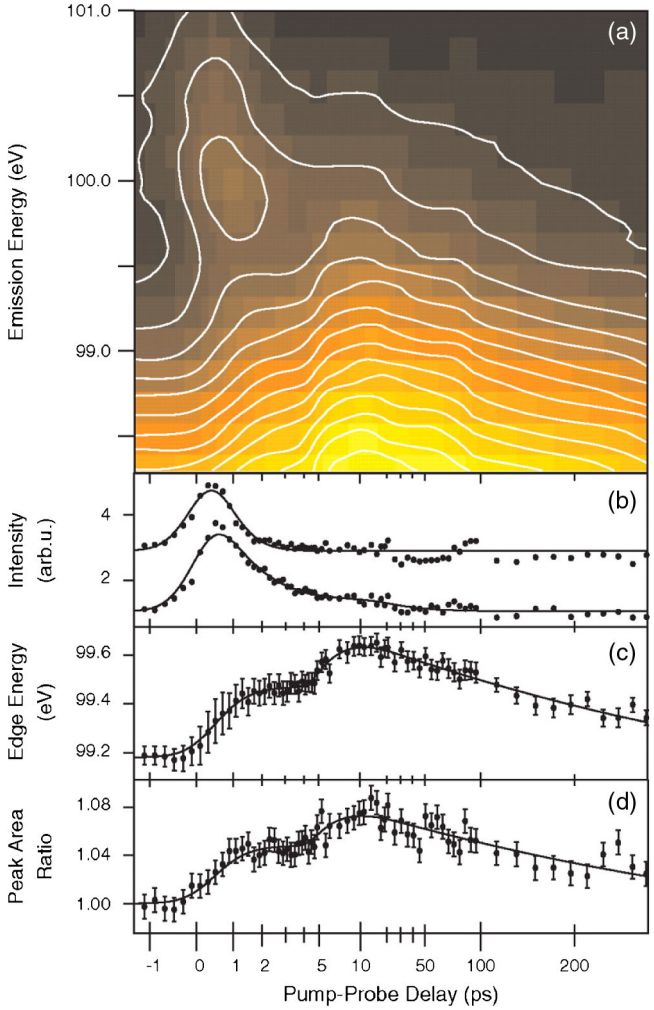

FIG. 56. Two distinct phase transitions are visible in the electronic structure of silicon. (a) In the false color map of the band gap region (higher intensities are brighter) with smooth white lines of equal intensity, the transient occupation of the conduction band and the transitions to the LDL phase in the first picosecond and to the HDL phase around 6 ps are obvious. (b) Hot electrons appear in time with laser excitation in the conduction band. Highly excited electrons decay faster than thermalized electrons trapped at the conduction band bottom. (c) The phase transitions shift the valence band edge. The transition to the LDL phase starts with the electronic excitation. The plateau between 2 and 4 ps followed by a step is the footprint of the first-order phase transition to the HDL state. (d) The structure of stronger bound states changes alongside and is prominently represented by the changing ratio of the L_1 and L_2 peaks in the x-ray emission. From Beye *et al.*, 2010.

LDL, with a density similar to that of the crystal. Silicon stays in this phase for the first 4 ps after laser excitation because the transition to the metallic without a band gap HDL phase takes around 1.5 ps (Fig. 56).

G. Time-resolved UV pump RIXS probe spectroscopy to monitor reaction paths in chemical processes in solution

The development of time-resolved techniques based on the use of XFEL and HHG sources enables investigations of

ultrafast processes including both spectroscopic probes and scattering (Kraus *et al.*, 2018; Schoenlein *et al.*, 2019; Wernet, 2019). The ability of time-resolved RIXS, involving a photon-in and photon-out probe, to deeply penetrate a condensed phase sample can be used to investigate photoinduced reactions in solution, with element selectivity and chemical sensitivity. In this section, we focus on time-resolved RIXS measurements, although other important and related techniques include valence-to-core x-ray emission (Gallo and Glatzel, 2014), x-ray absorption, and photoelectron spectroscopy.

Laser pump x-ray probe RIXS spectroscopy, supported by spectral fingerprints from static experiments or advanced quantum-chemical calculations (Wernet *et al.*, 2015; Norell *et al.*, 2018), allows one to investigate photoinduced processes by probing short-lived intermediates and population dynamics of different chemical species. Time-resolved Fe L-edge RIXS has been employed to study the photodissociation of iron pentacarbonyl [$Fe(CO)_5$] in solution (Wernet *et al.*, 2015) using the LCLS (Emma *et al.*, 2010). The removal of CO generates a $Fe(CO)_4$ species (Fig. 57), which subsequently may be involved in solvent association. Theoretical analysis of the transient RIXS signal allowed for detailed insight into the excited state dynamics, in which decreasing ligand coordination when going from $Fe(CO)_5$ to $Fe(CO)_4$ causes changes in the frontier-orbital interactions. A valence hole localized on the metal and a concomitant decrease in the d_π-d_σ^* splitting are manifested in the Fe L_3-edge RIXS spectra at time delays of 0–700 fs [Fig. 57(c), middle panel] as a new low-energy XAS resonance at 706.5 eV and a redshift in the energy transfer of the main RIXS feature relative to that of $Fe(CO)_5$. Subsequently restored $2p \rightarrow$ LUMO and $d_\pi \rightarrow d_\sigma^*$ transition energies, comparable to $Fe(CO)_5$, at late delays of 0.7–3.5 ps [Fig. 57(c), bottom panel] were explained by reformation of a fifth Fe–C bond that is indicative of solvent association. The transient RIXS signal could be explained by assuming branching involving intersystem crossing into a chemically inert triplet $Fe(CO)_4$ species and a reactive singlet $Fe(CO)_4$ pathway leading to solvent association (Wernet *et al.*, 2015). In a further theoretical analysis of ultrahigh energy resolution or ultrahigh time resolution (Kunnus *et al.*, 2016a), the possibility of probing the initial steps in the excited state dynamics in future experiments with improved settings was proposed. In particular, the search for antistokes RIXS features was identified as a means of identifying valence-excited states of the same multiplicity as the ground state.

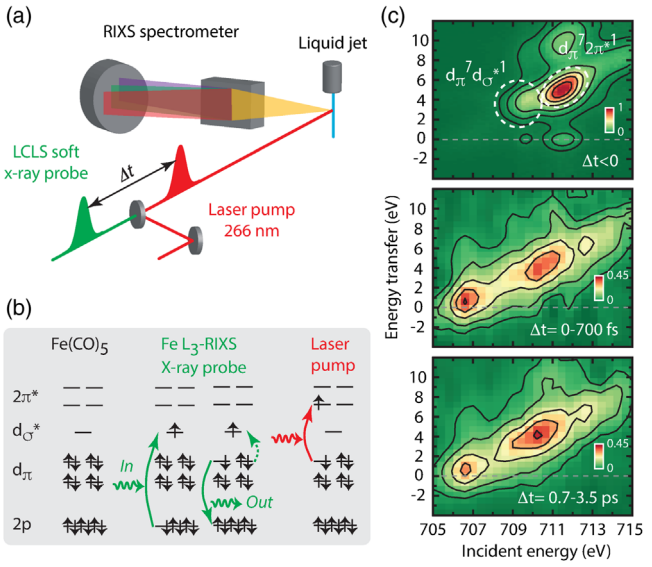

FIG. 57. Schemes and results of the time-resolved RIXS experiment on $Fe(CO)_5$ in an ethanolic solution. (a) Optical-laser pump and soft x-ray probe setup with pump-probe time delay Δt. (b) RIXS and valence transitions in $Fe(CO)_5$. (c) RIXS intensities measured at the Fe L_3 edge. Top panel: ground state $Fe(CO)_5$ (probed before pump). Middle and bottom panels: intensities for transient species at delay intervals Δt = 0–700 fs and 0.7–3.5 ps, respectively. From Wernet *et al.*, 2015.

Time-resolved RIXS spectroscopy has also been employed to study coupled electron-nuclear dynamics involving charge-transfer excitations in iron hexacyanide in aqueous solution using Fe L-edge RIXS (Jay *et al.*, 2018) complemented by theoretical simulations to determine the spectral fingerprint of possible reaction intermediates (Norell *et al.*, 2018), which could help identify a short-lived quartet state suggested to mediate the repopulation of the electronic ground state. As a natural probe of changes in chemical bonding, N K-edge RIXS has been used to investigate the electron dynamics leading to excited state proton transfer in 2-thiopyridone in an aqueous solution (Eckert *et al.*, 2017). However, further studies at high time resolution and improved statistics are required to resolve the relation to measurements with IR and N K-edge and S K-edge x-ray absorption probes.

XV. SUMMARY

In this review, we survey resonant inelastic x-ray and resonant Auger scattering. We focus both on the basic processes in these akin x-ray processes and on the information about electron-nuclear dynamics in free molecules, liquids, and solids that can be extracted from RIXS and RAS experiments. Over the past decade we have witnessed a significant increase in the brightness of tunable synchrotron radiation light sources and a tremendous improvement in spectral resolution of spectrometers. Energy transfers in the range of a few meV give access to detailed measurements of collective excitations in correlated materials and collective dynamics in noncrystalline materials.

Both RIXS and RAS can be considered kinds of pump-probe experiments. The concept of scattering duration (Gel'mukhanov *et al.*, 1999) controlled by the detuning brings effective "time resolution" in these processes even when continuous wave x rays are used. Sometimes the lifetime of the core-excited state serves the role of a delay time between the absorption and decay processes (Brühwiler, Karis, and Mårtensson, 2002; Céolin *et al.*, 2019). The effective time resolution in these measurements introduces nonequilbrium dynamics in x-ray spectroscopy. This type of implicitly time-resolved measurements has been performed to study down to femtosecond electron-nuclear (Gel'mukhanov and Ågren, 1999) and charge-transfer dynamics (Brühwiler, Karis, and Mårtensson, 2002). The ultrafast electronic wave packet dynamics (attosecond and below) (Schweigert and Mukamel, 2007) is the challenge for actually time-resolved

pump-probe x-ray spectroscopy. For example, the tunneling through the effective barrier in the case of shape resonances (Stöhr, 1992) or the set of problems related to relaxation of the electron cloud on the created core hole (Calegari *et al.*, 2014).

X-ray free-electron lasers being new, large-scale research facilities, allow us to film electron-nuclear dynamics and chemical reactions in real time varying the time delay between pump and probe pulses. The goal is a deeper understanding of ultrafast phenomena in atomic physics, chemistry, materials science, and structural biology (Khalil and Mukamel, 2020). One of the main applications is the extension of RIXS into the time domain making use of stimulated RIXS or a RIXS probe of a laser pumped system. The combination of XFELs and synchronized optical lasers enables pump-probe measurements of previously inaccessible processes in short-lived and extreme states of matter generated by optical lasers (Wernet *et al.*, 2015; Picón *et al.*, 2016; Chen *et al.*, 2019; Wernet, 2019; Wang *et al.*, 2020; Liu, Savchenko, Kimberg, Gel'mukhanov, and Odelius, 2021; Liu, Savchenko, Kimberg, Odelius, and Gel'mukhanov, 2021); see Secs. XIV.E–XIV.G. Pumping the ground-state vibrational levels with an IR field strongly changes and elongates the vibrational progression in XAS and in the quasielastic RIXS channel of isolated molecules and liquids. This IR pump x-ray-probe spectroscopy opens new opportunities to reach the high-energy part of intermolecular and intramolecular potentials and to study the influence of hydrogen bonding on the long-range part of the OH potential in various molecular liquids.

Ultrashort and highly intense x-ray pulses generated at the XFELs make it possible to study the effects of nonlinearity on x-ray optics and narrowing of x-ray pulses (Sun, Liu *et al.*, 2010). With x-ray flashes of unprecedented brightness and shortness, the XFELs allow direct observation of single molecules and atoms. For example, the high flux of XFEL can be used to observe recently predicted recoil-induced dissociation (Liu, Vaz da Cruz *et al.*, 2019). Seeded XFELs (Callegari *et al.*, 2021) open possibilities to perform phase sensitive x-ray pump-probe measurements, of which we evidenced only the initial steps. For example, symmetry-forbidden RIXS induced by coherent mixing of core-excited states of opposite parity (Liu *et al.*, 2008). Special attention should be paid to study stimulated x-ray emission and RIXS (Kroll *et al.*, 2020), and four-wave mixing (Tanaka and Mukamel, 2002). The next goal is the physics of phase transitions shedding light on most extreme and exotic forms of matter.

Strong attosecond XFEL fields, in which the phase of each oscillation is locked to the pulse envelope, offer new tools to control and manipulate using the currents and flow of spin in solids and to create and explore new phases of materials. There is an example of shaping matter with intense light in which the electron motion is dominated by the laser field, but the electron is still bound to the atomic core; this is the so-called Kramers-Henneberger atom (Henneberger, 1968; Matthews *et al.*, 2018).

Many applications, like the measurement of element-specific spatial correlation functions and pump-probe spectroscopy, need a high longitudinal coherence of x-ray radiation. Although SASE-based XFEL light has a high transverse coherence, its longitudinal coherence remains low. Longitudinal coherence can be obtained using a multistage cascade seeding scheme (Petrillo *et al.*, 2020). Another leading candidate for obtaining longitudinal coherence cavity-based XFELs (Kim, Shvyd'ko, and Reiche, 2008; Shvyd'ko, 2019) is capable of generating fully coherent x-ray beams of high brilliance and stability, as in classical lasers.

Regarding the experimental and theoretical studies of liquids, despite much progress in the field, one can infer that controversies in studies of these complex systems will remain. This refers to both ambient properties and the regions of phase transition. Here the role of new pump-probe tools and a refinement of theoretical methods are crucial.

This review will increase our understanding of resonant x-ray scattering and help physicists and physical chemists to realize new applications of the techniques and how their research field can benefit from the burgeoning field of synchrotron radiation and XFEL-based research. With the current steady progress in instrumentation, new sources of brilliant and short x-ray pulses, and increasing theoretical expertise, the use of resonant x-ray scattering techniques is becoming increasingly prevalent.

LIST OF SYMBOLS AND ABBREVIATIONS

$\|0\rangle$	ground state
α	fine-structure constant
ω, ω'	frequency of incident and scattered photons
E	energy of Auger electron
$\mathbf{k}, \mathbf{k}'$	momentum of incident and scattered photons
$\mathbf{q}$	transferred momentum $\mathbf{k}' - \mathbf{k}$
$\mathbf{e}, \mathbf{e}'$	polarization vector of incident and scattered photons
$\mathbf{p}$	momentum of electron
ε_ν	vibrational energy
$\mathbf{d}_{ij}$	transition dipole moment
$R_{fi}/\mathcal{R}_{fi}$	anisotropy parameter
M	nuclear mass
H	Hamiltonian
F	scattering amplitude
$\sigma(\omega', \omega)$	RIXS cross section
$\sigma(E, \omega)$	RAS cross section
Ω	detuning of ω from resonance
Γ	lifetime broadening of core-excited state
$\mathbf{G}$	reciprocal lattice vector
θ	angle between $\mathbf{e}$ and $\mathbf{e}'$
χ	angle between $\mathbf{e}$ and $\mathbf{k}'$
Θ	angle between $\mathbf{k}$ and $\mathbf{k}'$
$\mathbf{s}$	spin operator $\boldsymbol{\sigma}/2$
$\boldsymbol{\sigma}$	vector of Pauli matrices
$r_\circ$	classical electron radius
R	interatomic distance
$\mathcal{D}$	Doppler shift
$\mathbf{w}$	angular velocity
1D	one dimensional
BO	Born-Oppenheimer (approximation)
CI	configuration interaction

CT	charge transfer
FC	Franck-Condon (factor)
HB	hydrogen bond
HDL	high-density liquid
HF	Hartree-Fock
HHG	high-harmonic generation
IR	infrared
JT	Jahn-Teller (effect)
KH	Kramers-Heisenberg (equation)
LVI	lifetime vibrational interference
MD	molecular dynamics
MO	molecular orbital
NIXS	nonresonant inelastic x-ray scattering
PEC	potential energy curve
RAS	resonant Auger scattering
RIXS	resonant inelastic x-ray scattering
SACLA	SPring-8 Angstrom Compact Free-Electron Laser
SASE	self-amplified spontaneous emission
SF	superfluorescence
SHG	second-harmonic generation
SR	superradiance
SRIXS	stimulated RIXS
TM	transition metal
tr-RIXS	time-resolved RIXS
VC	vibronic coupling
VSA	vibrational scattering anisotropy
XAS	x-ray absorption spectroscopy
XES	x-ray emission spectroscopy
XFEL	x-ray free-electron Laser
XPS	x-ray photoelectron spectroscopy
YDSE	Young's double-slit experiment

ACKNOWLEDGMENTS

The reported study was funded by the Russian Foundation for Basic Research (RFBR) (Project No. 19-29-12015) and partly supported by the Ministry of Science and Higher Education of the Russian Federation (Project No. FSRZ-2020-0008). M. O. acknowledges funding from the European Union's Horizon 2020 research and innovation program under Marie Skłodowska-Curie Grant Agreement No. 860553, the Carl Tryggers Foundation (Contract No. CTS18:285), and the Swedish Energy Agency (Contract No. 2017-006797). Funding is acknowledged from the European Research Council through ERC-ADG-2014 (Advanced Investigator Grant No. 669531 EDAX) at the University of Potsdam within the Horizon 2020 EU Framework Programme for Research and Innovation. Support from the Helmholtz Association, in particular, the Helmholtz Virtual Institute 419 "Dynamic Pathways in Multidimensional Landscapes" and the Helmholtz-Zentrum Berlin für Materialien und Energie GmbH, is acknowledged. Support from the Swedish Research Council (Grants No. 2019-03470 and No. 2015-03781) is also acknowledged.

REFERENCES

Achkar, A. J., *et al.*, 2012, "Distinct Charge Orders in the Planes and Chains of Ortho-III-Ordered $YBa_2Cu_3O_{6+\delta}$ Superconductors Identified by Resonant Elastic X-Ray Scattering," Phys. Rev. Lett. **109**, 167001.

Adachi, J., N. Kosugi, and A. Yagishita, 2005, "Symmetry-resolved soft x-ray absorption spectroscopy: Its application to simple molecules," J. Phys. B **38**, R127.

Afanas'ev, A. M., and Yu. Kagan, 1965, "Radiation of a system of excited nuclei in a crystal," JETP Lett. **2**, 81–83, https://ui.adsabs.harvard.edu/abs/1965ZhPmR...2..130A/abstract.

Aidas, K., K. V. Mikkelsen, B. Mennucci, and J. Kongsted, 2011, "Fluorescence and phosphorescence of acetone in neat liquid and aqueous solution studied by QM/MM and PCM approaches," Int. J. Quantum Chem. **111**, 1511–1520.

Allen, L., and J. H. Eberly, 1987, *Optical Resonance and Two-Level Atoms* (Dover Publications, New York).

Amann, J., *et al.*, 2012, "Demonstration of self-seeding in a hard-x-ray free-electron laser," Nat. Photonics **6**, 693–698.

Amann-Winkel, K., R. Böhmer, F. Fujara, C. Gainaru, B. Geil, and T. Loerting, 2016, "Colloquium: Water's controversial glass transitions," Rev. Mod. Phys. **88**, 011002.

Ament, L. J. P., G. Ghiringhelli, M. Moretti Sala, L. Braicovich, and J. van den Brink, 2009, "Theoretical Demonstration of How the Dispersion of Magnetic Excitations in Cuprate Compounds Can Be Determined Using Resonant Inelastic X-Ray Scattering," Phys. Rev. Lett. **103**, 117003.

Ament, L. J. P., M. van Veenendaal, T. P. Devereaux, J. P. Hill, and J. van den Brink, 2011, "Resonant inelastic x-ray scattering studies of elementary excitations," Rev. Mod. Phys. **83**, 705.

Anderson, P. W., 1961, "Localized magnetic states in metals," Phys. Rev. **124**, 41.

Argenti, L., *et al.*, 2012, "Double-slit experiment with a polyatomic molecule: Vibrationally resolved C 1*s* photoelectron spectra of acetylene," New J. Phys. **14**, 033012.

Auer, B. M., and J. L. Skinner, 2008, "IR and Raman spectra of liquid water: Theory and interpretation," J. Chem. Phys. **128**, 224511.

Baba, M., I. Hanazaki, and U. Nagashima, 1985, "The $S_1(n,\pi^*)$ states of acetaldehyde and acetone in supersonic nozzle beam: Methyl internal rotation and C = O out-of-plane wagging," J. Chem. Phys. **82**, 3938–3947.

Baev, A., F. Gel'mukhanov, P. Sałek, H. Ågren, K. Ueda, A. de Fanis, K. Okada, and S. Sorensen, 2002, "Doppler interference in dissociative resonant photoemission," Phys. Rev. A **66**, 022509.

Bagger, A., T. Haarman, A. P. Molin, P. G. Moses, H. Ishii, N. Hiraoka, Y.-H. Wu, K.-D. Tsuei, I. Chorkendorff, and F. de Groot, 2017, "$1s2p$ resonant inelastic x-ray scattering combined dipole and quadrupole analysis method," J. Synchrotron Radiat. **24**, 296–301.

Bakker, H. J., and J. L. Skinner, 2010, "Vibrational spectroscopy as a probe of structure and dynamics in liquid water," Chem. Rev. **110**, 1498–1517.

Bao, Z., R. F. Fink, O. Travnikova, D. Céolin, S. Svensson, and M. N. Piancastelli, 2008, "Detailed theoretical and experimental description of normal Auger decay in O_2," J. Phys. B **41**, 125101.

Barletta, Paolo, Sergei V. Shirin, Nikolai F. Zobov, Oleg L. Polyansky, Jonathan Tennyson, Edward F. Valeev, and Attila G. Császár, 2006, "CVRQD *ab initio* ground-state adiabatic potential energy surfaces for the water molecule," J. Chem. Phys. **125**, 204307.

Bednorz, J. G., and K. A. Müller, 1986, "Possible high T_C superconductivity in the Ba-La-Cu-O system," Z. Phys. B. **64**, 189–193.

Bencivenga, F., *et al.*, 2015, "Four-wave mixing experiments with extreme ultraviolet transient gratings," Nature (London) **520**, 205–208.

Benkert, A., F. Meyer, D. Hauschild, M. Blum, W. Yang, R. G. Wilks, M. Bär, F. Reinert, C. Heske, and L. Weinhardt, 2016, "Isotope effects in the resonant inelastic soft x-ray scattering maps of gas-phase methanol, J. Phys. Chem. A **120**, 2260–2267.

Bertie, J. E., and Z. Lan, 1996, "Infrared intensities of liquids XX: The intensity of the OH stretching band of liquid water revisited, and the best current values of the optical constants of H_2O(l) at 25 °C between 15,000 and 1 cm^{-1}," Appl. Spectrosc. **50**, 1047–1057.

Beye, M., F. Hennies, M. Deppe, E. Suljoti, M. Nagasono, W. Wurth, and A. Föhlisch, 2009, "Dynamics of Electron-Phonon Scattering: Crystal- and Angular-Momentum Transfer Probed by Resonant Inelastic X-Ray Scattering," Phys. Rev. Lett. **103**, 237401.

Beye, M., S. Schreck, F. Sorgenfrei, C. Trabant, N. Pontius, C. Schüßler-Langeheine, W. Wurth, and A. Föhlisch, 2013, "Stimulated x-ray emission for materials science," Nature (London) **501**, 191–194.

Beye, M., F. Sorgenfrei, W. F. Schlotter, W. Wurth, and A. Föhlisch, 2010, "The liquid-liquid phase transition in silicon revealed by snapshots of valence electrons," Proc. Natl. Acad. Sci. U.S.A. **107**, 16772–16776.

Beye, M., Ph. Wernet, C. Schüßler-Langeheine, and A. Föhlisch, 2013, "Time resolved resonant inelastic x-ray scattering: A supreme tool to understand dynamics in solids and molecules," J. Electron Spectrosc. Relat. Phenom. **188**, 172–182.

Bisogni, V., *et al.*, 2015, "Orbital Control of Effective Dimensionality: From Spin-Orbital Fractionalization to Confinement in the Anisotropic Ladder System $CaCu_2O_3$," Phys. Rev. Lett. **114**, 096402.

Björneholm, O., 2001, "Direct and indirect methods for studying the energetics and dynamics of the Auger Doppler effect in femtosecond ultra-fast dissociation," J. Chem. Phys. **115**, 4139.

Björneholm, O., S. Sundin, S. Svensson, R. R. T. Marinho, A. Naves de Brito, F. Gel'mukhanov, and H. Ågren, 1997, "Femtosecond Dissociation of Core-Excited HCl Monitored by Frequency Detuning," Phys. Rev. Lett. **79**, 3150–3153.

Björneholm, O., *et al.*, 2000, "Doppler Splitting of In-Flight Auger Decay of Dissociating Oxygen Molecules: The Localization of Delocalized Core Holes," Phys. Rev. Lett. **84**, 2826–2829.

Błachucki, W., J. Szlachetko, J. Hoszowska, J.-Cl. Dousse, Y. Kayser, M. Nachtegaal, and J. Sá, 2014, "High Energy Resolution Off-Resonant Spectroscopy for X-Ray Absorption Spectra Free of Self-Absorption Effects," Phys. Rev. Lett. **112**, 173003.

Blackburn, E., J. Chang, A. H. Said, B. M. Leu, R. Liang, D. A. Bonn, W. N. Hardy, E. M. Forgan, and S. M. Hayden, 2013, "Inelastic x-ray study of phonon broadening and charge-density wave formation in ortho-II-ordered $YBa_2Cu_3O_{6.54}$," Phys. Rev. B **88**, 054506.

Blanco-Canosa, S., *et al.*, 2013, "Momentum-Dependent Charge Correlations in $YBa_2Cu_3O_{6+\delta}$ Superconductors Probed by Resonant X-Ray Scattering: Evidence for Three Competing Phases," Phys. Rev. Lett. **110**, 187001.

Blum, M., M. Odelius, L. Weinhardt, S. Pookpanratana, M. Bär, Y. Zhang, O. Fuchs, W. Yang, E. Umbach, and C. Heske, 2012, "Ultra-fast proton dynamics in aqueous amino acid solutions studied by resonant inelastic soft x-ray scattering, J. Phys. Chem. B **116**, 13757–13764.

Blume, M., 1985, "Magnetic scattering of x-rays," J. Appl. Phys. **57**, 3615–3618.

Bohr, N., 1983, "Discussion with Einstein on epistemological problems in atomic physics," in *Quantum Theory and Measurement*, edited by J. A. Wheeler and W. H. Zurek (Princeton University Press, Princeton, NJ), pp. 9–49.

Bokarev, S. I., and O. Kühn, 2020, "Theoretical x-ray spectroscopy of transition metal compounds," Wiley Interdiscip. Rev. Comput. Mol. Sci. **10**, e1433.

Bonifacio, R., and L. A. Lugiato, 1975, "Cooperative radiation processes in two-level systems: Super fluorescence," Phys. Rev. A **11**, 1507–1521.

Boyd, R. W., 2010, *Nonlinear Optics* (Academic Press, New York).

Braicovich, L., *et al.*, 2014, "The simultaneous measurement of energy and linear polarization of the scattered radiation in resonant inelastic soft x-ray scattering," Rev. Sci. Instrum. **85**, 115104.

Brena, B., D. Nordlund, M. Odelius, H. Ogasawara, A. Nilsson, and L. G. M. Pettersson, 2004, "Ultrafast Molecular Dissociation of Water in Ice," Phys. Rev. Lett. **93**, 148302.

Brookes, N. B., *et al.*, 2018, "The beamline ID32 at the ESRF for soft x-ray high energy resolution resonant inelastic x-ray scattering and polarisation dependent x-ray absorption spectroscopy," Nucl. Instrum. Methods Phys. Res., Sect. B **903**, 175–192.

Brownell, J. H., X. Lu, and S. R. Hartmann, 1995, "Yoked Superfluorescence," Phys. Rev. Lett. **75**, 3265–3268.

Brühwiler, P. A., O. Karis, and N. Mårtensson, 2002, "Charge-transfer dynamics studied using resonant core spectroscopies," Rev. Mod. Phys. **74**, 703–740.

Burnham, D. C., and R. Y. Chiao, 1969, "Coherent resonance fluorescence excited by short light pulses," Phys. Rev. **188**, 667–675.

Calegari, F., *et al.*, 2014, "Ultrafast electron dynamics in phenylalanine initiated by attosecond pulses," Science **346**, 336–339.

Callegari, C., A. N. Grum-Grzhimailo, K. L. Ishikawa, K. C. Prince, G. Sansone, and K. Ueda, 2021, "Atomic, molecular and optical physics applications of longitudinally coherent and narrow bandwidth free-electron lasers," Phys. Rep. **904**, 1–59.

Canton, S. E., E. Pleśiat, J. D. Bozek, B. S. Rude, P. Decleva, and F. Martin, 2011, "Direct observation of Young's double-slit interferences in vibrationally resolved photoionization of diatomic molecules," Proc. Natl. Acad. Sci. U.S.A. **108**, 7302–7306.

Cao, Y., D. G. Mazzone, D. Meyers, J. P. Hill, X. Liu, S. Wall, and M. P. M. Dean, 2019, "Ultrafast dynamics of spin and orbital correlations in quantum materials: An energy- and momentum-resolved perspective," Phil. Trans. R. Soc. A **377**, 20170480.

Carleer, M., A. Jenouvrier, A.-C. Vandaele, P. F. Bernath, M. F. Mérienne, R. Colin, N. F. Zobov, Oleg L. Polyansky, Jonathan Tennyson, and V. A. Savin, 1999, "The near infrared, visible, and near ultraviolet overtone spectrum of water," J. Chem. Phys. **111**, 2444–2450.

Carlisle, J. A., E. L. Shirley, E. A. Hudson, L. J. Terminello, T. A. Callcott, J. J. Jia, D. L. Ederer, R. C. C. Perera, and F. J. Himpse, 1995, "Probing the Graphite Band Structure with Resonant Soft-X-Ray Fluorescence," Phys. Rev. Lett. **74**, 1234.

Carlisle, J. A., E. L. Shirley, L. J. Terminello, J. J. Jia, T. A. Callcott, D. L. Ederer, R. C. C. Perera, and F. J. Himpsel, 1999, "Band-structure and core-hole effects in resonant inelastic soft-x-ray scattering: Experiment and theory," Phys. Rev. B **59**, 7433.

Carniato, S., R. Guillemin, W. C. Stolte, L. Journel, R. Taïeb, D. W. Lindle, and M. Simon, 2009, "Experimental and theoretical investigation of molecular field effects by polarization-resolved resonant inelastic x-ray scattering," Phys. Rev. A **80**, 032513.

Carniato, S., P. Selles, L. Journel, R. Guillemin, W. C. Stolte, L. El Khoury, T. Marin, F. Gel'mukhanov, D. W. Lindle, and M. Simon,

2012, "Thomson-resonant interference effects in elastic x-ray scattering near the Cl *K* edge of HCl," J. Chem. Phys. **137**, 094311.
Carra, P., M. Fabrizio, and B. T. Thole, 1995, "High Resolution X-Ray Resonant Raman Scattering," Phys. Rev. Lett. **74**, 3700–3703.
Caupin, F., and M. A. Anisimov, 2019, "Thermodynamics of supercooled and stretched water: Unifying two-structure description and liquid-vapor spinodal," J. Chem. Phys. **151**, 034503.
Caux, J.-S., and R. Hagemans, 2006, "The four-spinon dynamical structure factor of the Heisenberg chain," J. Stat. Mech. P12013.
Céolin, D., *et al.*, 2019, "Recoil-induced ultrafast molecular rotation probed by dynamical rotational Doppler effect, Proc. Natl. Acad. Sci. U.S.A. **116**, 4877–4882.
Cesar, A., F. Gel'mukhanov, Y. Luo, H. Ågren, P. Skytt, P. Glans, J. Guo, K. Gunnelin, and J. Nordgren, 1997, "Resonant x-ray scattering beyond the Born-Oppenheimer approximation: Symmetry breaking in the oxygen resonant x-ray emission spectrum of carbon dioxide," J. Chem. Phys. **106**, 3439.
Chainani, A., *et al.*, 2013, "Quantifying covalency and metallicity in correlated compounds undergoing metal-insulator transition," Phys. Rev. B **87**, 045108.
Chaix, L., *et al.*, 2017, "Dispersive charge density wave excitations in $Bi_2Sr_2CaCu_2O_{8+\delta}$," Nat. Phys. **13**, 952.
Chandler, D., 2016, "Metastability and no criticality," Nature (London) **531**, E1–E2.
Chang, J., *et al.*, 2012, "Direct observation of competition between superconductivity and charge density wave order in $YBa_2Cu_3O_{6.67}$," Nat. Phys. **8**, 871.
Chen, C.-C., M. van Veenendaal, T. P. Devereaux, and K. Wohlfeld, 2015, "Fractionalization, entanglement, and separation: Understanding the collective excitations in a spin-orbital chain," Phys. Rev. B **91**, 165102.
Chen, W., X. Wu, and R. Car, 2010, "X-Ray Absorption Signatures of the Molecular Environment in Water and Ice," Phys. Rev. Lett. **105**, 017802.
Chen, Y., Y. Wang, C. Jia, B. Moritz, A. M. Shvaika, J. K. Freericks, and T. P. Devereaux, 2019, "Theory for time-resolved resonant inelastic x-ray scattering," Phys. Rev. B **99**, 104306.
Chen, Z., *et al.*, 2018, "Ultrafast Self-Induced X-Ray Transparency and Loss of Magnetic Diffraction," Phys. Rev. Lett. **121**, 137403.
Chiuzbăian, G. S., *et al.*, 2008, "Combining *M*- and *L*-edge resonant inelastic x-ray scattering for studies of 3*d* transition metal compounds," Phys. Rev. B **78**, 245102.
Chubar, O., G. Geloni, V. Kocharyan, A. Madsen, E. Saldin, S. Serkez, Y. Shvyd'ko, and J. Sutter, 2016, "Ultra-high-resolution inelastic x-ray scattering at high-repetition-rate self-seeded x-ray free-electron lasers," J. Synchrotron Radiat. **23**, 410–424.
Chumakov, A. I., *et al.*, 2018, "Superradiance of an ensemble of nuclei excited by a free electron laser," Nat. Phys. **14**, 261–264.
Clark, G. N. I., G. L. Hura, J. Teixeira, A. K. Soper, and T. Head-Gordon, 2010, "Small-angle scattering and the structure of ambient liquid water," Proc. Natl. Acad. Sci. U.S.A. **107**, 14003–14007.
Cohen, H. D., and U. Fano, 1966, "Interference in the photoionization of molecules," Phys. Rev. **150**, 30.
Coheur, P.-F., S. Fally, M. Carleer, C. Clerbaux, R. Colin, A. Jenouvrier, M.-F. Mérienne, C. Hermans, and A. C. Vandaele, 2002, "New water vapor line parameters in the 26000–13000 cm^{-1} region," J. Quant. Spectrosc. Radiat. Transfer **74**, 493–510.
Comin, R., and A. Damascelli, 2016, "Studies of charge order in cuprates," Annu. Rev. Condens. Matter Phys. **7**, 369.
Comin, R., R. Sutarto, E. H. da Silva Neto, L. Chauviere, R. Liang, W. N. Hardy, D. A. Bonn, F. He, G. A. Sawatzky, and A. Damascelli, 2015, "Broken translational and rotational symmetry via charge stripe order in underdoped $YBa_2Cu_3O_{6+y}$," Science **347**, 1335.
Couto, R. C., *et al.*, 2016a, "Coupled electron-nuclear dynamics in resonant $1\sigma \rightarrow 2\pi$ x-ray Raman scattering of CO molecules," Phys. Rev. A **93**, 032510.
Couto, R. C., *et al.*, 2016b, "Anomalously strong two-electron one-photon x-ray decay transitions in CO caused by avoided crossing," Sci. Rep. **6**, 20947.
Couto, R. C., *et al.*, 2017, "Selective gating to vibrational modes through resonant x-ray scattering," Nat. Commun. **8**, 14165.
Császár, A. G, T. E. Mátyusa, Szidarovszky, L. Lodi, N. F. Zobov, S. V. Shirin, O. L. Polyansky, and J. Tennyson, 2010, "First-principles prediction and partial characterization of the vibrational states of water up to dissociation," J. Quant. Spectrosc. Radiat. Transfer **111**, 1043–1064.
Das, L., *et al.*, 2018, "Spin-Orbital Excitations in Ca_2RuO_4 Revealed by Resonant Inelastic X-Ray Scattering," Phys. Rev. X **8**, 011048.
Das, S. C., R. J. Green, J. Podder, T. Z. Regier, G. S. Chang, and A. Moewes, 2013, "Band gap tuning in ZnO through Ni doping via spray pyrolysis," J. Phys. Chem. C **117**, 12745–12753.
da Silva Neto, E. H., R. Comin, F. He, R. Sutarto, Y. Jiang, R. L. Greene, G. A. Sawatzky, and A. Damascelli, 2015, "Charge ordering in the electron-doped superconductor $Nd_{2-x}Ce_xCuO_4$," Science **347**, 282.
Dean, M. P. M., *et al.*, 2016, "Ultrafast energy- and momentum-resolved dynamics of magnetic correlations in the photo-doped Mott insulator Sr_2IrO_4," Nat. Mater. **15**, 601–605.
de Groot, F., 2001, "High-resolution x-ray emission and x-ray absorption spectroscopy," Chem. Rev. **101**, 1779–1808.
de Groot, F., 2005, "Multiplet effects in x-ray spectroscopy," Coord. Chem. Rev. **249**, 31–63.
de Groot, F., J. Fuggle, B. Thole, and G. Sawatzky, 1990, "2*p* x-ray absorption of 3*d* transition-metal compounds: An atomic multiplet description including the crystal field," Phys. Rev. B **42**, 5459.
de Groot, F. M. F., and A. Kotani, 2008, *Core Level Spectroscopy of Solids* (CRC Press, Boca Raton).
de Groot, F. M. F., P. Kuiper, and G. A. Sawatzky, 1998, "Local spin-flip spectral distribution obtained by resonant x-ray Raman scattering," Phys. Rev. B **57**, 14584–14587.
Demekhin, Ph. V., I. D. Petrov, V. L. Sukhorukov, W. Kielich, A. Knie, H. Schmoranzer, and A. Ehresmann, 2010a, "Strong interference effects in the angularly resolved Auger decay and fluorescence emission spectra of the core-excited NO molecule," J. Phys. B **43**, 165103.
Demekhin, Ph. V., I. D. Petrov, V. L. Sukhorukov, W. Kielich, A. Knie, H. Schmoranzer, and A. Ehresmann, 2010b, "Symmetry Forbidden Electronic State Interference Observed in Angularly Resolved NO^+ $(A^1\Pi)$ Deexcitation Spectra of the N^*O $(2\sigma^{-1}2\pi^2)$ Resonance," Phys. Rev. Lett. **104**, 243001.
Demekhin, Ph. V., I. D. Petrov, T. Tanaka, M. Hoshino, H. Tanaka, K. Ueda, W. Kielich, and A. Ehresmann, 2010, "Large impact of the weak direct photoionization on the angularly resolved $CO^+(A^2\Pi)$ de-excitation spectra of the $CO^*(1\sigma^{-1}2\pi)$ resonance," J. Phys. B **43**, 065102.
Dicke, R. H., 1954, "Coherence in spontaneous radiation processes," Phys. Rev. **93**, 99.
Dirac, P. A. M., 1927, "The quantum theory of the emission and absorption of radiation," Proc. R. Soc. A **114**, 243–265.
Domcke, W., and L. S. Cederbaum, 1978, "Electronic recoil effects in high-energy photoelectron spectroscopy," J. Electron Spectrosc. Relat. Phenom. **13**, 161–173.
Doniach, S., and E. H. Sondheimer, 1998, *Green's Functions for Solid State Physicists* (Imperial College Press, London).

Dressel, M., 2018, "Advances in organic conductors and superconductors," Crystals **8**, 332.

Duris, J., *et al.*, 2020, "Tunable isolated attosecond x-ray pulses with gigawatt peak power from a free-electron laser," Nat. Photonics **14**, 30–36.

Eckert, S., *et al.*, 2017, "Ultrafast independent N–H and N–C bond deformation investigated with resonant inelastic x-ray scattering," Angew. Chem., Int. Ed. Engl. **56**, 6088–6092.

Eckert, S., *et al.*, 2018, "One-dimensional cuts through multidimensional potential-energy surfaces by tunable x-rays," Phys. Rev. A **97**, 053410.

Efetov, K. B., and A. I. Larkin, 1976, "Correlation functions in one-dimensional systems with a strong interaction," Sov. Phys. JETP **42**, 390–396, http://www.jetp.ac.ru/cgi-bin/e/index/e/42/2/p390?a=list.

Eichmann, U., *et al.*, 2020, "Photon-recoil imaging: Expanding the view of nonlinear x-ray physics," Science **369**, 1630–1633.

Ekholm, V., *et al.*, 2020, "Core-hole localization and ultra-fast dissociation in SF_6," J. Phys. B **53**, 185101.

Elfimov, I. S., V. I. Anisimov, and G. A. Sawatzky, 1999, "Orbital Ordering, Jahn-Teller Distortion, and Anomalous X-Ray Scattering in Manganates," Phys. Rev. Lett. **82**, 4264–4267.

Elnaggar, H., R. P. Wang, M. Ghiasi, M. Yañez, M. U. Delgado-Jaime, M. H. Hamed, A. Juhin, S. S. Dhesi, and F. de Groot, 2020, "Probing the local distortion of Fe sites in Fe_3O_4 thin films using enhanced symmetry selection in XMLD," Phys. Rev. Mater. **4**, 024415.

Elnaggar, H., *et al.*, 2019, "Magnetic contrast at spin-flip excitations: An advanced x-ray spectroscopy tool to study magnetic-ordering," ACS Appl. Mater. Interfaces **11**, 36213–36220.

Emma, P., *et al.*, 2010, "First lasing and operation of an ångstrom-wavelength free-electron laser," Nat. Photonics **4**, 641–647.

English, N. J., P. G. Kusalik, and J. S. Tse, 2013, "Density equalisation in supercooled high- and low-density water mixtures," J. Chem. Phys. **139**, 084508.

English, N. J., and J. S. Tse, 2011, "Density Fluctuations in Liquid Water," Phys. Rev. Lett. **106**, 037801.

Ertan, E., M. Lundberg, L. K. Sørensen, and M. Odelius, 2020, "Setting the stage for theoretical x-ray spectra of the H_2S molecule with multi-configurational quantum chemical calculations of the energy landscape," J. Chem. Phys. **152**, 094305.

Ertan, E., *et al.*, 2018, "Ultrafast dissociation features in RIXS spectra of the water molecule," Phys. Chem. Chem. Phys. **20**, 14384–14397.

Fabrizio, M., M. Altarelli, and M. Benfatto, 1998, "X-Ray Resonant Scattering as a Direct Probe of Orbital Ordering in Transition-Metal Oxides," Phys. Rev. Lett. **80**, 3400–3403.

Faddeev, L. D., and L. A. Takhtajan, 1981, "What is the spin of a spin wave?," Phys. Lett. **85A**, 375.

Fatale, S., *et al.*, 2017, "Electronic and magnetic excitations in the half-stuffed Cu-O planes of $Ba_2Cu_3O_4Cl_2$ measured by resonant inelastic x-ray scattering," Phys. Rev. B **96**, 115149.

Feifel, R., *et al.*, 2000, "Observation of a Continuum-Continuum Interference Hole in Ultrafast Dissociating Core-Excited Molecules," Phys. Rev. Lett. **85**, 3133.

Feifel, R., *et al.*, 2002, "Interference Quenching of $\nu'' = 1$ Vibrational Line in Resonant Photoemission of N_2: A Possibility to Obtain Geometrical Information on the Core-Excited State," Phys. Rev. Lett. **89**, 103002.

Feifel, R., *et al.*, 2008, "X-ray absorption and resonant Auger spectroscopy of O_2 in the vicinity of the O $1s \rightarrow \sigma^*$ resonance: Experiment and theory," J. Chem. Phys. **128**, 064304.

Felicíssimo, V. C., F. F. Guimarães, and F. Gel'mukhanov, 2005, "Enhancement of the recoil effect in x-ray photoelectron spectra of molecules driven by a strong IR field," Phys. Rev. A **72**, 023414.

Fischer, H. E., A. C. Barnes, and P. S. Salmon, 2006, "Neutron and x-ray diffraction studies of liquids and glasses," Rep. Prog. Phys. **69**, 233–299.

Forsberg, J., Johan Gråsjö, B. Brena, J. Nordgren, Laurent-C. Duda, and J.-E. Rubensson, 2009, "Angular anisotropy of resonant inelastic soft x-ray scattering from liquid water," Phys. Rev. B **79**, 132203.

Fuchs, O., *et al.*, 2008, "Isotope and Temperature Effects in Liquid Water Probed by X-Ray Absorption and Resonant X-Ray Emission Spectroscopy," Phys. Rev. Lett. **100**, 027801.

Gallo, E., and P. Glatzel, 2014, "Valence to core x-ray emission spectroscopy," Adv. Mater. **26**, 7730–7746.

Ganesh, P., and M. Widom, 2009, "Liquid-Liquid Transition in Supercooled Silicon Determined by First-Principles Simulation," Phys. Rev. Lett. **102**, 075701.

Gao, X., D. Casa, J. Kim, T. Gog, C. Li, and C. Burns, 2016, "Toroidal silicon polarization analyzer for resonant inelastic x-ray scattering," Rev. Sci. Instrum. **87**, 083107.

Gavrilyuk, S., Y.-P. Sun, S. Levin, H. Ågren, and F. Gel'mukhanov, 2010, "Recoil splitting of x-ray-induced optical fluorescence," Phys. Rev. A **81**, 035401.

Gel'mukhanov, F., and H. Ågren, 1994, "Resonant inelastic x-ray scattering with symmetry-selective excitation," Phys. Rev. A **49**, 4378.

Gel'mukhanov, F., and H. Ågren, 1996a, "Raman, non-Raman, and anti-Raman dispersion in resonant x-ray scattering spectra of molecules," Phys. Rev. A **54**, 3960–3970.

Gel'mukhanov, F., and H. Ågren, 1996b, "X-ray resonant scattering involving dissociative states," Phys. Rev. A **54**, 379.

Gel'mukhanov, F., and H. Ågren, 1998a, "Channel interference in x-ray Raman scattering: Parity selection rules, dephasing and localization of core holes," J. Electron Spectrosc. Relat. Phenom. **93**, 31–37.

Gel'mukhanov, F., and H. Ågren, 1998b, "Spectral features of resonant radiative x-ray Raman scattering in polymers and solids," Phys. Rev. B **57**, 2780–2792.

Gel'mukhanov, F., and H. Ågren, 1999, "Resonant x-ray Raman scattering," Phys. Rep. **312**, 87.

Gel'mukhanov, F., H. Ågren, M. Neeb, J.-E. Rubensson, and A. Bringer, 1996, "Integral properties of channel interference in resonant x-ray scattering," Phys. Lett. A **211**, 101–108.

Gel'mukhanov, F., H. Ågren, and P. Sałek, 1998, "Doppler effects in resonant x-ray Raman scattering," Phys. Rev. A **57**, 2511–2526.

Gel'mukhanov, F., H. Ågren, S. Svensson, H. Aksela, and S. Aksela, 1996, "Theory of Auger spectra for molecular-field-split core levels," Phys. Rev. A **53**, 1379–1387.

Gel'mukhanov, F., V. Kimberg, X.-J. Liu, G. Prümper, T. Tanaka, M. Hoshino, H. Tanaka, and K. Ueda, 2007, "Young's double-slit experiment using two-center core-level photoemission: Photoelectron recoil effects," J. Electron Spectrosc. Relat. Phenom. **156–158**, 265–269.

Gel'mukhanov, F., T. Privalov, and H. Ågren, 1998a, "Channel interference in x-ray Raman scattering: Parity selection rules, dephasing and localization of core holes," J. Chem. Phys. **109**, 5060.

Gel'mukhanov, F., T. Privalov, and H. Ågren, 1998b, "Soft and hard x-ray Raman scattering by oriented symmetrical molecules: Selection rules, interference, and dephasing mechanisms," J. Chem. Phys. **109**, 5060.

Gel'mukhanov, F., T. Privalov, and H. Ågren, 2000, "Temperature dependence and Debye-Waller factors for resonant x-ray Raman scattering in solids," Phys. Rev. B **62**, 13996–14005.

Gel'mukhanov, F., P. Sałek, T. Privalov, and H. Ågren, 1999, "Duration of x-ray Raman scattering," Phys. Rev. A **59**, 380.

Gel'mukhanov, F. Kh., and H. Ågren, 1996, "X-Ray Raman scattering involving electronic continuum resonances," J. Phys. B **29**, 2751–2762.

Gel'mukhanov, F. Kh., and L. N. Mazalov, 1977, "Polarisation of the x-ray fluorescence of molecules," Opt. Spektrosk. **42**, 659 [Opt. Spectrosc. (USSR) **42**, 371–374 (1977)].

Gel'mukhanov, F. Kh., L. N. Mazalov, and A. V. Kondratenko, 1977, "A theory of vibrational structure in the x-ray spectra of molecules," Chem. Phys. Lett. **46**, 133–137.

Gel'mukhanov, F. Kh., L. N. Mazalov, and N. A. Shklyaeva, 1975, "An interference effect in x-ray fluorescence spectra," Zh. Eksp. Teor. Fiz. **69**, 1971–1980, http://www.jetp.ac.ru/cgi-bin/dn/e_042_06_1001.pdf.

Gel'mukhanov, F. Kh., L. N. Mazalov, and N. A. Shklyaeva, 1976, "Some features of x-ray fluorescence in metals near the absorption threshold," Zh. Eksp. Teor. Fiz. **71**, 960–976, http://www.jetp.ac.ru/cgi-bin/dn/e_044_03_0504.pdf.

Gel'mukhanov, F. Kh., T. I. Privalov, and H. Ågren, 1997a, "Collapse of vibrational structure in spectra of resonant x-ray Raman scattering," Phys. Rev. A **56**, 256.

Gel'mukhanov, F. Kh., T. I. Privalov, and H. Ågren, 1997b, "Restoration of selection rules in nonadiabatic resonant inelastic x-ray scattering," J. Exp. Theor. Phys. **85**, 20–26.

Ghiringhelli, G., M. Matsubara, C. Dallera, F. Fracassi, R. Gusmeroli, A. Piazzalunga, A. Tagliaferri, N. B. Brookes, A. Kotani, and L. Braicovich, 2005, "NiO as a test case for high resolution resonant inelastic soft x-ray scattering," J. Phys. Condens. Matter **17**, 5397.

Ghiringhelli, G., M. Matsubara, C. Dallera, F. Fracassi, A. Tagliaferri, N. B. Brookes, A. Kotani, and L. Braicovich, 2006, "Resonant inelastic x-ray scattering of MnO: $L_{2,3}$ edge measurements and assessment of their interpretation," Phys. Rev. B **73**, 035111.

Ghiringhelli, G., *et al.*, 2012, "Long-range incommensurate charge fluctuations in $(Y,Nd)Ba_2Cu_3O_{6+x}$," Science **337**, 821.

Giamarchi, T., 2004, *Quantum Physics in One Dimension* International Series of Monographs on Physics Vol. 121 (Clarendon Press, Oxford).

Giamarchi, T., 2016, "One-dimensional physics in the 21st century," C.R. Phys. **17**, 322–331.

Glans, P., K. Gunnelin, P. Skytt, J.-H. Guo, N. Wassdahl, J. Nordgren, F. Kh. Gel'mukhanov, H. Ågren, T. Warwick, and Eli Rotenberg, 1996, "Resonant X-Ray Emission Spectroscopy of Molecular Oxygen," Phys. Rev. Lett. **76**, 2448.

Glans, P., P. Skytt, K. Gunnelin, J.-H. Guo, and J. Nordgren, 1996a, "Selectively excited x-ray emission spectra of N_2," J. Electron Spectrosc. Relat. Phenom. **82**, 193.

Glans, P., P. Skytt, K. Gunnelin, J.-H. Guo, and J. Nordgren, 1996b, "Selectively excited x-ray emission spectra of N_2," J. Electron Spectrosc. Relat. Phenom. **82**, 193–201.

Glatzel, P., and U. Bergmann, 2005, "High resolution 1*s* core hole x-ray spectroscopy in 3*d* transition metal complexes—Electronic and structural information," Coord. Chem. Rev. **249**, 65–95.

Glatzel, P., F. M. F. de Groot, O. Manoilova, D. Grandjean, B. M. Weckhuysen, U. Bergmann, and R. Barrea, 2005, "Range-extended EXAFS at the *L* edge of rare earths using high-energy-resolution fluorescence detection: A study of La in LaOCl," Phys. Rev. B **72**, 014117.

Glatzel, P., L. Jacquamet, U. Bergmann, F. M. F. de Groot, and S. P. Cramer, 2002, "Site-selective EXAFS in mixed-valence compounds using high-resolution fluorescence detection: A study of iron in Prussian blue," Inorg. Chem. **41**, 3121–3127.

Glatzel, P., M. Sikora, and M. Fernández-Garćia, 2009, "Resonant x-ray spectroscopy to study K absorption pre-edges in 3*d* transition metal compounds," Eur. Phys. J. Special Topics **169**, 207–214.

Glover, T. E., *et al.*, 2012, "X-ray and optical wave mixing," Nature (London) **488**, 603–608.

Grechko, M., P. Maksyutenko, N. F. Zobov, S. V. Shirin, O. L. Polyansky, T. R. Rizzo, and Oleg V. Boyarkin, 2008, "Collisionally assisted spectroscopy of water from 27 000 to 34 000 cm^{-1}," J. Phys. Chem. A **112**, 10539–10545.

Grechko, Maxim, Oleg V. Boyarkin, Thomas R. Rizzo, Pavlo Maksyutenko, Nikolay F. Zobov, Sergei V. Shirin, Lorenzo Lodi, Jonathan Tennyson, Attila G. Császár, and Oleg L. Polyansky, 2009, "State-selective spectroscopy of water up to its first dissociation limit," J. Chem. Phys. **131**, 221105.

Green, R. J., D. A. Zatsepin, A. Hunt, E. Z. Kurmaev, N. V. Gavrilov, and A. Moewes, 2013, "The formation of Ti-O tetrahedra and band gap reduction in SiO_2 via pulsed ion implantation," J. Appl. Phys. **113**, 103704.

Guillemin, R., S. Carniato, W. C. Stolte, L. Journel, R. Taïeb, D. W. Lindle, and M. Simon, 2008, "Linear Dichroism in Resonant Inelastic X-Ray Scattering to Molecular Spin-Orbit States," Phys. Rev. Lett. **101**, 133003.

Gunnarsson, O., and K. Schönhammer, 1983, "Electron spectroscopies for Ce compounds in the impurity model," Phys. Rev. B **28**, 4315.

Gunnelin, K., P. Glans, P. Skytt, J.-H. Guo, and J. Nordgren, 1998, "Assigning x-ray absorption spectra by means of soft-x-ray emission spectroscopy," Phys. Rev. A **57**, 864.

Guo, J., P. Skytt, N. Wassdahl, J. Nordgren, Y. Liu, O. Vahtras, and H. Ågren, 1995, "Resonant and non-resonant x-ray scattering from C_{70}," Chem. Phys. Lett. **235**, 152–159.

Haldane, F. D. M., 1981, "Luttinger liquid theory of one-dimensional quantum fluids. I. Properties of the Luttinger model and their extension to the general 1D interacting spinless Fermi gas," J. Phys. C **14**, 2585–2609.

Hämäläinen, K., and S. Manninen, 2001, "Resonant and non-resonant inelastic x-ray scattering," J. Phys. Condens. Matter **13**, 7539–7555.

Hämäläinen, K., D. P. Siddons, J. B. Hastings, and L. E. Berman, 1991, "Elimination of the Inner-Shell Lifetime Broadening in X-Ray-Absorption Spectroscopy," Phys. Rev. Lett. **67**, 2850–2853.

Hancock, J. N., *et al.*, 2010, "Evidence for core-hole-mediated inelastic x-ray scattering from metallic $Fe_{1.087}Te$," Phys. Rev. B **82**, 020513(R).

Hannon, J. P., and G. T. Trammell, 1989, "Coherent excitations of nuclei in crystals by synchrotron radiation pulses," Physica (Amsterdam) **159B**, 161–167.

Harada, Y., J. Miyawaki, H. Niwa, K. Yamazoe, L. G. M. Pettersson, and A. Nilsson, 2017, "Probing the OH stretch in different local environments in liquid water," J. Phys. Chem. Lett. **8**, 5487–5491.

Harada, Y., T. Tokushima, Y. Takata, T. Takeuchi, Y. Kitajima, S. Tanaka, Y. Kayanuma, and S. Shin, 2004, "Dynamical Symmetry Breaking under Core Excitation in Graphite: Polarization Correlation in Soft X-Ray Recombination Emission," Phys. Rev. Lett. **93**, 017401.

Harada, Y., *et al.*, 2013, "Selective Probing of the OH or OD Stretch Vibration in Liquid Water Using Resonant Inelastic Soft-X-Ray Scattering," Phys. Rev. Lett. **111**, 193001.

Hariki, A., R.-P. Wang, A. Sotnikov, K. Tomiyasu, D. Betto, N. B. Brookes, Y. Uemura, M. Ghiasi, F. M. F. de Groot, and J. Kuneš,

2020, "Damping of spinful excitons in $LaCoO_3$ by thermal fluctuations: Theory and experiment," Phys. Rev. B **101**, 245162.
Hariki, A., M. Winder, T. Uozumi, and J. Kuneš, 2020, "LDA + DMFT approach to resonant inelastic x-ray scattering in correlated materials," Phys. Rev. B **101**, 115130.
Harries, J. R., *et al.*, 2018, "Superfluorescence, Free-Induction Decay, and Four-Wave Mixing: Propagation of Free-Electron Laser Pulses through a Dense Sample of Helium Ions," Phys. Rev. Lett. **121**, 263201.
Haverkort, M. W., 2010, "Theory of Resonant Inelastic X-Ray Scattering by Collective Magnetic Excitations," Phys. Rev. Lett. **105**, 167404.
Haverkort, M. W., M. Zwierzycki, and O. K. Andersen, 2012, "Multiplet ligand-field theory using Wannier orbitals," Phys. Rev. B **85**, 165113.
Head-Gordon, T., and M. E. Johnson, 2006, "Tetrahedral structure or chains for liquid water," Proc. Natl. Acad. Sci. U.S.A. **103**, 7973.
Henneberger, W. C., 1968, "Perturbation Method for Atoms in Intense Light Beams," Phys. Rev. Lett. **21**, 838–841.
Hennies, F., *et al.*, 2005, "Nonadiabatic Effects in Resonant Inelastic X-Ray Scattering," Phys. Rev. Lett. **95**, 163002.
Hennies, F., *et al.*, 2007, "Dynamic interpretation of resonant x-ray Raman scattering: Ethylene and benzene," Phys. Rev. A **76**, 032505.
Hermanns, M., I. Kimchi, and J. Knolle, 2018, "Physics of the Kitaev model: Fractionalization, dynamic correlations, and material connections," Annu. Rev. Condens. Matter Phys. **9**, 17–33.
Hikosaka, Y., Y. Velkov, E. Shigemasa, T. Kaneyasu, Y. Tamenori, J. Liu, and F. Gel'mukhanov, 2008, "X-Ray Absorption Measured in the Resonant Auger Scattering Mode," Phys. Rev. Lett. **101**, 073001.
Hopersky, A. N., A. M. Nadolinsky, and S. A. Novikov, 2018, "Resonant inelastic scattering of two x-ray photons by a many-electron atom," Phys. Rev. A **98**, 063424.
Huang, X-C., X.-J. Kong, T.-J. Li, Z.-R. Ma, H.-C. Wang, G.-C. Liu, Z.-S. Wang, W.-B. Li, and L.-F. Zhu, 2021, "Controlling core-hole lifetime through an x-ray planar cavity," arXiv:2101.11225v1.
Humphries, O. S., *et al.*, 2020, "Mapping the electronic structure of warm dense nickel via resonant inelastic x-ray scattering," arXiv:2001.05813v1.
Hunault, M. O. J. Y., Y. Harada, J. Miyawaki, J. Wang, A. Meijerink, F. M. F. de Groot, and M. M. van Schooneveld, 2018, "Direct observation of Cr^{3+} 3*d* states in ruby: Toward experimental mechanistic evidence of metal chemistry, J. Phys. Chem. A **122**, 4399–4413.
Iga, F., *et al.*, 2004, "Determination of the Orbital Polarization in $YTiO_3$ by Using Soft X-Ray Linear Dichroism," Phys. Rev. Lett. **93**, 257207.
Ignatova, N., *et al.*, 2017a, "Infrared-pump-x-ray-probe spectroscopy of vibrationally excited molecules," Phys. Rev. A **95**, 042502.
Ignatova, N., *et al.*, 2017b, "Gradual collapse of nuclear wave functions regulated by frequency tuned x-ray scattering," Sci. Rep. **7**, 43891.
Ishihara, S., 2017, "Resonant x-ray scattering and orbital degree of freedom in correlated electron systems," in *Resonant X-Ray Scattering in Correlated Systems*, edited by Y. Murakami and S. Ishihara (Springer-Verlag, Heidelberg), pp. 1–46.
Ishii, K., 2017, "Resonant inelastic x-ray scattering in strongly correlated copper oxydes," in *Resonant X-Ray Scattering in Correlated Systems*, edited by Y. Murakami and S. Ishihara (Springer-Verlag, Heidelberg), pp. 197–241.
Ishii, K., I. Jarrige, M. Yoshida, K. Ikeuchi, T. Inami, Y. Murakami, and J. Mizuki, 2013, "Instrumental upgrades of the RIXS spectrometer at BL11XU at SPring-8," J. Electron Spectrosc. Relat. Phenom. **188**, 127–132.
Ishikawa, T., 2019, "Accelerator-based x-ray sources: Synchrotron radiation, x-ray free electron lasers and beyond," Phil. Trans. R. Soc. A **377**, 0231.
Ismail, I., M. Simon, and Francis Penent, 2020, MOSARIX: Progress report, arXiv:2003.05177.
Jackeli, G., and G. Khaliullin, 2009, "Mott Insulators in the Strong Spin-Orbit Coupling Limit: From Heisenberg to a Quantum Compass and Kitaev Models," Phys. Rev. Lett. **102**, 017205.
Jaeschke, E. J., S. Khan, J. R. Schneider, and J. B. Hastings, 2020, Eds., *Synchrotron Light Sources and Free-Electron Lasers: Accelerator Physics, Instrumentation and Science Applications*, 2nd ed. (Springer International Publishing, Cham, Switzerland).
Jang, H., *et al.*, 2016, "Ideal charge-density-wave order in the high-field state of superconducting YBCO," Proc. Natl. Acad. Sci. U.S.A. **113**, 14645–14650.
Jarrige, I., V. Bisogni, W. Leonhardt, and J. Dvorak, 2018, "Paving the way to ultra-high-resolution resonant inelastic x-ray scattering with the SIX beamline at NSLS-II," Synchrotron Radiat. News **31**, 7.
Jay, R. M., *et al.*, 2018, "Disentangling transient charge density and metal-ligand covalency in photoexcited ferricyanide with femtosecond resonant inelastic soft x-ray scattering, J. Phys. Chem. Lett. **9**, 3538–3543.
Jérome, D., and H. J. Schulz, 1982, "Organic conductors and superconductors, Adv. Phys. **31**, 299–490.
Jeyachandran, Y. L., *et al.*, 2014, "Ion-solvation-induced molecular reorganization in liquid water probed by resonant inelastic soft x-ray scattering, J. Phys. Chem. Lett. **5**, 4143–4148.
Johnson, A. S., *et al.*, 2018, "High-flux soft x-ray harmonic generation from ionization-shaped few-cycle laser pulses," Sci. Adv. **4**, eaar3761.
Jonker, G. H., 1966, "Magnetic and semiconducting properties of perovskites containing manganese and cobalt," J. Appl. Phys. **37**, 1424.
Josefsson, I., K. Kunnus, S. Schreck, A. Föhlisch, F. de Groot, Ph. Wernet, and M. Odelius, 2012, "*Ab initio* calculations of x-ray spectra: Atomic multiplet and molecular orbital effects in a multiconfigurational SCF approach to the *L*-edge spectra of transition metal complexes," J. Phys. Chem. Lett. **3**, 3565–3570.
Juhin, A., C. Brouder, and F. de Groot, 2014, "Angular dependence of resonant inelastic x-ray scattering: A spherical tensor expansion," Cent. Eur. J. Phys. **12**, 323–340.
Kanász-Nagy, M., Y. Shi, I. Klich, and E. A. Demler, 2016, "Resonant inelastic x-ray scattering as a probe of band structure effects in cuprates," Phys. Rev. B **94**, 165127.
Kane, P. P., 1992, "Inelastic scattering of x-rays and gamma rays by inner shell electrons," Phys. Rep. **218**, 67.
Kassi, S., P. Macko, O. Naumenko, and A. Campargue, 2005, "The absorption spectrum of water near 750 nm by CW-CRDS: Contribution to the search of water dimer absorption," Phys. Chem. Chem. Phys. **7**, 2460–2467.
Kazantsev, A. P., G. I. Surdutovich, and V. P. Yakovlev, 1990, *Mechanical Action of Light on Atoms* (World Scientific, Singapore).
Khalil, M., and S. Mukamel, 2020, "Ultrafast spectroscopy and diffraction from XUV to x-ray," J. Chem. Phys. **153**, 100401.
Khaliullin, G., and V. Oudovenko, 1997, "Spin and orbital excitation spectrum in the Kugel-Khomskii model," Phys. Rev. B **56**, R14243–14246.
Kikas, A., T. Käämbre, A. Saar, K. Kooser, E. Nõmmiste, I. Martinson, V. Kimberg, S. Polyutov, and F. Gel'mukhanov, 2004, "Resonant inelastic x-ray scattering at the F 1*s* photoabsorption edge in LiF:

Interplay of excitonic and conduction states, and Stokes' doubling," Phys. Rev. B **70**, 085102.
Kim, B. J., *et al.*, 2006, "Distinct spinon and holon dispersions in photoemission spectral functions from one-dimensional $SrCuO_2$," Nat. Phys. **2**, 397–401.
Kim, C., A. Y. Matsuura, Z.-X. Shen, N. Motoyama, H. Eisaki, S. Uchida, T. Tohyama, and S. Maekawa, 1996, "Observation of Spin-Charge Separation in One-Dimensional $SrCuO_2$," Phys. Rev. Lett. **77**, 4054–4057.
Kim, C., A. Y. Matsuura, Z.-X. Shen, N. Motoyama, H. Eisaki, S. Uchida, T. Tohyama, and S. Maekawa, 1997, "Separation of spin and charge excitations in one-dimensional $SrCuO_2$," Phys. Rev. B **56**, 15589–15595.
Kim, J., D. Casa, A. Said, R. Krakora, B. J. Kim, E. Kasman, X. Huang, and T. Gog, 2018, "Quartz-based flat-crystal resonant inelastic x-ray scattering spectrometer with sub-10 meV energy resolution," Sci. Rep. **8**, 1958.
Kim, J., *et al.*, 2012, "Magnetic Excitation Spectra of Sr_2IrO_4 Probed by Resonant Inelastic X-Ray Scattering: Establishing Links to Cuprate Superconductors," Phys. Rev. Lett. **108**, 177003.
Kim, K. H., *et al.*, 2017, "Maxima in the thermodynamic response and correlation functions of deeply supercooled water," Science **358**, 1589–1593.
Kim, K. H., *et al.*, 2020, "Experimental observation of the liquid-liquid transition in bulk supercooled water under pressure," Science **370**, 978–982.
Kim, K.-J., Y. Shvyd'ko, and S. Reiche, 2008, "A Proposal for an X-Ray Free-Electron Laser Oscillator with an Energy-Recovery Linac," Phys. Rev. Lett. **100**, 244802.
Kimberg, V., T. Gejo, M. Oura, T. Tokushima, Y. Horikawa, H. Arai, S. Shin, and N. Kosugi, 2012, "Rydberg-valence mixing and interchannel coupling in resonant oxygen 1*s* inelastic x-ray scattering of O_2," Phys. Rev. A **85**, 032503.
Kimberg, V., and C. Miron, 2014, "Molecular potentials and wave function mapping by high-resolution electron spectroscopy and *ab initio* calculations," J. Electron Spectrosc. Relat. Phenom. **195**, 301.
Kimberg, V., and N. Rohringer, 2013, "Amplified X-Ray Emission from Core-Ionized Diatomic Molecules," Phys. Rev. Lett. **110**, 043901.
Kimberg, V., and N. Rohringer, 2016, "Stochastic stimulated electronic x-ray Raman spectroscopy," Struct. Dyn. **3**, 034101.
Kimberg, V., *et al.*, 2016, "Stimulated x-ray Raman scattering—A critical assessment of the building block of nonlinear x-ray spectroscopy," Faraday Discuss. **194**, 305.
Kitaev, A., 2006, "Anyons in an exactly solved model and beyond," Ann. Phys. (Amsterdam) **321**, 2–111.
Kitajima, M., *et al.*, 2003, "Doppler Effect in Resonant Photoemission from SF_6: Correlation between Doppler Profile and Auger Emission Anisotropy," Phys. Rev. Lett. **91**, 213003.
Kjellsson, L., *et al.*, 2021, "Resonant inelastic x-ray scattering at the N_2 π^* resonance: Lifetime-vibrational interference, radiative electron rearrangement, and wave-function imaging," Phys. Rev. A **103**, 022812.
Kotani, A., and S. Shin, 2001, "Resonant inelastic x-ray scattering spectra for electrons in solids," Rev. Mod. Phys. **73**, 203–245.
Köuppel, H., W. Domcke, and L. S. Cederbaum, 2007, "Multimode molecular dynamics beyond the Born-Oppenheimer approximation," in *Advances in Chemical Physics LVII*, edited by I. Prigogin and S. A. Rice (John Wiley & Sons, New York), pp. 59–246.
Kowalewski, M., B. P. Fingerhut, K. E. Dorfman, K. Bennett, and S. Mukamel, 2017, "Simulating coherent multidimensional spectroscopy of nonadiabatic molecular processes: From the infrared to the x-ray regime," Chem. Rev. **117**, 12165–12226.
Kramers, H. A., and W. Heisenberg, 1925, "On the scattering of radiation off atoms," Z. Phys. **31**, 681–708.
Kraus, P. M., M. Zürch, S. K. Cushing, D. M. Neumark, and S. R. Leone, 2018, "The ultrafast x-ray spectroscopic revolution in chemical dynamics," Nat. Rev. Chem. **2**, 82–94.
Kringle, L., W. A. Thornley, B. D. Kay, and G. A. Kimmel, 2020, "Reversible structural transformations in supercooled liquid water from 135 to 245 K," Science **369**, 1490–1492.
Kroll, T., *et al.*, 2018, "Stimulated X-Ray Emission Spectroscopy in Transition Metal Complexes," Phys. Rev. Lett. **120**, 133203.
Kroll, T., *et al.*, 2020, "Observation of Seeded Mn Kβ Stimulated X-Ray Emission Using Two-Color X-Ray Free-Electron Laser Pulses," Phys. Rev. Lett. **125**, 037404.
Kugel', K. I., and D. I. Khomskii, 1982, "The Jahn-Teller effect and magnetism: Transition metal compounds," Sov. Phys. Usp. **25**, 231.
Kühne, T. D., and R. Z. Khaliullin, 2013, "Electronic signature of the instantaneous asymmetry in the first coordination shell of liquid water," Nat. Commun. **4**, 1450.
Kukk, E., *et al.*, 2018, "Energy Transfer into Molecular Vibrations and Rotations by Recoil in Inner-Shell Photoemission," Phys. Rev. Lett. **121**, 073002.
Kumar, M. P., *et al.*, 2020, "Attosecond pulse shaping using a seeded free-electron laser," Nature (London) **578**, 386–391.
Kumar, Umesh, Alberto Nocera, Elbio Dagotto, and Steve Johnston, 2018, "Multi-spinon and antiholon excitations probed by resonant inelastic x-ray scattering on doped one- dimensional antiferromagnets," New J. Phys. **20**, 073019.
Kunnus, K., *et al.*, 2016a, "Anti-Stokes resonant x-ray Raman scattering for atom specific and excited state selective dynamics," New J. Phys. **18**, 103011.
Kunnus, K., *et al.*, 2016b, "Viewing the valence electronic structure of ferric and ferrous hexacyanide in solution from the Fe and cyanide perspectives, J. Phys. Chem. B **120**, 7182–7194.
Lange, K. M., and E. F. Aziz, 2013, "Electronic structure of ions and molecules in solution: A view from modern soft x-ray spectroscopies," Chem. Soc. Rev. **42**, 6840.
Lange, K. M., R. Könnecke, M. Soldatov, R. Golnak, J.-E. Rubensson, A. Soldatov, and E. F. Aziz, 2011, "On the origin of the hydrogen-bond-network nature of water: X-ray absorption and emission spectra of water-acetonitrile mixtures," Angew. Chem., Int. Ed. Engl. **50**, 10621–10625.
Le Tacon, M., A. Bosak, S. M. Souliou, G. Dellea, T. Loew, R. Heid, K-P. Bohnen, G. Ghiringhelli, M. Krisch, and B. Keimer, 2014, "Inelastic x-ray scattering in $YBa_2Cu_3O_{6.6}$ reveals giant phonon anomalies and elastic central peak due to charge-density-wave formation," Nat. Phys. **10**, 52.
Li, J., *et al.*, 2020, "Multiorbital charge-density wave excitations and concomitant phonon anomalies in $Bi_2Sr_2LaCuO_{6+\delta}$," Proc. Natl. Acad. Sci. U.S.A. **117**, 16219.
Li, K., M. Labeye, P. J. Ho, M. B. Gaarde, and L. Young, 2020, "Resonant propagation of x-rays from the linear to the nonlinear regime," Phys. Rev. A **102**, 053113.
Lieb, E. H., and F. Y. Wu, 1968, "Absence of Mott Transition in an Exact Solution of the Short-Range, One-Band Model in One Dimension," Phys. Rev. Lett. **20**, 1445–1448.
Limmer, D. T., and D. Chandler, 2013, "The putative liquid-liquid transition is a liquid-solid transition in atomistic models of water. II," J. Chem. Phys. **138**, 214504.
Lindblad, A., J. Söderström, C. Nicolas, E. Robert, and C. Miron, 2013, "A multi purpose source chamber at the PLEIADES beamline at SOLEIL for spectroscopic studies of isolated species: Cold

molecules, clusters, and nanoparticles," Rev. Sci. Instrum. **84**, 113105.

Lindle, D. W., P. L. Cowan, T. Jach, R. E. LaVilla, R. D. Deslattes, and R. C. C. Perera, 1991, "Polarized x-ray emission studies of methyl chloride and the chlorofluoromethanes," Phys. Rev. A **43**, 2353.

Lindle, D. W., P. L. Cowan, R. E. LaVilla, T. Jach, R. D. Deslattes, B. Karlin, J. A. Sheehy, T. J. Gil, and P. W. Langhoff, 1988, "Polarization of Molecular X-Ray Fluorescence," Phys. Rev. Lett. **60**, 1010.

Liu, J.-C., C. Miron, H. Ågren, S. Polyutov, and F. Gel'mukhanov, 2019, "Resonant x-ray second-harmonic generation in atomic gases," Phys. Rev. A **100**, 063403.

Liu, J.-C., V. Savchenko, V. Kimberg, F. Gel'mukhanov, and M. Odelius, 2021, "High-resolution x-ray spectra of carbon monoxide reveal ultrafast dynamics induced by long UV pulse," New J. Phys. (in press), https://doi.org/10.1088/1367-2630/ac0198.

Liu, J.-C., V. Savchenko, V. Kimberg, M. Odelius, and F. Gel'mukhanov, 2021b, "Polarization-sensitive IR-pump-x-ray-probe spectroscopy," Phys. Rev. A **103**, 022829.

Liu, J.-C., Y.-P. Sun, C.-K. Wang, H. Ågren, and F. Gel'mukhanov, 2010, "Auger effect in the presence of strong x-ray pulses," Phys. Rev. A **81**, 043412.

Liu, J.-C., V. Vaz da Cruz, S. Polyutov, A. Föhlisch, and F. Gel'mukhanov, 2019, "Recoil-induced dissociation in hard-x-ray photoionization," Phys. Rev. A **100**, 053408.

Liu, J.-C., Y. Velkov, Z. Rinkevicius, H. Ågren, and F. Gel'mukhanov, 2008, "Symmetry-forbidden x-ray Raman scattering induced by strong infrared-laser pulse," Phys. Rev. A **77**, 043405.

Liu, J.-C., *et al.*, 2011a, "Multimode resonant auger scattering from the ethene molecule, J. Phys. Chem. B **115**, 5103–5112.

Liu, J.-C., *et al.*, 2011b, "Multimode resonant Auger scattering from the ethene molecule," J. Phys. Chem. B **115**, 5103.

Liu, X. J., *et al.*, 2005, "Site-selective ion production of the core-excited CH_3F molecule probed by Auger-electron-ion coincidence measurements," Phys. Rev. A **72**, 042704.

Liu, X.-J., Q. Miao, F. Gel'mukhanov, M. Patanen, O. Travnikova, C. Nicolas, H. Ågren, K. Ueda, and C. Miron, 2015, "Einstein-Bohr recoiling double-slit gedanken experiment performed at the molecular level," Nat. Photonics **9**, 120.

Liu, X.-J., C. Nicolas, and C. Miron, 2013, "Design of a lens table for a double toroidal electron spectrometer," Rev. Sci. Instrum. **84**, 033105.

Liu, X.-J., *et al.*, 2006, "Young's double-slit experiment using core-level photoemission from N_2: Revisiting Cohen-Fano's two-centre interference phenomenon," J. Phys. B **39**, 4801.

Ljungberg, M. P., I. Zhovtobriukh, O. Takahashi, and L. G. M. Pettersson, 2017, "Core-hole-induced dynamical effects in the x-ray emission spectrum of liquid methanol," J. Chem. Phys. **146**, 134506.

Lucchese, R. R., J. Söderström, T. Tanaka, M. Hoshino, M. Kitajima, H. Tanaka, A. De Fanis, J.-E. Rubensson, and K. Ueda, 2007, "Vibrationally resolved partial cross sections and asymmetry parameters for nitrogen *K*-shell photoionization of the N_2O molecule," Phys. Rev. A **76**, 012506.

Lundberg, M., and Ph. Wernet, 2019, "Resonant inelastic x-ray scattering (RIXS) studies in chemistry: Present and future," in *Synchrotron Light Sources and Free-Electron Lasers: Accelerator Physics, Instrumentation and Science Applications*, edited by E. Jaeschke, S. Khan, J. R. Schneider, and J. B. Hastings (Springer International Publishing, Cham, Switzerland), pp. 1–52.

Lüning, J., J.-E. Rubensson, C. Ellmers, S. Eisebitt, and W. Eberhardt, 1997, "Site- and symmetry-projected band structure measured by resonant inelastic soft x-ray scattering," Phys. Rev. B **56**, 13147.

Luo, Y., H. Ågren, F. Gel'mukhanov, J. Guo, P. Skytt, N. Wassdahl, and J. Nordgren, 1995, "Symmetry-selective resonant inelastic x-ray scattering of C_{60}," Phys. Rev. B **52**, 14479.

Luo, Y., O. Vahtras, F. Gel'mukhanov, and H. Ågren, 1997, "Theory of natural circular dichroism in x-ray Raman scattering from molecules," Phys. Rev. A **55**, 2716.

Luttinger, J. M., 1963, "An exactly soluble model of a many-fermion system," J. Math. Phys. (N.Y.) **4**, 1154–1162.

Maganas, D., P. Kristiansen, L.-C. Duda, A. Knop-Gericke, S. DeBeer, R. Schlögl, and F. Neese, 2014, "Combined experimental and *ab initio* multireference configuration interaction study of the resonant inelastic x-ray scattering spectrum of CO_2, J. Phys. Chem. C **118**, 20163–20175.

Magnuson, M., S. M. Butorin, A. Agui, and J. Nordgren, 2002, "Resonant soft x-ray Raman scattering of NiO," J. Phys. Condens. Matter **14**, 3669.

Magnuson, M., S. M. Butorin, J.-H. Guo, and J. Nordgren, 2002, "Electronic structure investigation of CoO by means of soft x-ray scattering," Phys. Rev. B **65**, 205106.

Magnuson, M., L.-C. Duda, S. M. Butorin, P. Kuiper, and J. Nordgren, 2006, "Large magnetic circular dichroism in resonant inelastic x-ray scattering at the Mn *L*-edge of Mn-Zn ferrite," Phys. Rev. B **74**, 172409.

Magnuson, M., J.-E. Rubensson, A. Föhlisch, N. Wassdahl, A. Nilsson, and N. Mårtensson, 2003, "X-ray fluorescence spectra of metals excited below threshold," Phys. Rev. B **68**, 045119.

Marchenko, T., *et al.*, 2011, "Resonant inelastic x-ray scattering at the limit of subfemtosecond natural lifetime," J. Chem. Phys. **134**, 144308.

Marchenko, T., *et al.*, 2015, "Electron Dynamics in the Core-Excited CS_2 Molecule Revealed through Resonant Inelastic X-Ray Scattering Spectroscopy," Phys. Rev. X **5**, 031021.

Marchenko, T., *et al.*, 2017, "Potential Energy Surface Reconstruction and Lifetime Determination of Molecular Double-Core-Hole States in the Hard X-Ray Regime," Phys. Rev. Lett. **119**, 133001.

Matthews, M., *et al.*, 2018, "Amplification of intense light fields by nearly free electrons," Nat. Phys. **14**, 695–700.

Mattis, D. C., and E. H. Lieb, 1965, "Exact solution of a many-fermion system and its associated boson field," J. Math. Phys. (N.Y.) **6**, 304–312.

Mayer, R., D. W. Lindle, S. H. Southworth, and P. L. Cowan, 1991, "Direct determination of molecular orbital symmetry of H_2S using polarized x-ray emission," Phys. Rev. A **43**, 235.

McCall, S. L., and E. L. Hahn, 1967, "Self-Induced Transparency by Pulsed Coherent Light," Phys. Rev. Lett. **18**, 908.

Menshikov, L. I., P. L. Menshikov, and P. O. Fedichev, 2020, "Effects of action at a distance in water," Phys. Usp. **63**, 440.

Mercadier, L., *et al.*, 2019, "Evidence of Extreme Ultraviolet Superfluorescence in Xenon," Phys. Rev. Lett. **123**, 023201.

Miao, Q., J.-C. Liu, H. Ågren, J.-E. Rubensson, and F. Gel'mukhanov, 2012, "Dissociative X-Ray Lasing," Phys. Rev. Lett. **109**, 233905.

Miao, Q., O. Travnikova, F. Gel'mukhanov, V. Kimberg, Y.-P. Sun, T. D. Thomas, C. Nicolas, M. Patanen, and C. Miron, 2015, "Rotational Doppler effect: A probe for molecular orbital anisotropy, J. Phys. Chem. Lett. **6**, 1568–1572.

Miedema, P. S., M. Beye, R. Könnecke, G. Schiwietz, and A. Föhlisch, 2014, "The angular- and crystal-momentum transfer through electron-phonon coupling in silicon and silicon- carbide: Similarities and differences," New J. Phys. **16**, 093056.

Millot, M., S. Hamel, J. Ryan Rygg, P. M. Celliers, G. W. Collins, F. Coppari, D. E. Fratanduono, R. Jeanloz, D. C. Swift, and J. H. Eggert, 2018, "Experimental evidence for superionic water ice using shock compression," Nat. Phys. **14**, 297–302.

Mills, D., J. A. Sheehy, T. A. Ferrett, S. H. Southworth, R. Mayer, D. W. Lindle, and P. W. Langhoff, 1997, "Nondipole Resonant X-Ray Raman Spectroscopy: Polarized Inelastic Scattering at the *K* Edge of Cl_2," Phys. Rev. Lett. **79**, 383.

Miron, C., V. Kimberg, P. Morin, C. Nicolas, N. Kosugi, S. Gavrilyuk, and F. Gel'mukhanov, 2010, "Vibrational Scattering Anisotropy Generated by Multichannel Quantum Interference," Phys. Rev. Lett. **105**, 093002.

Miron, C., Q. Miao, C. Nicolas, J. D. Bozek, W. Andrałojć, M. Patanen, G. Simões, O. Travnikova, H. Å gren, and F. Gel'mukhanov, 2014, "Site-selective photoemission from delocalized valence shells induced by molecular rotation," Nat. Commun. **5**, 3816.

Miron, C., C. Nicolas, O. Travnikova, P. Morin, Y.-P. Sun, F. Gel'mukhanov, N. Kosugi, and V. Kimberg, 2012, "Imaging molecular potentials using ultrahigh-resolution resonant photoemission," Nat. Phys. **8**, 135.

Mitrano, Matteo, *et al.*, 2019a, "Ultrafast time-resolved x-ray scattering reveals diffusive charge order dynamics in $La_{2-x}Ba_xCuO_4$," Sci. Adv. **5**, eaax3346.

Mitrano, Matteo, *et al.*, 2019b, "Evidence for photoinduced sliding of the charge-order condensate in $La_{1.875}Ba_{0.125}CuO_4$," Phys. Rev. B **100**, 205125.

Miyawaki, J., S. Suga, H. Fujiwara, M. Urasaki, H. Ikeno, H. Niwa, H. Kiuchi, and Y. Harada, 2017, "Dzyaloshinskii-Moriya interaction in αFe_2O_3 measured by magnetic circular dichroism in resonant inelastic soft x-ray scattering," Phys. Rev. B **96**, 214420.

Mizokawa, T., D. I. Khomskii, and G. A. Sawatzky, 1999, "Interplay between orbital ordering and lattice distortions in $LaMnO_3$, YVO_3, and $YTiO_3$," Phys. Rev. B **60**, 7309.

Morin, P., and I. Nenner, 1986, "Atomic Autoionization Following Very Fast Dissociation of Core-Excited HBr," Phys. Rev. Lett. **56**, 1913.

Mukamel, S., 2005, "Multiple core-hole coherence in x-ray four-wave-mixing spectroscopies," Phys. Rev. B **72**, 235110.

Murakami, Y., H. Kawada, H. Kawata, M. Tanaka, T. Arima, Y. Moritomo, and Y. Tokura, 1998, "Direct Observation of Charge and Orbital Ordering in $La_{0.5}Sr_{1.5}MnO_4$," Phys. Rev. Lett. **80**, 1932–1935.

Murakami, Y., H. Nakao, T. Matsumura, and H. Ohsumi, 2007, "Mechanism of resonant x-ray scattering to observe the orbital ordering," J. Magn. Magn. Mater. **310**, 723–729.

Murakami, Y., *et al.*, 1998, "Resonant X-Ray Scattering from Orbital Ordering in $LaMnO_3$," Phys. Rev. Lett. **81**, 582–585.

Nag, A., *et al.*, 2020, "Many-Body Physics of Single and Double Spin-Flip Excitations in NiO," Phys. Rev. Lett. **124**, 067202.

Nagasaka, Masanari, Hayato Yuzawa, and Nobuhiro Kosugi, 2020, "Soft x-ray absorption spectroscopy of liquids for understanding chemical processes in solution," Anal. Sci. **36**, 95–105.

Nandi, S., C. Nicolas, A. N. Artemyev, N. M. Novikovskiy, C. Miron, J. D. Bozek, and Ph. V. Demekhin, 2017, "Electronic-state interference in the C 1*s* excitation and decay of methyl chloride studied by angularly resolved Auger spectroscopy," Phys. Rev. A **96**, 052501.

Naus, H., W. Ubachs, P. F. Levelt, O. L. Polyansky, N. F. Zobov, and J. Tennyson, 2001, "Cavity-ring-down spectroscopy on water vapor in the range 555–604 nm," J. Mol. Spectrosc. **205**, 117–121.

Nazarkin, A., S. Podorov, I. Uschmann, E. Förster, and R. Sauerbrey, 2003, "Nonlinear optics in the angstrom regime: Hard-x-ray frequency doubling in perfect crystals," Phys. Rev. A **67**, 041804R.

Neeb, M., J.-E. Rubensson, M. Biermann, and W. Eberhardt, 1994, "Coherent excitation of vibrational wave functions observed in core hole decay spectra of O_2, N_2 and CO," J. Electron Spectrosc. Relat. Phenom. **67**, 261.

Nicoletti, D., E. Casandruc, Y. Laplace, V. Khanna, C. R. Hunt, S. Kaiser, S. S. Dhesi, G. D. Gu, J. P. Hill, and A. Cavalleri, 2014, "Optically induced superconductivity in striped $La_{2-x}Ba_xCuO_4$ by polarization-selective excitation in the near infrared," Phys. Rev. B **90**, 100503(R).

Nilsson, A., and L. G. M. Pettersson, 2011, "Perspective on the structure of liquid water, Chem. Phys. **389**, 1–34.

Nilsson, A., and L. G. M. Pettersson, 2015, "The structural origin of anomalous properties of liquid water," Nat. Commun. **6**, 8998.

Nilsson, A., T. Tokushima, Y. Horikawa, Y. Harada, M. P. Ljungberg, S. Shin, and L. G. M. Pettersson, 2013, "Resonant inelastic x-ray scattering of liquid water," J. Electron Spectrosc. Relat. Phenom. **188**, 84–100.

Nishizawa, K., N. Kurahashi, K. Sekiguchi, T. Mizuno, Y. Ogi, T. Horio, M. Oura, N. Kosugia, and T. Suzuki, 2011, "High-resolution soft x-ray photoelectron spectroscopy of liquid water," Phys. Chem. Chem. Phys. **13**, 413–417.

Niskanen, J., *et al.*, 2019, "Compatibility of quantitative x-ray spectroscopy with continuous distribution models of water at ambient conditions," Proc. Natl. Acad. Sci. U.S.A. **116**, 4058.

Nordgren, Joseph, and Jan-Erik Rubensson, 2013, "Resonant soft x-ray emission for studies of molecules and solids," J. Electron Spectrosc. Relat. Phenom. **188**, 3–9.

Norell, J., R. M. Jay, M. Hantschmann, S. Eckert, M. Guo, K. J. Gaffney, Ph. Wernet, M. Lundberg, A. Föhlisch, and M. Odelius, 2018, "Fingerprints of electronic, spin and structural dynamics from resonant inelastic soft x-ray scattering in transient photochemical species," Phys. Chem. Chem. Phys. **20**, 7243–7253.

Norman, P., and A. Dreuw, 2018, "Simulating x-ray spectroscopies and calculating core-excited states of molecules," Chem. Rev. **118**, 7208–7248.

Noziéres, P., and E. Abrahams, 1974, "Threshold singularities of the x-ray Raman scattering in metals," Phys. Rev. B **10**, 3099.

Odelius, M., 2009a, "Information content in O[1*s*] *K*-edge x-ray emission spectroscopy of liquid water, J. Phys. Chem. A **113**, 8176–8181.

Odelius, M., 2009b, "Molecular dynamics simulations of fine structure in oxygen *K*-edge x-ray emission spectra of liquid water and ice," Phys. Rev. B **79**, 144204.

Odelius, M., *et al.*, 2005, "Ultrafast Core Hole Induced Dynamics in Water Probed by X-Ray Emission Spectroscopy," Phys. Rev. Lett. **94**, 227401.

Olalde-Velasco, P., J. Jiménez-Mier, J. D. Denlinger, Z. Hussain, and W. L. Yang, 2011, "Direct probe of Mott-Hubbard to charge-transfer insulator transition and electronic structure evolution in transition-metal systems," Phys. Rev. B **83**, 241102(R).

Palmer, J. C., R. Car, and P. G. Debenedetti, 2013, "The liquid-liquid transition in supercooled ST2 water: A comparison between umbrella sampling and well-tempered metadynamics," Faraday Discuss. **167**, 77.

Palmer, J. C., P. H. Poole, F. Sciortino, and P. G. Debenedetti, 2018, "Advances in computational studies of the liquid-liquid transition in water and water-like models," Chem. Rev. **118**, 9129–9151.

Pellegrini, C., A. Marinelli, and S. Reiche, 2016, "The physics of x-ray free-electron lasers," Rev. Mod. Phys. **88**, 015006.

Perakis, F., L. De Marco, A. Shalit, F. Tang, Z. R. Kann, T. D. Künne, R. Torre, M. Bonn, and Y. Nagata, 2016, "Vibrational spectroscopy and dynamics of water," Chem. Rev. **116**, 7590–7607.

Petrillo, V., *et al.*, 2020, "Coherent, high repetition rate tender x-ray free-electron laser seeded by an extreme ultra-violet free-electron laser oscillator," New J. Phys. **22**, 073058.

Piancastelli, M.-N., T. Marchenko, R. Guillemin, L. Journel, O. Travnikova, I. Ismail, and M. Simon, 2020, "Hard x-ray spectroscopy and dynamics of isolated atoms and molecules: A review," Rep. Prog. Phys. **83**, 016401.

Picón, A., *et al.*, 2016, "Hetero-site-specific x-ray pump-probe spectroscopy for femtosecond intramolecular dynamics," Nat. Commun. **7**, 11652.

Pietzsch, A., F. Hennies, P. S. Miedema, B. Kennedy, J. Schlappa, T. Schmitt, V. N. Strocov, and A. Föhlisch, 2015, "Snapshots of the Fluctuating Hydrogen Bond Network in Liquid Water on the Sub-Femtosecond Timescale with Vibrational Resonant Inelastic X-Ray Scattering," Phys. Rev. Lett. **114**, 088302.

Pietzsch, A., *et al.*, 2011, "Spatial Quantum Beats in Vibrational Resonant Inelastic Soft X-Ray Scattering at Dissociating States in Oxygen," Phys. Rev. Lett. **106**, 153004.

Pinjari, R. V., M. G. Delcey, M. Guo, M. Odelius, and M. Lundberg, 2014, "Restricted active space calculations of L-edge x-ray absorption spectra: From molecular orbitals to multiplet states," J. Chem. Phys. **141**, 124116.

Polyansky, Oleg L., Roman I. Ovsyannikov, Aleksandra A. Kyuberis, Lorenzo Lodi, Jonathan Tennyson, and Nikolai F. Zobov, 2013, "Calculation of rotation-vibration energy levels of the water molecule with near-experimental accuracy based on an *ab initio* potential energy surface, J. Phys. Chem. A **117**, 9633–9643.

Pontius, N., *et al.*, 2018, "Probing the non-equilibrium transient state in magnetite by a jitter-free two-color x-ray pump and x-ray probe experiment," Struct. Dyn. **5**, 054501.

Popova, T. Ya., A. K. Popov, S. G. Raurtian, and R. I. Sokolovskii, 1970, "Nonlinear interference effects in emission, absorption, and generation spectra," Sov. Phys. JETP **30**, 466–472, http://jetp.ac.ru/cgi-bin/dn/e_030_03_0466.pdf.

Privalov, T., F. Gel'mukhanov, and H. Ågren, 1999, "Role of electron-phonon interaction in resonant x-ray Raman scattering by polymers and solids," Phys. Rev. B **59**, 9243.

Privalov, T., F. Gel'mukhanov, and H. Ågren, 2001, "X-ray Raman scattering from molecules and solids in the framework of the Mahan–Noziéres–De Dominicis model," Phys. Rev. B **64**, 165116.

Puglisi, A., P. Selles, N. Sisourat, and S. Carniato, 2020, "L-edge photoelectron spectra of silicon hydride cations: Imprint of molecular-field and spin-orbit effects," Phys. Rev. A **102**, 042801.

Revelli, A., *et al.*, 2019, "Resonant inelastic x-ray incarnation of Young's double-slit experiment," Sci. Adv. **5**, eaav4020.

Robin, M., I. Ishii, R. McLaren, and A. Hitchcock, 1988, "Fluorination effects on the inner-shell spectra of unsaturated molecules," J. Electron Spectrosc. Relat. Phenom. **47**, 53.

Rohringer, N., and R. Santra, 2008, "Resonant Auger effect at high x-ray intensity," Phys. Rev. A **77**, 053404.

Rohringer, N., *et al.*, 2012, "Atomic inner-shell x-ray laser at 1.46 nanometres pumped by an x-ray free-electron laser," Nature (London) **481**, 488.

Röntgen, W. K., 1892, "Ueber die constitution des flüssigen wassers," Ann. Phys. (Berlin) **281**, 91–97.

Rosenqvist, L., *et al.*, 2001, "Femtosecond dissociation of ozone studied by the Auger Doppler effect," J. Chem. Phys. **115**, 3614.

Rossbach, J., J. R. Schneider, and W. Wurth, 2019, "10 years of pioneering x-ray science at the free-electron laser FLASH at DESY," Phys. Rep. **808**, 1–74.

Rossi, M., *et al.*, 2019a, "Experimental Determination of Momentum-Resolved Electron-Phonon Coupling," Phys. Rev. Lett. **123**, 027001.

Rossi, M., *et al.*, 2019b, "Resonant inelastic x-ray scattering of magnetic excitations under pressure," J. Synchrotron Radiat. **26**, 1725–1732.

Rubensson, J.-E., 2000, "RIXS dynamics for beginners," J. Electron Spectrosc. Relat. Phenom. **110-111**, 135–151.

Rueff, J.-P., and A. Shukla, 2010, "Inelastic x-ray scattering by electronic excitations under high pressure," Rev. Mod. Phys. **82**, 847–896.

Russo, J., and H. Tanaka, 2014, "Understanding water's anomalies with locally favoured structures," Nat. Commun. **5**, 3556.

Safonova, O. V., M. Tromp, J. A. van Bokhoven, F. M. F. de Groot, J. Evans, and P. Glatzel, 2006, "Identification of CO adsorption sites in supported Pt catalysts using high-energy-resolution fluorescence detection x-ray spectroscopy, J. Phys. Chem. B **110**, 16162–16164.

Sala, M. M., *et al.*, 2018, "A high-energy-resolution resonant inelastic x-ray scattering spectrometer at ID20 of the European Synchrotron Radiation Facility," J. Synchrotron Radiat. **25**, 580–591.

Salamon, M. B., and M. Jaime, 2001, "The physics of manganites: Structure and transport," Rev. Mod. Phys. **73**, 583–628.

Sałek, P., F. Gel'mukhanov, and H. Ågren, 1999, "Wave-packet dynamics of resonant x-ray Raman scattering: Excitation near the Cl $L_{II,III}$ edge of HCl," Phys. Rev. A **59**, 1147.

Sałek, P., *et al.*, 2001, "Dynamical suppression of atomic peaks in resonant dissociative photoemission," Chem. Phys. Lett. **343**, 332.

Såthe, C., F. F. Guimarães, J.-E. Rubensson, J. Nordgren, A. Agui, J. Guo, U. Ekström, P. Norman, F. Gel'mukhanov, and H. Ågren, 2006, "Resonant $L_{II,III}$ x-ray Raman scattering from HCl," Phys. Rev. A **74**, 062512.

Savchenko, V., *et al.*, 2021, "Vibrational resonant inelastic x-ray scattering inliquid acetic acid: A ruler for molecular chain lengths," Sci. Rep. **11**, 4098.

Schinke, R., 2009, *Photodissociation Dynamics* (Cambridge University Press, Cambridge, England).

Schlappa, J., *et al.*, 2012, "Spin-orbital separation in the quasi-one-dimensional Mott insulator Sr_2CuO_3," Nature (London) **485**, 82–85.

Schlappa, J., *et al.*, 2018, "Probing multi-spinon excitations outside of the two-spinon continuum in the antiferromagnetic spin chain cuprate Sr_2CuO_3," Nat. Commun. **9**, 5394.

Schmitt, T., F. M. F. de Groot, and J.-E. Rubensson, 2014, "Prospects of high-resolution resonant x-ray inelastic scattering studies on solid materials, liquids and gases at diffraction-limited storage rings," J. Synchrotron Radiat. **21**, 1065–1076.

Schmitt, T., V. N. Strocov, K.-J. Zhou, J. Schlappa, C. Money, U. Flechsig, and L. Patthey, 2013, "High-resolution resonant inelastic x-ray scattering with soft x-rays at the ADRESS beamline of the Swiss light source: Instrumental developments and scientific highlight," J. Electron Spectrosc. Relat. Phenom. **188**, 38–46.

Schoenlein, R., T. Elsaesser, K. Holldack, Z. Huang, H. Kapteyn, M. Murnane, and M. Woerner, 2019, "Recent advances in ultrafast x-ray sources," Phil. Trans. R. Soc. A **377**, 20180384.

Schreck, S., A. Pietzsch, K. Kunnus, B. Kennedy, W. Quevedo, P. S. Miedema, P. Wernet, and A. Föhlisch, 2014, "Dynamics of the OH group and electronic structure of liquid alcohols," Struct. Dyn. **1**, 054901.

Schreck, S., *et al.*, 2016, "Ground state potential energy surfaces around selected atoms from resonant inelastic x-ray scattering," Sci. Rep. **6**, 20054.

Schülke, W., 2007, *Electron Dynamics by Inelastic X-Ray Scattering* (Oxford University Press, Oxford).

Schweigert, I., and S. Mukamel, 2007, "Probing valence electronic wave-packet dynamics by all x-ray stimulated Raman spectroscopy: A simulation study," Phys. Rev. A **76**, 012504.

Shi, R., and H. Tanaka, 2020, "Direct evidence in the scattering function for the coexistence of two types of local structures in liquid water, J. Am. Chem. Soc. **142**, 2868–2875.

Shia, R., J. Russo, and H. Tanaka, 2018, "Origin of the emergent fragile-to-strong transition in supercooled water, Proc. Natl. Acad. Sci. U.S.A. **115**, 9444–9449.

Shin, S., A. Agui, M. Watanabe, M. Fujisawa, Y. Tezuka, and T. Ishii, 1996, "Observation of resonant Raman scattering at the Si $L_{2,3}$ core exciton," Phys. Rev. B **53**, 15660.

Shirley, E. L., 2000, "Theory and simulation of resonant inelastic x-ray scattering in s-p bonded systems: Graphite, hexagonal boron nitride, diamond, and cubic boron nitride," J. Electron Spectrosc. Relat. Phenom. **110–111**, 305–321.

Shvyd'ko, Y., 2019, "Output coupling from x-ray free-electron laser cavities with intracavity beam splitters," Phys. Rev. Accel. Beams **22**, 100703.

Shvyd'ko, Y., S. Stoupin, K. Mundboth, and J. Kim, 2013, "Hard x-ray spectrographs with resolution beyond 100 μeV," Phys. Rev. A **87**, 043835.

Shwartz, S., *et al.*, 2014, "X-Ray Second Harmonic Generation," Phys. Rev. Lett. **112**, 163901.

Simon, M., and T. Schmitt, 2013, "Progress in resonant inelastic x-ray scattering," J. Electron Spectrosc. Relat. Phenom. **188**, 1–2.

Simon, M., *et al.*, 2006, "Femtosecond nuclear motion of HCl probed by resonant x-ray Raman scattering in the Cl 1s region," Phys. Rev. A **73**, 020706(R).

Simon, M., *et al.*, 2014, "Atomic Auger Doppler effects upon emission of fast photoelectrons," Nat. Commun. **5**, 4069.

Sivia, D. S., 2011, *Elementary Scattering Theory: For X-Ray and Neutron Users*, 1st ed. (Oxford University Press, Oxford).

Skytt, P., P. Glans, K. Gunnelin, J. Guo, and J. Nordgren, 1997, "Lifetime-vibrational interference effects in the resonantly excited x-ray-emission spectra of CO," Phys. Rev. A **55**, 146.

Skytt, P., P. Glans, J.-H. Guo, K. Gunnelin, C. Såthe, J. Nordgren, F. Kh. Gel'mukhanov, A. Cesar, and H. Ågren, 1996, "Quenching of Symmetry Breaking in Resonant Inelastic X-Ray Scattering by Detuned Excitation," Phys. Rev. Lett. **77**, 5035.

Smallenburg, F., and F. Sciortino, 2015, "Tuning the Liquid-Liquid Transition by Modulating the Hydrogen-Bond Angular Flexibility in a Model for Water," Phys. Rev. Lett. **115**, 015701.

Söderström, J., *et al.*, 2020, "Resonant inelastic x-ray scattering on CO_2: Parity conservation in inversion-symmetric polyatomics," Phys. Rev. A **101**, 062501.

Soper, A. K., 2019, "Is water one liquid or two?" J. Chem. Phys. **150**, 234503.

Soper, A. K., and M. A. Ricci, 2000, "Structures of High-Density and Low-Density Water," Phys. Rev. Lett. **84**, 2881–2884.

Soper, A. K., J. Teixeira, and T. Head-Gordon, 2010, "Is ambient water inhomogeneous on the nanometer-length scale?," Proc. Natl. Acad. Sci. U.S.A. **107**, E44.

Sorensen, L., *et al.*, 2007, "Electronic Doppler effect in resonant Auger decay of CO molecules upon excitation near a shake-up Π resonance," Phys. Rev. A **76**, 062704.

Southworth, S. H., 1994, "Resonance and threshold effects in polarized x-ray emission from atoms and molecules," Nucl. Instrum. Methods Phys. Res., Sect. B **87**, 247–252.

Southworth, S. H., D. W. Lindle, R. Mayer, and P. L. Cowan, 1991, "Anisotropy of Polarized X-Ray Emission from Molecules," Phys. Rev. Lett. **67**, 1098.

Spielberger, L., *et al.*, 1995, "Separation of Photoabsorption and Compton Scattering Contributions to He Single and Double Ionization," Phys. Rev. Lett. **74**, 4615–4618.

Stillinger, F. H., 1980, "Water revisited," Science **209**, 451–457.

Stöhr, J., 1992, *NEXAFS Spectroscopy*, Springer Series in Surface Sciences (Springer, New York).

Streltsov, S. V., and D. I. Khomskii, 2017, "Orbital physics in transition metal compounds: New trends," Phys. Usp. **60**, 1121–1146.

Suga, S., *et al.*, 2009, "Do all nuclei recoil on photoemission in compounds?," New J. Phys. **11**, 073025.

Sun, Y.-P., J.-C. Liu, and F. Gel'mukhanov, 2009a, "The propagation of a strong x-ray pulse followed by pulse slowdown and compression, amplified spontaneous emission and lasing without inversion," J. Phys. B **42**, 201001.

Sun, Y.-P., J.-C. Liu, and F. Gel'mukhanov, 2009b, "Slowdown and compression of a strong x-ray free-electron pulse propagating through the Mg vapors," Europhys. Lett. **87**, 64002.

Sun, Y.-P., J.-C. Liu, C.-K. Wang, and F. Gel'mukhanov, 2010, "Propagation of a strong x-ray pulse: Pulse compression, stimulated Raman scattering, amplified spontaneous emission, lasing without inversion, and four-wave mixing," Phys. Rev. A **81**, 013812.

Sun, Y.-P., Q. Miao, A.-P. Zhou, R.-J. Liu, B. Liu, and F. Gel'mukhanov, 2018, "Suppression of resonant Auger effect with chirped x-ray free-electron laser pulse," J. Phys. B **51**, 035602.

Sun, Y.-P., A. Pietzsch, F. Hennies, Z. Rinkevicius, H. O. Karlsson, T. Schmitt, V. N. Strocov, J. Andersson, B. Kennedy, and J. Schlappa, 2011, "Internal symmetry and selection rules in resonant inelastic soft x-ray scattering," J. Phys. B **44**, 161002.

Sun, Y.-P., Z. Rinkevicius, C.-K. Wang, S. Carniato, M. Simon, R. Taïeb, and F. Gel'mukhanov, 2010, "Two-photon-induced x-ray emission in neon atoms," Phys. Rev. A **82**, 043430.

Sun, Y.-P., C.-K. Wang, and F. Gel'mukhanov, 2010, "Rotational Doppler effect in x-ray photoionization," Phys. Rev. A **82**, 052506.

Sun, Y.-P., *et al.*, 2011, "Intramolecular soft modes and intermolecular interactions in liquid acetone," Phys. Rev. B **84**, 132202.

Sun, Y.-P., *et al.*, 2013, "Interference between Resonant and Nonresonant Inelastic X-Ray Scattering," Phys. Rev. Lett. **110**, 223001.

Sun, Z., M. Chen, L. Zheng, J. Wang, H. Shen, B. Santra, L. Xu, W. Kang, M. L. Klein, and Xifan Wu, 2017, "X-ray absorption of liquid water by advanced *ab initio* methods," Phys. Rev. B **96**, 104202.

Sundin, S., F. Kh. Gel'mukhanov, H. Ågren, S. J. Osborne, A. Kikas, O. Björneholm, A. Ausmees, and S. Svensson, 1997, "Collapse of Vibrational Structure in the Auger Resonant Raman Spectrum of CO by Frequency Detuning," Phys. Rev. Lett. **79**, 1451.

Svanberg, S., 2001, *Atomic and Molecular Spectroscopy: Basic Aspects and Practical Applications* (Springer-Verlag, Berlin).

Svensson, S., *et al.*, 1994, "Observation of an Anomalous Decay Ratio between the Molecular Field Split Levels in the S 2p Core Photoelectron and LVV Auger Spectrum of H_2S," Phys. Rev. Lett. **72**, 3021–3024.

Takata, Y., *et al.*, 2007, "Recoil effects of photoelectrons in a solid," Phys. Rev. B **75**, 233404.

Takata, Y., *et al.*, 2008, "Recoil Effect of Photoelectrons in the Fermi Edge of Simple Metals," Phys. Rev. Lett. **101**, 137601.

Tanaka, A., and T. Jo, 1994, "Resonant 3d, 3p and 3s photoemission in transition metal oxides predicted at 2p threshold," J. Phys. Soc. Jpn. **63**, 2788–2807.

Tanaka, S., and S. Mukamel, 2002, "Coherent X-Ray Raman Spectroscopy: A Nonlinear Local Probe for Electronic Excitations," Phys. Rev. Lett. **89**, 043001.

Thampy, V., *et al.*, 2013, "Comparison of charge modulations in $La_{1.875}Ba_{0.125}CuO_4$ and YBa_2Cu_3O," Phys. Rev. B **88**, 024505.

Thomas, T. D., E. Kukk, K. Ueda, T. Ouchi, K. Sakai, T. X. Carroll, C. Nicolas, O. Travnikova, and C. Miron, 2011, "Experimental Observation of Rotational Doppler Broadening in a Molecular System," Phys. Rev. Lett. **106**, 193009.

Thomas, T. D., *et al.*, 2009, "Photoelectron-recoil-induced rotational excitation of the $B^2\Sigma_u^+$ state in N_2^+," Phys. Rev. A **79**, 022506.

Tokushima, T., Y. Harada, O. Takahashi, Y. Senba, H. Ohashi, L. G. M. Pettersson, A. Nilsson, and S. Shin, 2008, "High resolution x-ray emission spectroscopy of liquid water: The observation of two structural motifs," Chem. Phys. Lett. **460**, 387–400.

Tokushima, T., Y. Horikawa, Y. Harada, O. Takahashi, A. Hiraya, and S. Shin, 2009, "Selective observation of the two oxygen atoms at different sites in the carboxyl group (–COOH) of liquid acetic acid," Phys. Chem. Chem. Phys. **11**, 1679.

Tomonaga, S.-I., 1950, "Remarks on Bloch's method of sound waves applied to many-fermion problems," Prog. Theor. Phys. **5**, 544–569.

Travnikova, O., J.-C. Liu, A. Lindblad, C. Nicolas, J. Söderström, V. Kimberg, F. Gel'mukhanov, and C. Miron, 2010, "Circularly Polarized X Rays: Another Probe of Ultrafast Molecular Decay Dynamics," Phys. Rev. Lett. **105**, 233001.

Tulkki, J., and T. Åberg, 1982, "Behaviour of Raman resonance scattering across the *K* x-ray absorption edge," J. Phys. B **15**, L435.

Turner, J. J., K. J. Thomas, J. P. Hill, M. A. Pfeifer, K. Chesnel, Y. Tomioka, Y. Tokura, and S. D. Kevan, 2008, "Orbital domain dynamics in a doped manganite," New J. Phys. **10**, 053023.

Ueda, K., X.-J. Liu, G. Prümper, T. Lischke, T. Tanaka, M. Hoshimo, H. Tanaka, I. Minkov, V. Kimberg, and F. Gel'mukhanov, 2006, "Role of the recoil effect in two-center interference in x-ray photoionization," Chem. Phys. **329**, 329.

Ueda, K., R. Püttner, N. A. Cherepkov, F. Gel'mukhanov, and M. Ehara, 2009, "High resolution x-ray photoelectron spectroscopy on nitrogen molecules," Eur. Phys. J. Special Topics **169**, 95.

Ueda, K., *et al.*, 2003, "Anisotropic Ultrafast Dissociation Probed by the Doppler Effect in Resonant Photoemission from CF_4," Phys. Rev. Lett. **90**, 233006.

Ulrich, C., *et al.*, 2009, "Momentum Dependence of Orbital Excitations in Mott-Insulating Titanates," Phys. Rev. Lett. **103**, 107205.

Umetsu, R. Y., *et al.*, 2019, "Half-metallicity of the ferrimagnet Mn_2VAl revealed by resonant inelastic soft x-ray scattering in a magnetic field," Phys. Rev. B **99**, 134414.

van Bürck, U., R. L. Mössbauer, E. Gerdau, R. Rüffer, R. Hollatz, G. V. Smirnov, and J. P. Hannon, 1987, "Nuclear Bragg Scattering of Synchrotron Radiation with Strong Speedup of Coherent Decay, Measured on Antiferromagnetic $^{57}FeBO_3$," Phys. Rev. Lett. **59**, 355–358.

van den Brink, J., 2016, "Resonant inelastic x-ray scattering on elementary excitations," in *Quantum Materials: Experiments and Theory*, Modeling and Simulation Vol. 6, edited by Eva Pavarini, Erik Koch, Jeroen van den Brink, and George Sawatzky (Forschungszentrum Jülich, Jülich, Germany), Chap. 12, pp. 12.1–12.31.

van Veenendaal, M., 2015, *Theory of Inelastic Scattering and Absorption of X-Rays* (Cambridge University Press, Cambridge, England).

Vaz da Cruz, V., S. Eckert, and A. Föhlisch, 2021, "TD-DFT simulations of *K*-edge resonant inelastic x-ray scattering within the restricted subspace approximation," Phys. Chem. Chem. Phys. **23**, 1835–1848.

Vaz da Cruz, V., E. Ertan, N. Ignatova, R. C. Couto, S. Polyutov, M. Odelius, V. Kimberg, and F. Gel'mukhanov, 2018, "Anomalous polarization dependence in vibrationally resolved resonant inelastic x-ray scattering of H_2O," Phys. Rev. A **98**, 012507.

Vaz da Cruz, V., *et al.*, 2017, "A study of the water molecule using frequency control over nuclear dynamics in resonant x-ray scattering," Phys. Chem. Chem. Phys. **19**, 19573–19589.

Vaz da Cruz, V., *et al.*, 2019a, "Probing hydrogen bond strength in liquid water by resonant inelastic x-ray scattering," Nat. Commun. **10**, 1013.

Vaz da Cruz, V., *et al.*, 2019b, "Nuclear dynamics in resonant inelastic x-ray scattering and x-ray absorption of methanol," J. Chem. Phys. **150**, 234301.

Velkov, Y., Y. Hikosaka, E. Shigemasa, T. Kaneyasu, J.-C. Liu, and F. Gel'mukhanov, 2009, "Limitations of x-ray absorption spectroscopy of super-high resolution measured in the resonant Auger mode," Phys. Rev. A **79**, 022508.

Voit, J., 1995, "One-dimensional Fermi liquids," Rep. Prog. Phys. **58**, 977–1116.

Wang, R.-P., B. Liu, R. J. Green, M. U. Delgado-Jaime, M. Ghiasi, T. Schmitt, M. M. van Schooneveld, and F. M. F. de Groot, 2017, "Charge-transfer analysis of $2p3d$ resonant inelastic x-ray scattering of cobalt sulfide and halides, J. Phys. Chem. C **121**, 24919–24928.

Wang, Y., Y. Chen, C. Jia, B. Moritz, and T. P. Devereaux, 2020, "Time-resolved resonant inelastic x-ray scattering in a pumped Mott insulator," Phys. Rev. B **101**, 165126.

Weinhardt, L., A. Benkert, F. Meyer, M. Blum, R. G. Wilks, W. Yang, M. Bär, F. Reinert, and C. Heske, 2012, "Nuclear dynamics and spectator effects in resonant inelastic soft x-ray scattering of gas-phase water molecules," J. Chem. Phys. **136**, 144311.

Weinhardt, L., M. Weigand, M. Bär, O. Fuchs, M. Blum, J. D. Denlinger, W. Yang, E. Umbach, and C. Heske, 2011, "Nuclear dynamics in the core-excited state of aqueous ammonia probed by resonant inelastic soft x-ray scattering," Phys. Rev. B **84**, 104202.

Weninger, C., M. Purvis, D. Ryan, R. A. London, J. D. Bozek, C. Bostedt, A. Graf, G. Brown, J. J. Rocca, and N. Rohringer, 2013, "Stimulated Electronic X-Ray Raman Scattering," Phys. Rev. Lett. **111**, 233902.

Weninger, C., and N. Rohringer, 2013, "Stimulated resonant x-ray Raman scattering with incoherent radiation," Phys. Rev. A **88**, 053421.

Wernet, Ph., 2019, "Chemical interactions and dynamics with femtosecond x-ray spectroscopy and the role of x-ray free-electron lasers," Phil. Trans. R. Soc. A **377**, 20170464.

Wernet, Ph., *et al.*, 2004, "The structure of the first coordination shell in liquid water," Science **304**, 995–999.

Wernet, Ph., *et al.*, 2015, "Orbital-specific mapping of the ligand exchange dynamics of $Fe(CO)_5$ in solution," Nature (London) **520**, 78–81.

Wohlfeld, K., M. Daghofer, S. Nishimoto, G. Khaliullin, and J. van den Brink, 2011, "Intrinsic Coupling of Orbital Excitations to Spin Fluctuations in Mott Insulators," Phys. Rev. Lett. **107**, 147201.

Woicik, J. C., J. M. Ablett, N. F. Quackenbush, A. K. Rumaiz, C. Weiland, T. C. Droubay, and S. A. Chambers, 2018, "Experimental assignment of many-electron excitations in the photoionization of NiO," Phys. Rev. B **97**, 245142.

Woicik, J. C., C. Weiland, A. K. Rumaiz, M. T. Brumbach, J. M. Ablett, E. L. Shirley, J. J. Kas, and J. J. Rehr, 2020, "Core hole processes in x-ray absorption and photoemission by resonant Auger-electron spectroscopy and first-principles theory," Phys. Rev. B **101**, 245105.

Wold, A., and R. Arnott, 1959, "Preparation and crystallographic properties of the systems $LaMn_{1-x}Ni_xO_{3+\lambda}$ JA-1106, J. Phys. Chem. Solids **9**, 176.

Wollenweber, L., *et al.*, 2021, "High-resolution inelastic x-ray scattering at the high energy density scientific instrument at the European X-Ray Free-Electron Laser," Rev. Sci. Instrum. **92**, 013101.

Wu, B., *et al.*, 2016, "Elimination of X-Ray Diffraction through Stimulated X-Ray Transmission," Phys. Rev. Lett. **117**, 027401.

Yablonskikh, M. V., Yu. M. Yarmoshenko, V. I. Grebennikov, E. Z. Kurmaev, S. M. Butorin, L.-C. Duda, J. Nordgren, S. Plogmann, and M. Neumann, 2001, "Origin of magnetic circular dichroism in soft x-ray fluorescence of Heusler alloys at threshold excitation," Phys. Rev. B **63**, 235117.

Yamazoe, K., J. Miyawaki, H. Niwa, A. Nilsson, and Y. Harada, 2019, "Measurements of ultrafast dissociation in resonant inelastic x-ray scattering of water," J. Chem. Phys. **150**, 204201.

Yang, M., and J. L. Skinner, 2010, "Signatures of coherent vibrational energy transfer in IR and Raman line shapes for liquid water," Phys. Chem. Chem. Phys. **12**, 982–991.

Yavaş, H., M. Sundermann, K. Chen, A. Amorese, A. Severing, H. Gretarsson, M. W. Haverkort, and L. H. Tjeng, 2019, "Direct imaging of orbitals in quantum materials," Nat. Phys. **15**, 559–562.

Yin, Z., *et al.*, 2015, "Ionic solutions probed by resonant inelastic x-ray scattering," Z. Phys. Chem. (Frankfurt/Main) **229**, 1855–1867.

Yoneda, H., *et al.*, 2015, "Atomic inner-shell laser at 1.5-ångström wavelength pumped by an x-ray free-electron laser," Nature (London) **524**, 446–449.

Young, L., *et al.*, 2018, "Roadmap of ultrafast x-ray atomic and molecular physics," J. Phys. B **51**, 032003.

Yudovich, S., and S. Shwartz, 2015, "Second-harmonic generation of focused ultrashort x-ray pulses, J. Opt. Soc. Am. B **32**, 1894–1900.

Zaanen, J., and G. A. Sawatzky, 1990, "Systematics in band gaps and optical spectra of 3*d* transition metal compounds," J. Solid State Chem. **88**, 8–27.

Zaanen, J., G. A. Sawatzky, and J. W. Allen, 1985, "Band Gaps and Electronic Structure of Transition-Metal Compounds," Phys. Rev. Lett. **55**, 418–421.

Zhovtobriukh, I., N. A. Besley, T. Fransson, A. Nilsson, and L. G. M. Pettersson, 2018, "Relationship between x-ray emission and absorption spectroscopy and the local H-bond environment in water," J. Chem. Phys. **148**, 144507.

Zimmermann, M. v., J. P. Hill, D. Gibbs, M. Blume, D. Casa, B. Keimer, Y. Murakami, Y. Tomioka, and Y. Tokura, 1999, "Interplay between Charge, Orbital, and Magnetic Order in $Pr_{1-x}Ca_xMnO_3$," Phys. Rev. Lett. **83**, 4872–4875.

Zimmermann, P., N. Bouldi, M. O. J. Y. Hunault, M. Sikora, J. M. Ablett, J.-P. Rueff, B. Lebert, P. Sainctavit, F. M. F. de Groot, and A. Juhin, 2018, "$1s2p$ resonant inelastic x-ray scattering magnetic circular dichroism as a probe for the local and non-local orbitals in CrO_2," J. Electron Spectrosc. Relat. Phenom. **222**, 74–87.

Zykova, V. A., Y. A. Karpegina, V. K. Malinovsky, and N. V. Surovtsev, 2017, "Temperature dependence of the Landau-Placzek ratio in liquid water," Phys. Rev. E **96**, 042608.